Use of Gas-eXpanded Liquids as Tunable Solvents for the Preparation of Well-Defined Nanomaterials

by

Steven R. Saunders

A dissertation submitted to the Graduate Faculty of
Auburn University
in partial fulfillment of the
requirements for the Degree of
Doctor of Philosophy

Auburn, Alabama
May 9, 2011

Keywords: Nanotechnology, Nanoparticle, Nanomaterial Processing, Thermodynamics, Computational Modeling, Statistical Analysis

Approved by:

Christopher B. Roberts, Chair, Professor of Chemical Engineering
Ram B. Gupta, Professor of Chemical Engineering
Mario Richard Eden, Associate Professor of Chemical Engineering
Christopher L. Kitchens, Assistant Professor of Chemical Engineering,
Clemson University, Clemson, South Carolina

Abstract

This dissertation presents the research performed to study the precipitation and fractionation of noble metal nanoparticles using gas-expanded liquids. The unique and novel properties of nanoparticles are often found to be highly size-dependent, as such, methods of fine tuning the size distribution of synthesized nanoparticles is crucial in order to make use of these properties in fundamental studies and applications. Traditional methods of nanoparticle processing are typically qualitative, time intensive, and produce large quantities of organic solvent waste. Previously, a technique has been developed that uses mixtures of pressurized CO_2 and an organic solvent to size-selectively precipitate and fractionate nanoparticles. However, this technique was limited to extremely small processing scales (~200 μL volumes) and required relatively large operating pressures (upwards of 35 bars of applied CO_2 pressure).

This work presents methods of size-selectively precipitating and fractionating large quantities of nanoparticle dispersions utilizing techniques that make use to the tunable solvent properties of CO_2-expanded liquids. The methods presented here demonstrate that processing large volumes of nanoparticle dispersions is possible while producing zero waste. A new apparatus is utilized that is simple and cost-effective to build while being scalable to handle larger volumes and modular. This apparatus, at current scales, is capable of size-selectively precipitating and fractionating a polydisperse nanoparticle sample (up to 20 mL) into monodisperse samples. This apparatus can process volumes two orders of magnitude greater than the previous state of the art. Using this technique, it is demonstrated that by judiciously selecting the operating conditions, the recovered nanoparticle sample can be tailored to a specific average size and size-distribution.

Also presented are techniques for tuning the range over which nanoparticles precipitate in a gas-expanded liquid by varying the stabilizing ligand and the composition of solvent media in which the nanoparticles are initially dispersed. A thermodynamically stable dispersion of nanoparticles can be brought to the threshold of stability by adding a secondary poor solvent such that any additional reduction in overall solvent strength of the system would induce nanoparticle precipitation. These methods demonstrate that nanoparticle precipitation is possible at an applied gas pressure 85% lower than what was previously reported.

Modeling these precipitation and fractionation processes is crucial in order to predict the average sizes and size-distributions of recovered nanoparticle fractions. Three models are presented which capture the dynamics of the system in different ways. First, an empirical model which relates simple experimental measurements of the precipitation process into average sizes of the nanoparticles that could be dispersed at a given set of conditions. Secondly, a fundamental thermodynamic model which balances the inherent van der Waals attractive forces with an osmotic repulsive force (due to solvent-ligand interactions) and an elastic repulsive force (due to the compression of the ligand tails between two nanoparticles) has provided an understanding the physical phenomenon that causes the precipitation of nanoparticles in a gas-expanded liquid. Finally, a rigorous fundamental thermodynamic and statistical model which makes use of the known physical nature of the stabilizing ligand shell in order to predict the size-distributions of recovered nanoparticle samples from the gas-expanded liquid fractionation process.

Acknowledgements

First and foremost, I'd like to thank my advisor Dr. Christopher B. Roberts who has always provided encouragement, thoughtful discussions, and needed advice, whether it was scholarly or personal. Chris has been so much more than just an advisor and has become a true friend. I would also like to thank him for allowing me to take on my own independent project and let me have to freedom to do new and exciting work. I would also like to thank all of my committee members for taking the time to make significant contributions to all portions of this dissertation. A special thanks to Brian Schweiker and Dr. Michael Miller, for their assistance when anything broke and needed to be fixed in an unreasonable amount of time.

Thanks are also due current and past members of the Roberts' Reseach Group. Specifically, I'd like to mention the work done by Madhu Anand, Chandler McLeod, Chris Kitchens, Greg Von White, and Seong-Sik Yoo whom have contributed significantly to work presented here. I would also like to thank the other members of the Roberts' group for having to share an office with me: Debbie Bacik, Ed Durham, Dan Obrzut, Kendall Hurst, Rui Xu, Sihe Zhang, Raj Chinnawar, and Jennifer Boice.

I also need to thank my mother, Janine, and my brothers, Chris and Jon. I wouldn't be here without their unconditional love, support, and guidance.

Table of Contents

List of Figures

List of Tables

List of Abbreviations

ΔE	Change in Total Energy of the System
ΔP	Pressure Change Between Fractionation Stages
ΔV	Change in Volume of a GXL
Γ	Ligand Surface Coverage Ratio
Γ_{slab}	Ligand Surface Coverage Ratio on a Flat Surface
Φ_{elas}	Elastic Repulsive Potential Energy
Φ_{osm}	Osmotic Repulsive Potential Energy
Φ_{total}	Total Interaction Energy
Φ_{vdW}	Van der Waals Attractive Potential Energy
α	Maximum One-Dimensional Step Size
χ	Flory-Huggins Interaction Parameter
δ_i	Hildebrand Solubility Parameter of Component i
ϵ	Extinction Coefficient
ϵ_i	Dielectric Constant of Material i
λ_p	Surface Plasmon Resonance Band Wavelength
μ	Average Diameter
ν_e	Main Electronic UV Absorption Frequency
ρ	Density
σ	Standard Deviation
$\tilde{\phi}_i$	Volume Fraction of Component i
ξ_i	Random Variable
A	Absorbance
A_{Au}	Atomic Gold Cross-Sectional Area

$AgNO_3$	Silver Nitrate
A_{ii}	Hamaker Constant, Material i Interacting Through a Vacuum
A_{iji}	Hamaker Constant, Material i Interacting Through Medium j
A_{thiol}	Ligand Tail Cross-Sectional Area
BDAC	Benzyldimethylhexadcylammonium Chloride
C_{16}TAB	Cetyltrimethylammonium Bromide
C	Concentration
c	Normalization Constant
c_1	Regression Parameter
c_2	Regression Parameter
CDF	Cumulative Distribution Function
CdSe/ZnS	Cadmiun Selenide/Zinc Sulfate (Core/Shell)
CO_2	Carbon Dioxide
CPM	Condensed Phase Model
D	Nanoparticle Diameter
d	Center-to-Center Separation Distance
D-H_2O	Deionized Ultra Filtered Water
$\overline{D}_i$	Average Nanoparticle Diameter of Fraction i
D_i	Diameter of the ith Nanoparticle
$\overline{D_N}$	Number Average Diameter
$\overline{D_W}$	Diameter-Weighted Average Diameter
DDT	1-Dodecanethiol
$disperse$	Probability Distribution Function of the Precipitated Nanoparticles
DIUF	Deionized Ultra Filtered
D_{Ti}	Threshold Nanoparticle Size of Fraction i
E	Total System Energy
ELLSM	Extended Ligand Length Solvation Model

GaI	Gallium Iodide
GXL	Gas-eXpanded Liquid
h	Planck's Constant
H_2PtCl_6	Chloroplatinic Acid
h	Surface-to-Surface Separation Distance
$HAuCl_4 \cdot 3H_2O$	Hydrogen Tetrachloroaurate (III) Trihydrate
HT	1-Hexanethiol
InP	Indium Phosphorous
K_2PdCl_4	Potassium Tetrachloroplatinate (II)
k_B	Boltzmann Constant
$KC_4H_5O_6$	Potassium Bitartrate
k_{ij}	Binary Interaction Parameter
L	Thickness of the Ligand Shell
L/D	Aspect Ratio = Length / Diameter
$L_{collapsed}$	Thickness of a Fully Collasped Ligand Shell
L_{ext}	Extended Ligand Length
LLLSM	Limited Ligand Length Solvation Model
l	Path Length
M	Molecular Weight
MW_2	Molecular Weight of the Ligand
n	Number of Nanoparticles Sized
N_A	Avogadro's Number
$NaBH_4$	Sodium Borohydride
n_i	Reflective Constant of Material i
OT	1-Octanethiol
P_1	Pressure for First Fractionation Stage
P_2	Pressure for Second Fractionation Stage

PDF	Probability Distribution Function
PDI	Polydispersity Index
P_2^m	Average Pressure of the Second Fractionation Stage
precip	Probability Distribution Function of the Precipitated Nanoparticles
R	Gas Constant
R	Nanoparticle Radius
r	Molecular Segment Length
RSD	Relative Standard Deviation
S3MP	Sodium 3-mercaptopropionate
$scCO_2$	Supercritical Carbon Dioxide
SCF	Supercritical fluid
SPRB	Surface Plasmon Resonance Band
T	Temperature
TADDD	Bis(11-trimethylammoniumdecanoylaminoethyl)-disulfide Dibromide
TDPC	3,3′-Thiodipropionic Acid
TEM	Transmission Electron Microscope
TGA	Thermogravimetric Analysis
TOABr	Tetra-n-octylammonium Bromide
V	Volume
V_o	Initial volume
v_i	Molar Volume
w/o	Water-in-Oil Micelle
X	Coordinate 1 of Nanoparticle Position
x_i	Mole Fraction of Component i
Y	Coordinate 2 of Nanoparticle Position
Z	Coordinate 3 of Nanoparticle Position

Chapter 1

Introduction

1.1 Introduction to Nanotechnology

Nanotechnology is the study and application of materials with at least one critical dimension at the nanoscale (i.e., less than 100 nanometers, 1 nm = 10^{-9} meters). Materials with dimensions at these length scales exhibit very unique electrical, optical, magnetic, mechanical and catalytic properties that are not seen at the bulk scale or at the molecular scale (Adair *et al.*, 1998; Poole & Owens, 2003). Nanotechnology involves the understanding and manipulation of matter at the nanoscale to exploit these novel properties as well as creating new and powerful materials, devices, and systems that utilize these novel properties.

These very unique and novel properties of nanomaterials arise from the materials being incredibly small, smaller than the critical lengths which characterize many physical phenomena (Poole & Owens, 2003). Table 1.1 lists the characteristic lengths associated with several important properties in solid state sciences. For example, electrical conductivity of a metal is characterized by a critical length, the inelastic mean free path (the distance an electron can travel before colliding with another electron). If the size of a particle is less than this critical length, it is possible that new physics or chemistries may arise leading to new properties that do not exist in the bulk scale but differ from those seen at the molecular scale.

The use of nanomaterials is not new. Nanoscale gold and silver particles have been used to color glass since the Roman civilization. Vases that appear light green in color until a light was placed inside causing the color to change to a red-wine color have been discovered that are colored by gold nanoparticles (Murday, 2002). The Roman artisans

Field	Property	Length Scale
Electronic	Electronic Wavelength	10 - 100 nm
	Inelastic Mean Free Path	1 - 100 nm
	Tunneling	1 - 10 nm
Magnetic	Domain Wall	10 - 100 nm
	Exchange Frequency	0.1 - 1 nm
	Spin-Flip Scattering Length	1 - 100 nm
Optic	Quantum Well	1 - 100 nm
	Evanescent Wave Decay Length	10 - 100 nm
	Metallic Skin Depth	10 - 100 nm
Superconductivity	Cooper Pair Coherence Length	0.1 - 100 nm
	Meisner Penetration Depth	1 - 100 nm
Mechanics	Dislocation Interaction	1 - 100 nm
	Grain Boundaries	1 - 10 nm
Nucleation/Growth	Defect	0.1 - 10 nm
	Surface Corrugation	1 - 10 nm
Catalysis	Localized Bonding Orbitals	0.01 - 0.1 nm
	Surface Topology	1 - 10 nm
Supramolecules	Primary Structure	0.1 - 1 nm
	Secondary Structure	1 - 10 nm
	Tertiary Structure	10 - 100 nm
Immunology	Molecular Recognition	1 - 10 nm

Table 1.1: Characteristic lengths of several important properties in solid state science

knew how to achieve the effect but were unaware of its "nano-basis." Not until the 20th century was the phenomenon understood. Since the late 1980's, access to reliable analysis techniques (e.g., transmission/scanning electron microscopy, atomic force microscopy, etc.) has dramatically increased allowing for the measurement and manipulation of nano-sized structures. Fundamental nanotechnology research has increased more than 10-fold since the late 1980's to over $1.5 billion in federally funded research in the United States (NNI, 2005; NNI, 2008; NNI, 2009).

Nanomaterials find applications in several areas including dispersions and coatings, high surface area materials, functional nanodevices, and consolidated materials (Siegel *et al.*, 1998). Applications in which nanomaterials are used as dispersions and coatings include cosmetics, pharmaceuticals, printing, semiconductors and sensors. These applications make use of the enhanced properties of well dispersed, agglomeration-free nanostructures. Nanomaterials have a large surface area to volume ratio, and as such, have a large percentage of surface atoms compared to their bulk counterparts. These large surface area to volume ratios have led to nanomaterials being used in applications such as catalysis, membranes, energy storage, and adsorption and desorption processes. As the ability to control materials down to the nanoscale improves it is possible to drastically improve electronic devices. The efficiency of computer processors scales with the density of transistors on the chip. A higher number of transistors per area allows for faster chip speeds while decreasing the energy required to operate. Through similar "scale down" methods, nanoscale devices will lead to better electronic devices, help control pollution and improve human health. One of the largest applications of nanomaterials is in composites, or consolidated materials. Through combining nanomaterials with conventional materials, it is possible to alter the hardness, strength, magnetic properties and optical properties. In just about every possible field, nanomaterial composites will be used to make things smaller and lighter while maintaining or improving strength.

1.1.1 Size-Dependent Properties of Nanomaterials

As stated earlier, nanomaterials are often smaller than the critical lengths associated with physical properties. The potential for creating materials with new, enhanced properties is huge through an exacting control over the size and the size distribution of nanoparticles. The properties of nanoparticles can change drastically with size due the change in number of surface atoms, variations in the density of electronic energy levels, the emergence of quantum-like transport and predominance of interfacial phenomena (Adair *et al.*, 1998). Nanoparticles, when synthesized, are often found to have lognormal or normal distributions (Granqvist & Buhrman, 1976; Kiss *et al.*, 1999) with a broad standard deviation (Murray *et al.*, 2000) and, as such, the ability to control the size-distribution is of the utmost importance.

While all properties (magnetic, optical, electronic, catalytic, etc.) tend to vary with nanoparticle size, the most visual example of properties is the change of the color (under UV light) of differently sized quantum dots (i.e., semiconductor nanoparticles) as seen in Figure 1.1 (Guzelian *et al.*, 1996; Alivisatos, 1996a; Alivisatos, 1996b; Shiang *et al.*, 1996). The optical properties of these nanomaterials (e.g., CdSe/ZnS, GaI, InP, etc.) can be utilized in many applications including sensors and medical diagnoses. The size of the nanoparticles limits the movement of electrons (called *quantum confinement*) which causes the quantization of the bulk energy bands into discrete energy levels. In the case of these semiconductor materials, the discrete energy levels shift to higher energies compared to the bulk material as the material size decreases, leading to different colors for different sizes.

The color of nanomaterials typically differ from that of their bulk counterparts due to a phenomenon known as surface plasmon resonance. Surface plasmons are temporary dipoles created along the surface of nanomaterials due to an energy transfer from light. Incident light is absorbed by the material and the energy induces electron oscillations on the surface of the material (Mie, 1908). The surface plasmon resonsnance band (SPRB)

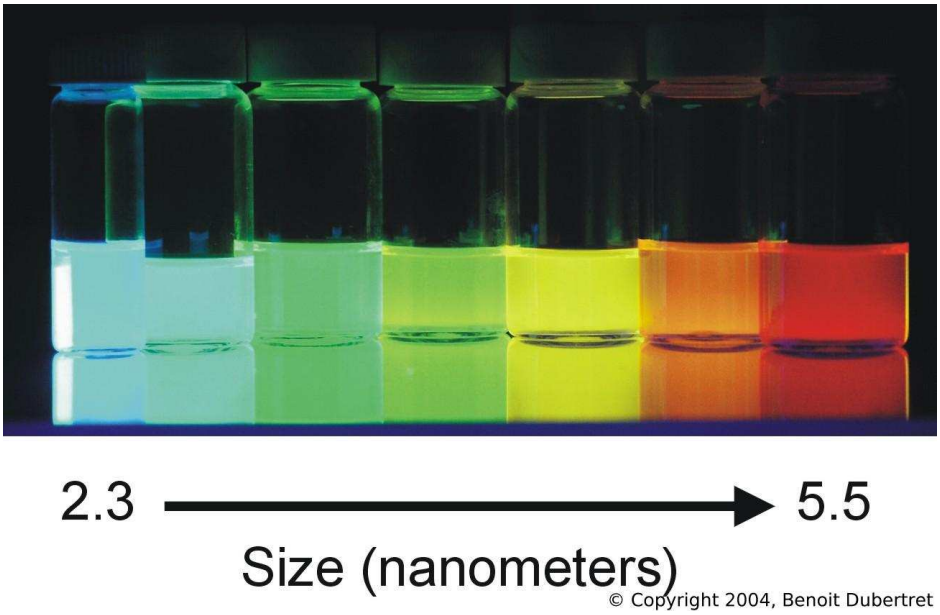

Figure 1.1: Size-dependent color (under UV light) of CdSe/ZnS nanoparticles. Reprinted with permission from Benoit Dubertret

wavelength, λ_p, is a characteristic property of each material and can vary with size. This wavelength not only varies with size but also with shape. Plasmons exist for each line of symmetry across a nanomaterial. For example, nanoparticles have only one line of symmetry (symmetry of rotation) and hence only one surface plasmon which varies with diameter. On the other hand, nanorods have two lines of symmetry (along the length of the rod, and around the rod perpendicular to the length) and hence there are two surface plasmons one with varies with aspect ratio and another with diameter (Perez-Juste *et al.*, 2005). A summary of the variation of λ_p for several materials and sizes is available in Table 1.2.

The ability to control the size and size-distribution is of the utmost importance when producing nanomaterials for specialized applications. Two ways are available to do this: (1) specialized nanomaterial synthesis routes to produce monodisperse nanomaterials or (2) post-synthesis processing techniques to produce monodisperse nanomaterials from polydisperse nanomaterials.

1.1.2 Synthesis of Nanomaterials

Nanomaterials are synthesized either in a top-down approach or a bottom-up approach. In top-down methods, the dimensions of larger objects are gradually reduced; this can be done through a number of techniques including, but not limited to, lithography (Haynes & Van Duyne, 2001), ball-milling (Guerard *et al.*, 2007) or laser ablation (Ullmann *et al.*, 2002). These techniques involve a large object that is "sculpted" or milled to create smaller materials. Bottom-up methods involve the chemical assembly of individual atoms or molecules into a final material. This can be done through basic chemical techniques including acid/base reactions, salt precipitation, or redox reactions (Poole & Owens, 2003). Individual material techniques build on one of these methods and tailor the reaction to achieve the best control over the size, shape, and composition of the final material.

Material	Nanoparticle Diameter (nm)	λ_p (nm)	ref.
Gold	8.9	517	(Link & El-Sayed, 1999)
	14.8	520	
	21.7	521	
	48.3	533	
Silver	3.66	443	(Lee *et al.*, 1992)
	4.87	443	
	8.09	472	
	10.64	497	
CdSe/ZnS	5.2	594	(Anand *et al.*, 2007)
	3.2	563	
	2.4	522	
	1.9	475	

Table 1.2: Wavelength of maximum absorbance due to surface plasmon resonance for several different materials and nanoparticle diameters

Nanoparticle Synthesis

Metallic nanoparticles have traditionally been synthesized via the coprecipitation of a metal in both aqueous and nonaqueous solvents. This involves the chemical reduction of metal cations which then begin to nucleate and grow into nanoparticles. Growth of the nanoparticles into bulk material (i.e, irreversible nanoparticle agglomeration) is typically inevitable unless a stabilizer is used to halt the growth and protect the nanoparticle core. Two types of stabilizers are available: (1) stabilizers which create a steric repulsion between nanoparticles (via surfactants, polymers, or other organic species) generally referred to as capping ligands, or (2) electrostatic repulsions due to the chemisorption of charged species to the surface of the nanoparticle. Stabilized nanoparticles help prevent agglomeration while adding additional functionalization to the surface of the nanoparticle.

Turkevich *et al.* described a method for synthesizing gold nanoparticles by boiling a mixture of dilute hydrogen tetrachloroaurate (III) trihydrate ($HAuCl_4 \cdot 3H_2O$) and sodium citrate (Turkevich *et al.*, 1954). The sodium citrate not only acts a reducing agent for the gold cation but also as stabilizer to prevent agglomeration. This method produces gold nanoparticles of approximately 20 nm in diameter. Yonezawa *et al.* have shown that when sodium 3-mercaptopropionate (S3MP) is added simultaneously with the sodium citrate, the size of the stabilized nanoparticles can be controlled by varying the stabilizer/gold ratio (Yonezawa & Kunitake, 1999). Similar methods, usually based on the Turkevich technique are used to produce other metal nanoparticles. Silver nanoparticles can be produced through the reduction of silver nitrate ($AgNO_3$) by sodium borohydride ($NaBH_4$) in the presence of bis(11-trimethylammoniumdecanoylaminoethyl)-disulfide dibromide (TADDD) as a stabilizer (Yonezawa *et al.*, 2000). Tan *et al.* demonstrated that platinum, gold, and palladium nanoparticles can be synthesized via the reduction of the chloride salt (H_2PtCl_6, $HAuCl_4$, and K_2PdCl_4, respectively) by potassium bitartrate ($KC_4H_5O_6$) in the presence of 3,3'-thiodipropionic acid (TDPC) (Tan *et al.*, 2003).

The typical growth kinetics for the synthesis of nanoparticles is presented in Figure 1.2. As the concentration of the precursor metal ions that have been reduced exceeds the supersaturation limit, nucleation begins and nanoparticles begin to form. At the moment nanoparticles are present, some of the metal precursor will simultaneously be used to grow the existing nanoparticles. Nucleation continues until the concentration of the reduced precursor drops below the supersaturation limit (due to the precursor being used for both nucleation and growth). In the nucleation regime, the number of nanoparticles drastically increases. As the growth of the nanoparticles is a continuous process, the average size of the synthesized nanoparticles constantly increases. As nucleation and growth occur at the same time early in the reaction, polydispersity increases until nucleation stops where it begins to decrease due to the increase in size of all nanoparticles at a similiar rate. Polydispersity also decreases do to a phenomenon known as ripening where the overall average diameter of the nanoparticles change (i.e., increase) at the expense of other nanoparticles (Stoeva *et al.*, 2002; Cushing *et al.*, 2004).

The nucleation and growth regimes occur simultaneously due the large concentration of metal ions needed for most synthesis routes (i.e., a significant amount of time is spent with the concentration of the reduced precursor greater than the supersaturation limit). This leads to a sample with wide size distributions. It has been demonstrated (Brown & Natan, 1998; Jana *et al.*, 2001b) that when the nucleation and growth regimes are separated, a fine control over nanoparticle size can be achieved by limiting the amount of time spent in the nucleation regime (i.e., low concentrations are used such that nucleation occurs and immediately stops whereupon growth begins). Gold nanoparticle seeds can be created in aqueous media where low concentrations of salts are used such that, when completely reduced, are still relatively small (<4 nm). From these seeds, additional amounts of metal cations can be added and reduced slowly such that no new nucleation sites are formed whereupon the reduced metal adsorbs to the surfaces of existing nanoparticles. Nanoparticles from these seeded growth methods can produce nanoparticles 5 - 40 nm

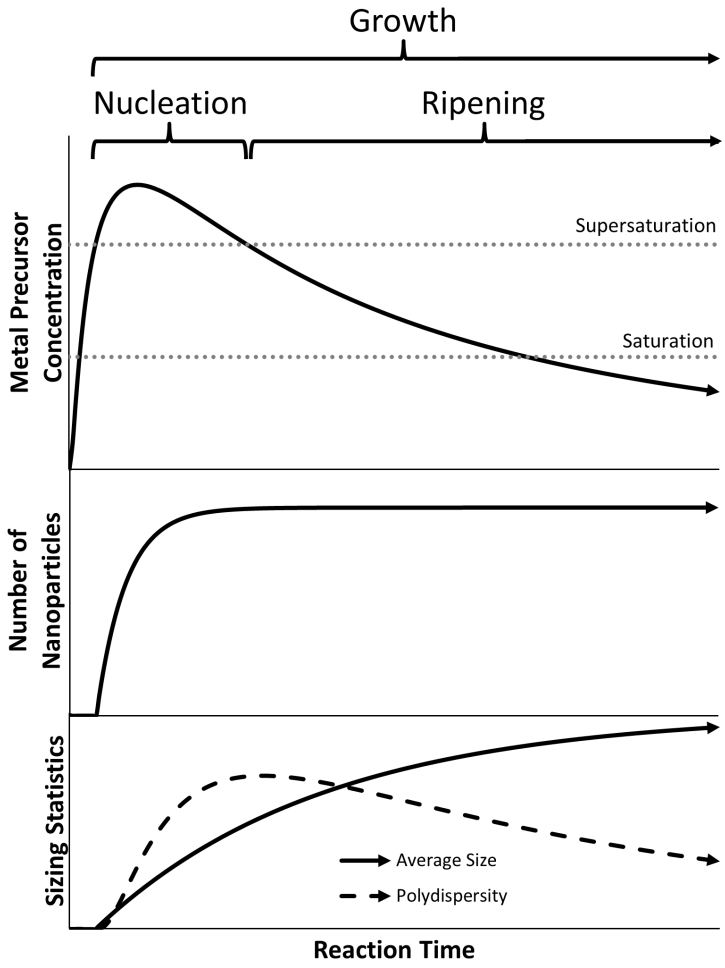

Figure 1.2: Typical nanoparticle growth kinetics.

in diameter with a narrow size distribution (relative standard deviation, RSD, of 10-15% (Daniel & Astruc, 2004; Liu *et al.*, 2006)).

Nanoparticles that are prepared in an aqueous solution without a stabilizing agent, while stable for long periods against agglomeration (typically due to electrostatic repulsions) cannot be redispersed when isolated as dry powders nor processed easily for application purposes such as thin films, thus leading to a need for synthesis routes with organic solvents. However, to follow the same technique, dissolution of a metal salt followed by reduction and growth, cannot occur as most common metal salts are not readily soluble in organic solvents. The Brust-Schiffrin arrested precipitation allows for large quantities of gold and silver nanoparticles to be produced in an organic solvent (Brust *et al.*, 1994; Sigman *et al.*, 2004). This technique involves the dissolution of the metal salt in water (Equation 1.1) and through the use of a phase-transfer catalyst, tetraoctylammonium bromide (TOABr), the metal cation can be transferred to the organic phase (Equation 1.2) where it is reduced, commonly by $NaBH_4$ (Equation 1.3), and stabilized with 1-dodecanethiol (Equation 1.4) (Brust *et al.*, 1994).

$$HAuCl_4 \xrightarrow{H_2O} H^+_{(aq)} + AuCl^-_{4(aq)} \tag{1.1}$$

$$AuCl^-_{4(aq)} \xrightarrow{[CH_3(CH_2)_7]_4N^+} AuCl^-_{4(org)} \tag{1.2}$$

$$Au^{3+} + 3\,e^- \longrightarrow Au^o \tag{1.3}$$

$$m\,Au + n\,HS(CH_2)_{11}CH_3 \longrightarrow Au_m[HS(CH_2)_{11}CH_3]_n \tag{1.4}$$

It is important to note that the chemistry for the arrested precipitation synthesis of silver nanoparticles is not well understood as the cationic phase transfer catalyst cannot bind to the cationic silver ion (Brust *et al.*, 1994). It is thought that the silver cation complexes with several free bromide anions and then transferred into the organic (Goulet & Lennox, 2010) . This method produces nanoparticles 2-12 nm in diameter with a large relative

standard deviation (RSD = 25-30%). However, these nanoparticles can be isolated as dry powders and redispersed in any number of nonpolar or weakly polar solvents (e.g., chloroform, toluene, alkanes, etc.) due to the stabilization provided by the covalently bonded thiol. Additional functionality can be added by changing the capping ligand; rather than thiol-based capping ligands, carboxylic acids, amines (Thomas *et al.*, 2002), silanes and phosphines (Prasad *et al.*, 2003) have also been explored.

A similar technique to the Brust-Schiffrin technique was developed by Stoeva *et al.* which allows for gram-scale quantities of monodisperse gold nanoparticles to be synthesized (Stoeva *et al.*, 2002). Through a process known as digestive ripening, polydisperse gold nanoparticles were converted to monodisperse nanoparticles. Digestive ripening occurs when additional energy (e.g., heat) is supplied, where the additional energy overcomes the stabilizing energy of the capping ligands and the nanoparticle sizes begin to change. Digestive ripening is seen as a form of forced Ostwald ripening, or coarsening, where smaller nanoparticles are consumed by larger nanoparticles (Cushing *et al.*, 2004). This phenomena is not fully understood but is believed to occur simultaneously with the growth regime (see Figure 1.2).

Nanoparticle synthesis in microemulsions has garnered significant attention since the 1980's due to the wide range of materials that can be produced using this method (Eastoe *et al.*, 2006). A microemulsion is a thermodynamically stable dispersion of two immiscible fluids through the use of surfactants. Of interest for nanoparticle syntheses are water-in-oil (w/o) microemulsions (reverse micelle) in which droplets of water are dispersed through a continuous hydrocarbon phase. Any inorganic reagent encapsulated within the micelle ("microreactor") becomes well mixed. Typical synthesis routes involve the preparation of two w/o micellular solutions, dissolved metal salt in one and dissolved reducing agent in the other. Upon mixing of these two solutions, the micelles collide and percolate, thereby mixing the contents of the two micelles (Capek, 2004). Nanoparticles made from various materials can be synthesized from w/o microemulsions: gold (Herrera *et al.*, 2005; Spirin

et al., 2005), silver (Petit *et al.*, 1993), copper (Lisiecki & Pileni, 1995), cobalt (Petit *et al.*, 1999; Lisiecki & Pileni, 2003), zinc sulfide (Khiew *et al.*, 2005), cadmium selenide (Petit & Pileni, 1988), titanium (II) oxide (Saiwan *et al.*, 2004; Lee *et al.*, 2005), calcium carbonate (Rauscher *et al.*, 2005), iron (III) oxide (Shi & Verweij, 2005), and polyaniline (Xing *et al.*, 2005). One reason why nanoparticle synthesis in microemulsions is so popular is the ability to control particle size and polydispersity by adjusting the type of solvent (Cason *et al.*, 2001), the surfactant (López-Quintela *et al.*, 2004), addition of an electrolyte (Kitchens *et al.*, 2005), concentration of reagents (Maillard *et al.*, 2003), or the water-to-surfactant molar ratio (Cason *et al.*, 2001; Kitchens *et al.*, 2003; Kimijima & Sugimoto, 2005). Following synthesis, the surfactant may be exchanged for a thiol, sulfide, carboxylic acid, or amine in order to increase the functionality of the nanoparticle (Lin *et al.*, 1999).

Nanorod Synthesis

Beyond nanoparticles, another class of nanomaterials which has garnered extreme interest is nanorods. The interest in this shape of nanomaterial is due to their very unique optical properties. Typical nanorod formation is through either an electrochemical technique (Martin, 1994; Foss *et al.*, 1994; Martin, 1996; Yu *et al.*, 1997) or a seeded growth technique. Seeded growth techniques for nanorods are very similar to those discussed for nanoparticles and are typically synthesized under very similar conditions. Through the use of cetyltrimethylammonium bromide (C_{16}TAB), Jana *et al.* were able to produce high aspect ratio (L/D = 4.3, 13, and 18) gold nanorods from the same seeds discussed previously (Jana *et al.*, 2001a). Nanorods are formed, rather than nanoparticles, due to the presence of the C_{16}TAB, which forms a bilayer at the surface of the rod. C_{16}TAB is an amphiphilic molecule (hydrophilic head group and hydrophobic tails), where the bilayer is created with head groups of the C_{16}TAB preferentially binding to the crystallographic faces along the sides of the nanorod rather than the tips. This leads to growth in the longitudinal direction rather than radially. Through simple adjustments in various

reagent conditions, the product can be targeted to specific aspect ratios, diameters, or crystal structure. It has been demonstrated that the addition of silver nitrate to the growth mixture helps control crystal structure as well as increase the yield of nanorods versus nanoparticles (Jana *et al.*, 2001c). Nikoobakht and El-Sayed were able to reduce the number of non-cylindrical products by replacing citrate-capped seeds with C_{16}TAB-capped seeds (Nikoobakht & El-Sayed, 2003). Typical seed-mediated nanorod synthesis routes are capable of producing nanorods with tunable aspect ratios (L/D = 1.5 - 5), however by changing the surfactant from a pure C_{16}TAB solution to a mixture of C_{16}TAB and benzyldimethylhexadcylammonium chloride (BDAC), nanorods with an aspect ratio up to 8 can be produced (Nikoobakht & El-Sayed, 2003). It has been demonstrated that even minor differences in the surfactant can lead to products with various yields (0% rods - nearly 100%) depending on manufacturer due to the amount of impurities (Durr *et al.*, 2007; Smith & Korgel, 2008).

1.1.3 Size and Shape Separation of Nanomaterials

As the properties of nanomaterials are highly dependent on their size and size-distribution, being able to produce large quantities of monodisperse nanomaterials is of the utmost importance for certain applications and fundamental studies. Typical methods of producing monodisperse nanomaterials are not well-suited for producing large quantities. Seed-mediated nanoparticle syntheses inherently require a low metal ion concentration as to prevent new nucleation sites from forming thus producing only low concentrations of nanoparticles (Jana *et al.*, 2001b). The seed-mediated nanorod synthesis methods always produce an amount of nanoparticles or other non-cylindrical products (Jana *et al.*, 2001c; Nikoobakht & El-Sayed, 2003). Likewise, methods that produce large quantities of nanomaterials lead to very polydisperse products. The Brust-Schiffrin arrested precipitation synthesis route produces large concentrations of polydisperse (RSD = 25 - 30%) nanoparticles (Brust *et al.*, 1994; Bethell *et al.*, 1996). As synthesis routes

for producing large quantities of monodisperse nanoparticles do not exist, post-synthesis processing methods for controlling size and shape are needed.

Separation by Size

The most common method of size-selectively separating, or fractionating, nanoparticles is through an antisolvent precipitation (Brust *et al.*, 1994; Murray *et al.*, 2000; Sigman *et al.*, 2004). This technique, useful for organic dispersions of nanoparticles, involves the drop-wise addition of a poor solvent to a stable dispersion. As the amount of antisolvent is increased, the solvent strength of the solvent media drops to the point where the nanoparticles can no longer be stabilized in the solvent mixture. The nanoparticles with the largest size exhibit the largest van der Waals forces of attraction and tend to agglomerate and precipitate first while leaving the smaller nanoparticles in a stable dispersion (Ohara *et al.*, 1995; Yamaki *et al.*, 1995). Centrifugation can aid in the agglomeration and precipitation process. The solvent mixture can be decanted, leaving the largest nanoparticles precipitated which can then be redispersed by addition of the original neat solvent. The smaller nanoparticles, those in the decanted solvent media, can be fractionated further by adding more antisolvent. Through repeated addition of solvent and antisolvent, the fractionated nanoparticles can be separated into narrow size distributions, RSD < 5% (Murray *et al.*, 2000) . This technique is used in many laboratories due to its simplicity. However, it is very qualitative, slow, and requires large amounts of solvent. This method could not be considered for an industrial process due to the expenditures for equipment (centrifuges to accelerate the agglomeration and precipitation) and solvent recovery (energy expenditures for solvent separation and purification over waste costs).

Hanauer *et al.* have demonstrated a technique which makes use of gel electrophoresis to size-selectively separate nanoparticles (Hanauer *et al.*, 2007). This technique exploits the behavior of polymers covalently bonded to the surface of the nanoparticle. Through

simple chemical adjustments in the tail groups of the polymer chains, it is possible to adjust the charge and mobility needed to achieve an effective separation between differently sized nanoparticles. Arnaud *et al.* have made use of isoelectric focusing electrophoresis to size-selectively fractionate nanoparticles (Arnaud *et al.*, 2005) which has shown to eliminate the need of attaching large polymers to the surface of the nanoparticles which can hinder their properties. While being rather effective, these techniques are not applicable to industrial scales due to their extremely low throughput and limited by the cost of electrophoresis gel.

Chromatography has also been used to obtain monodisperse nanoparticles. Several research groups have reported the use of high pressure liquid chromatography HPLC to separate semiconductor nanoparticles (Fischer *et al.*, 1989) as well as gold and silver nanoparticles (Wilcoxon *et al.*, 1998; Jimenez *et al.*, 2003). Again, while producing effective separations, chromatography does not lend itself well for industrial applications as throughput is low and equipment costs are high.

High throughput, flow systems have garnered signification attention recently. Sweeney *et al.* have reported on a rapid size-selective separation and purification technique that utilizes diafiltration (Sweeney *et al.*, 2006). This method makes use of semi-permeable membranes of varying molecular weights (i.e., pore diameter) which can effectively fractionate polydisperse samples into monodisperse fractions. Stavis *et al.* have recently reported on a prototype nanofluidic device, much like a coin sorter, capable of physically separating nanoparticles greater than 10 nm (Stavis *et al.*, 2009).

Separation by Shape

In contrast to the varied techniques used to size-selectively separate nanoparticles, shape-selective separation is rather limited. The few techniques to separate nanomaterials by shape involve centrifugation to balance viscous forces with drag forces (Alekseeva *et al.*, 2006). Reaction products from typical seed-mediated nanorod synthesis can be

concentrated via centrifugation and placed atop step-gradient glyercol and centrifuged a second time. Products with low drag coefficients easily traverse the differing viscous layers whereas products that experience significant drag will only traverse certain layers. This leads to a gradient of products ranging from nanoparticles at the bottom of the centrifuge tube (the most viscous region) to high aspect ratio rods at the top of the centrifuge tube. Germain *et al.* used a similar method to separate silver nanodisks from silver nanoparticles (Germain *et al.*, 2005). Rather than using a step-gradient method, this centrifugation technique balances solvation forces with centrifugal forces. Larger silver nanodisks are not as stably dispersed as smaller nanoparticles and, therefore, when centrifuged, can be temporarily forced from dispersion.

The Hanauer electrophoresis method for size-selectively separating nanoparticles can also be used to shape-selectively separate nanomaterials (Hanauer *et al.*, 2007). It has been shown to be effective for separating spheres, rods, and triangles. Outside of electrophoresis which has been shown to be effective for both shape and size separation, chromatography is also effective. Size-exclusion chromatography has been shown to be able to separate gold nanoparticles from gold nanorods (Wei *et al.*, 1999).

1.2 Tunable Solvent Systems

The properties of compressed fluids can often be varied by tuning the applied pressure or temperature of the system. Two examples of these tunable compressed fluid systems are supercritical fluids and gas expanded liquids. These systems are very prevalent in areas such as drug and materials synthesis and processing.

1.2.1 Supercritical Fluids

A supercritical fluid (SCF) occurs when any material is heated and compressed beyond its critical point (Clifford, 1999). As a material is heated and compressed along the vapor-liquid equilibrium line (as can be seen in the phase diagram of carbon dioxide ,CO_2, in

Figure 1.3) the liquid becomes less dense due to thermal expansion and the vapor become more dense due to increasing pressure. Eventually, at the critical point, the density of the two phases become identical and the distinction between the vapor and the liquid disappears. Simple variations in the applied pressure of a SCF lead to variations in the density of the fluid thus leading to variations in the physico-chemical properties of the SCF, such as diffusivity, solvent strength, viscosity and heat capacity (McHugh & Krukonis, 1994) allowing for the properties of the SCF to be tuned by simply varying the applied pressure. A major benefit of using SCF's as solvents is that diffusivities are larger than and viscosities lower than the conventional liquid counterparts (Vesovic *et al.*, 1990) while maintaining the liquid-like solvent strength.

Carbon dioxide is the most widely studied and utilized supercritical fluid being continuously studied for well over 50 years with significant industrial activity in the last 20 years (Beckman, 2004). While supercritical fluids in general are of interest, CO_2 and $scCO_2$ (supercritical carbon dioxide) garner a great deal of interest due to CO_2's "green" properties. CO_2 is nonflammable, relatively nontoxic and inert, readily available, miscible with a variety of low molecular weight organic liquids, environmentally benign and inexpensive. The supercritical region is easily accessible as the critical temperature is 304 K and critical pressure 71 bar. This combination of properties makes $scCO_2$ useful in processes which involve extraction, chromatography, chemical reactions (hydrogenations, hydroformylations, oxidations, and Friedel-Crafts alkylations/acylations) and microparticle formation (Beckman, 2004). Microparticle formation with $scCO_2$ can be accomplished through a variety of techniquies, including rapid expansion of supercritical solution (RESS), aerosol solvent extraction system (AES), and supercritical antisolvent (SAS) (Jung & Perrut, 2001a). While $scCO_2$ has found uses in a wide variety of applications, its use as a solvent has been very limited. The dielectric constant of $scCO_2$ is very low, ranging 1.1 - 1.5 depending on the density. The combination

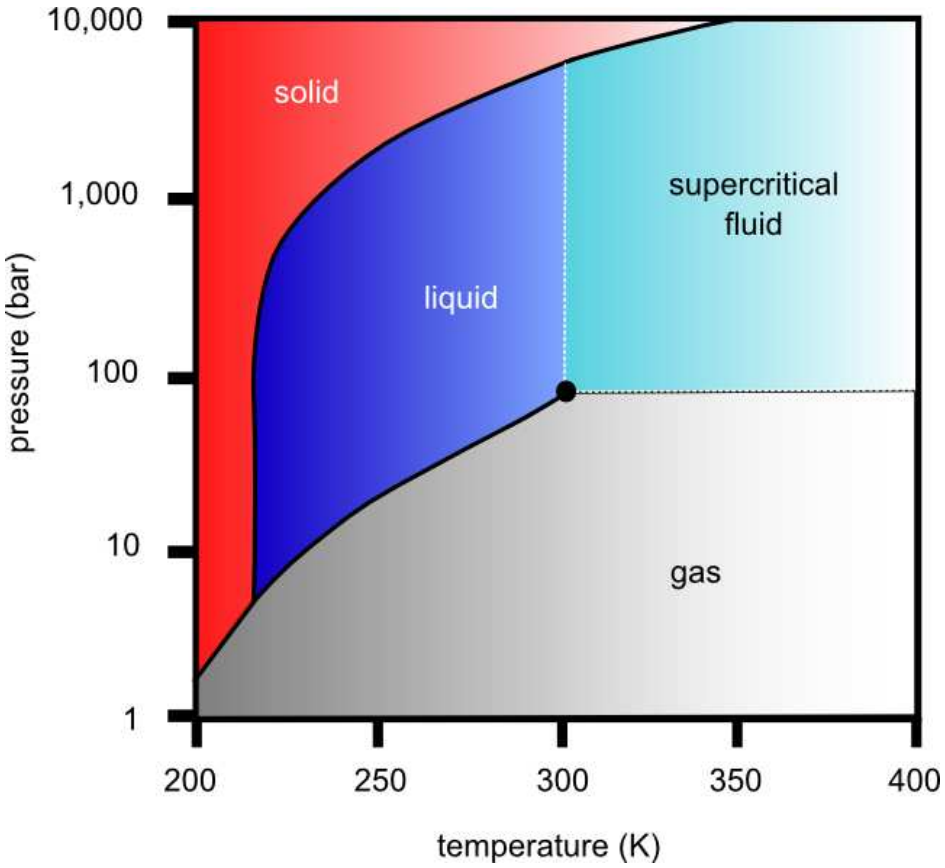

Figure 1.3: Phase diagram of carbon dioxide. (Marc Jacobs, CCL)

of a low dielectric constant and a zero-net dipole moment, scCO_2 is a very poor solvent (essentially a nonsolvent) for many organic and polymeric species.

1.2.2 Gas-eXpanded Liquids

While supercritical carbon dioxide systems offer many desirable properties, they require elevated temperatures and high pressures and only allow for the poor solubility of many species. These limitations can be addressed through the use of gas-expanded liquid (GXL) systems (Jessop & Subramaniam, 2007). Gas-eXpanded Liquids (GXLs) are mixtures of an organic solvent and a pressurized gas. In these systems, a liquid solvent (e.g., hexane) is pressurized with a gas (e.g., CO_2) where the gas partitions (dissolves) into the liquid phase to create a solvent mixture at greater than atmospheric pressure but less than the vapor pressure of the pure gas. At low pressures, very little gas is dissolved in the organic phase, however with increases in the applied pressure of the gas, the volume of the liquid phase drastically increases due to the increased solubility of the gas. A commom GXL has been hexane-CO_2 mixtures (Jessop & Subramaniam, 2007); the vapor liquid equilibrium of this hexane-CO_2 mixture, as well as other mixtures, can be predicted using the Peng-Robinson equation of state (Peng & Robinson, 1976; Dixon & Johnston, 1991; Cassel *et al.*, 1997; Saunders & Korgel, 2004). Figure 1.4a demonstrates the volume change of hexane when pressurized with CO_2 such that

$$\frac{\Delta V}{V_o} = \frac{V - V_o}{V_o} \tag{1.5}$$

where V is the total liquid volume at an applied CO_2 pressure and V_o is the liquid volume of neat hexane at atmospheric conditions. As the applied CO_2 pressure increases, the solubility of CO_2 in the organic solvent (in this case, hexane), increases drastically leading to a volume increase and a significant change in the properties of the liquid mixture. The composition and physico-chemical properties (e.g., density, viscosity, diffusivity, solvent strength, and surface tension) of the solvent mixtures can be easily tuned between those of the organic solvent and those of the pure gas by simple variations the applied partial

pressure of the gas (density and molar volume tuning demonstrated in Figure 1.4b). An additional advantage of using these systems involves the recovery and recycle of both the organic phase and gas through simple depressurization.

The solvent strength of GXLs can be tuned between those of the gas and those of the liquid, in part, due to the ability to change the polarity of the solvent mixture. Wyatt *et al.* reported the Kamlett-Taft π^* parameter (a measure of solvent polarity and polarizability) as measured by solvatochromic dyes for CO_2-expanded acetone and methanol (Wyatt *et al.*, 2005). It was found that the addition of CO_2 to those solvents greatly reduced the solvent polarity as CO_2 is a net-zero pole. Jessop and coworkers were able to use gas expanded liquids as switchable solvents for the dissolution and subsequent recovery of flouro-compounds (Jessop *et al.*, 2002). Mcleod *et al.* were able to demonstrate the controllable solvent strength of GXLs through the controlled precipitation of nanoparticles (McLeod *et al.*, 2005b).

Mass transport properties of gas-expanded liquid systems have been shown to be tunable with the applied system pressure of the selected gas. The diffusion coefficient of benzene in CO_2-expanded methanol was reported to be enhanced between 4 and 5 fold with CO_2 addition (Sassiat *et al.*, 1987). Likewise, the diffusivities of pyridine, pyrimidine, pyrazine, and 1,3,5-triazine in CO_2-expanded methanol increased with applied CO_2 pressure (Maxey, 2006). Kho *et al.* reported the measured viscosities of CO_2-expanded fluorinated solvents and found a 4-5 fold decrease with CO_2 addition (Kho *et al.*, 2003). Hsu *et al.* found the surface tension of CO_2-expanded n-hexane decreased by two orders of magnitude with CO_2 addition (Hsu *et al.*, 1985).

1.2.3 Nanoparticle Processing using Tunable Solvent Systems

A variety of methods have been employed to produce micro and nanoparticles of various polymers, organic and inorganic materials based on technologies that utilize the CO_2 expansion of a solution, including precipitation with a compressed antisolvet (PCA), gas

(a)

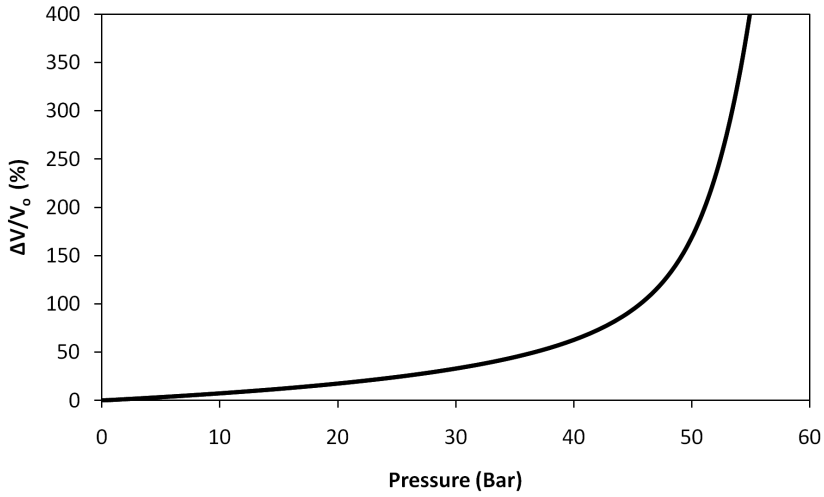

(b)

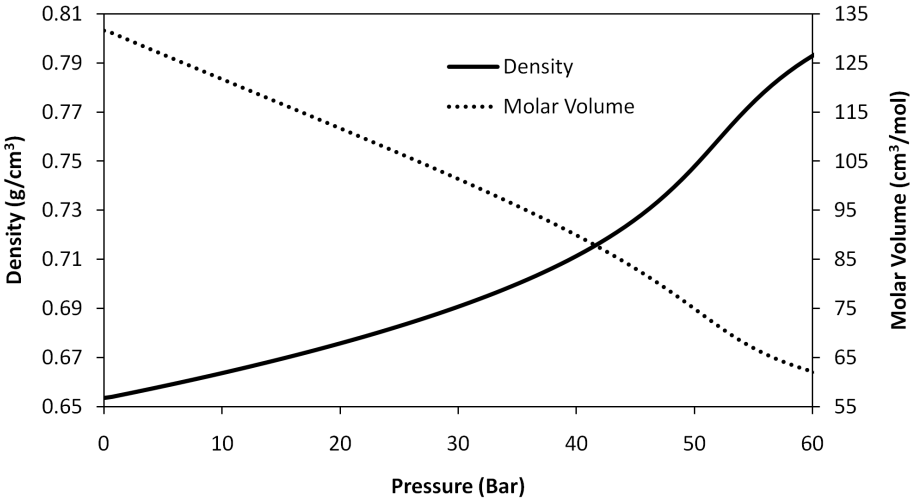

Figure 1.4: Hexane and CO_2 at 25°C as predicted by the PR-EOS: (a) Volume Expansion of the liquid phase and (b) solvent mixture density and molar volume with pressurization of CO_2

or supercritical antisolvent precipitation (GAS or SAS, respectively), depressurization of an expanded liquid organic solution (DELOS), and others. These technologies commonly employ CO_2 as an antisolvent to induce preciptitation from saturated organic solvent solutions. A number of extensive reviews are available in the literature (Tom & Debenedetti, 1991; Subramaniam *et al.*, 1997; Palakodaty & York, 1999; Reverchon, 1999; Cooper, 2000; Marr & Gamse, 2000; Jung & Perrut, 2001b; Tan & Borsadia, 2001; Stanton *et al.*, 2002; Ye & Wai, 2003; Yeo & Kiran, 2005) that address these techniques, and as such, will not be addressed in this chapter.

GXLs also hold potential as media for inorganic nanoparticle synthesis due to reasonable solubilities of material precursors, capping agents, and reducing agents, such as hydrogen. For example, CO_2-expanded heptane has been used as a synthesis medium to synthesize silver nanoparticles from a silver isostearate precursor and hydrogen, both of which are soluble in the GXL (Hsieh *et al.*, 2010). The authors report that by using the silver isostearate precursor in CO_2-expanded heptane, nanoparticles with a diameter of 2.64 ± 0.51 nm were effectively synthesized which were smaller and more narrow in size distribution than analogous nanoparticles synthesized in liquid heptane. This technique takes advantage of the enhanced hydrogen gas solubility in the GXL in order to acheive reduction of the silver ions.

The use of tunable solvents as a processing medium for nanoparticles has received a great deal of attention over the last several years due to typical nanomaterial processing methods being very solvent and time intensive (Shah *et al.*, 2004). Several groups have demonstrated the ability to size-selectively disperse 1-dodecanethiol capped silver and gold nanoparticles in supercritical ethane by tuning the density of the supercritical medium (Clarke *et al.*, 2001; Shah *et al.*, 2002b; Williams & Satherley, 2009). Through variations in the applied ethane pressure, the density (and thus, in this case, the solvent strength) of the supercritical media was adjusted, allowing larger nanoparticles to be dispersed at higher pressures (higher density). However, this method

requires a system pressure of 414 bar to disperse nanoparticles that have a maximum diameter of approximately 3.7 nm due to the feeble solvent strength of supercritical ethane. Alternatively, Han and coworkers have demonstrated a technique to controllably precipitate ZnS nanoparticles from AOT reverse micelles (w/o), dispersed in a continuous isooctane phase, by expanding the isooctane phase with CO_2 (Zhang *et al.*, 2001). Applying a similar technique, McLeod *et al.* controllably precipitated lauric acid and 1-dodecanethiol capped gold and silver nanoparticles from an organic (hexane) dispersion using CO_2 as an antisolvent (McLeod *et al.*, 2005a).

McLeod *et al.* demonstrated that when an organic dispersion of nanoparticles is pressurized with CO_2, the CO_2 readily dissolves into the organic phase and acts as an antisolvent, similar to ethanol in the liquid solvent-antisolvent techniques used to size-selectively fractionate nanoparticles. At low applied CO_2 pressures, the gas is poorly soluble in the liquid solvent, but as the pressure is increased the solubility drastically increases allowing for a significant amount of CO_2 to dissolve into the liquid phase. With a significant portion of the solvent mixture being CO_2, the stabilization provided by the solvation of the ligand tails by the solvent is reduced forcing the nanoparticles to precipitate from the dispersion. By slowly increasing the applied CO_2 pressure, nanoparticles could be slowly precipitated from dispersion whereupon uniform wide-area nanoparticle films could be formed as seen in Figures 1.5b and 1.5d. The process consists of a supercritical drying stage to remove the solvent and creates thin films of a significant higher quality than those created from simple dropcasting, Figures 1.5a and 1.5c (McLeod *et al.*, 2005a; Liu *et al.*, 2006).

The Roberts group took this another step further, using this CO_2-expanded solvent nanoparticle precipitation technique to size-selectively fractionate nanoparticles (McLeod *et al.*, 2005b). Using a novel, Archimedes-type spiral, open ended glass tube enclosed in a high pressure vessel, fractions of nanoparticles could be size-selectively precipitated onto precise locations along the tube, demonstrated in Figure 1.6. They discovered that

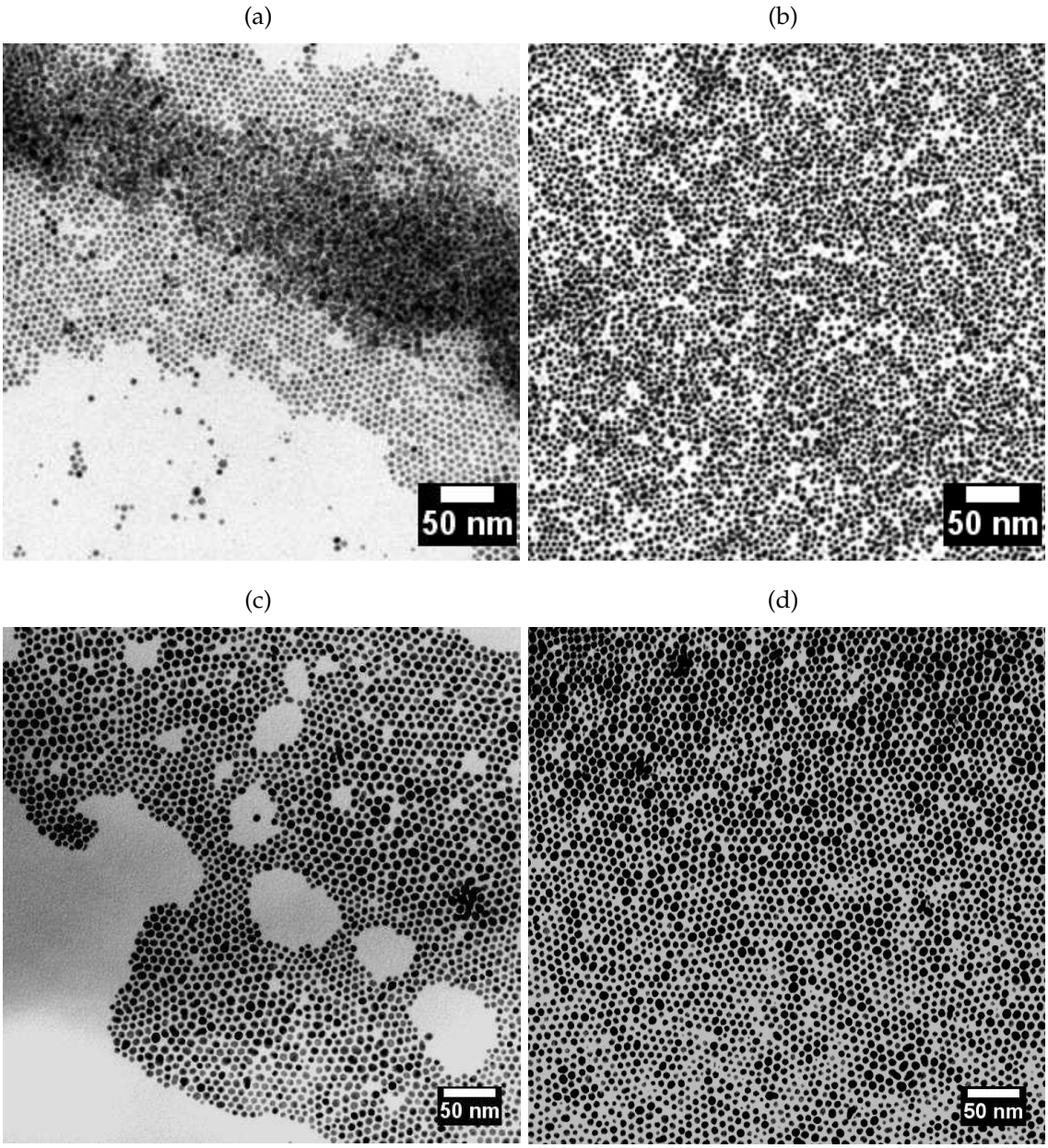

Figure 1.5: DDT-stabilzed silver nanoparticle films deposited via (a) hexane evaporation and (b) GXL nanoparticle deposition. Adapted from (McLeod *et al.*, 2005a). DDT-stabilized gold nanoparticle films deposited via (c) hexane evaporation and (d) GXL nanoparticle deposition. Adapted from (Liu *et al.*, 2006)

as the stabilization of the nanoparticles is reduced (through the addition of CO_2 as a nonsolvent), the van der Waals forces of attraction between the nanoparticles dominates and forces the nanoparticles to precipitate (Anand *et al.*, 2008). Nanoparticles with the largest van der Waals forces of attraction (i.e., the largest nanoparticles) would precipitate first, as they require less CO_2-disruption to overcome the stabilization offered by solvation of the ligand tails. By finely controlling the applied CO_2 pressure, an effective nanoparticle fractionation could be performed without the solvent waste being produced that typical nanoparticle fractionation techniques produce, nor requiring centrifugation due to the increased diffusivity of the nanoparticles through the CO_2-expanded solvent and reduced viscosity.

Anand *et al.* performed a comprehensive study on the effects of solvent length, capping ligand length, temperature, and repeated fractionations on this size-selective fractionation technique, see Figure 1.7 (Anand *et al.*, 2005). Longer solvents (octane as compared to pentane) offers a greater stabilizing force hence higher pressures are needed to precipitate the nanoparticles. Likewise, longer ligand capping agents (1-dodecanethiol as compared to 1-hexanethiol) help to keep the nanoparticles dispersed thus requiring a larger applied CO_2 pressures to precipitate the nanoparticles. It should be noted that ligands longer then C13 (1-tetradecanethiol) demonstrate a decrease in nanoparticle stabilibity, theoretically due to folding of the ligand onto itself. Increasing the temperature of the system, decreases the vapor density of the CO_2, thus requiring larger applied CO_2 pressures to reach the same liquid phase compositions needed to precipitate the nanoparticles. Recursive fractionations also proved to produce fractions with a more narrow size-distribution.

An additional novel separation operation for GXLs has been termed Organic-Aqueous Tunable Solvents (OATS) which are distinguished by the use of a polar solvent that is completely miscible with water at ambient pressures (Lu *et al.*, 2004; Hallett *et al.*, 2006; Hill *et al.*, 2007; Blasucci *et al.*, 2010). With the addition of CO_2, which prefers an organic

(a)

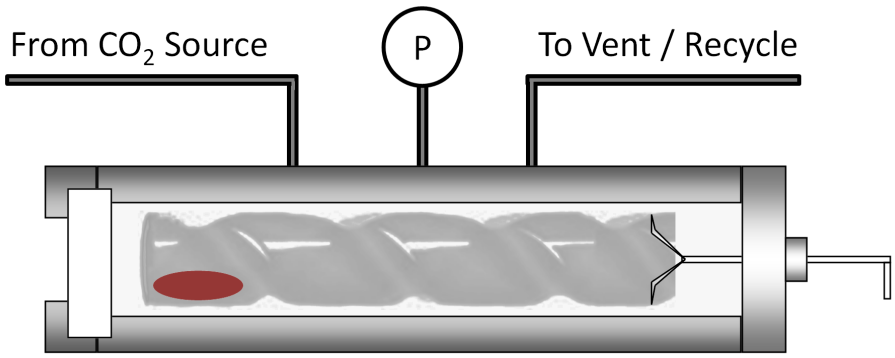

(b)

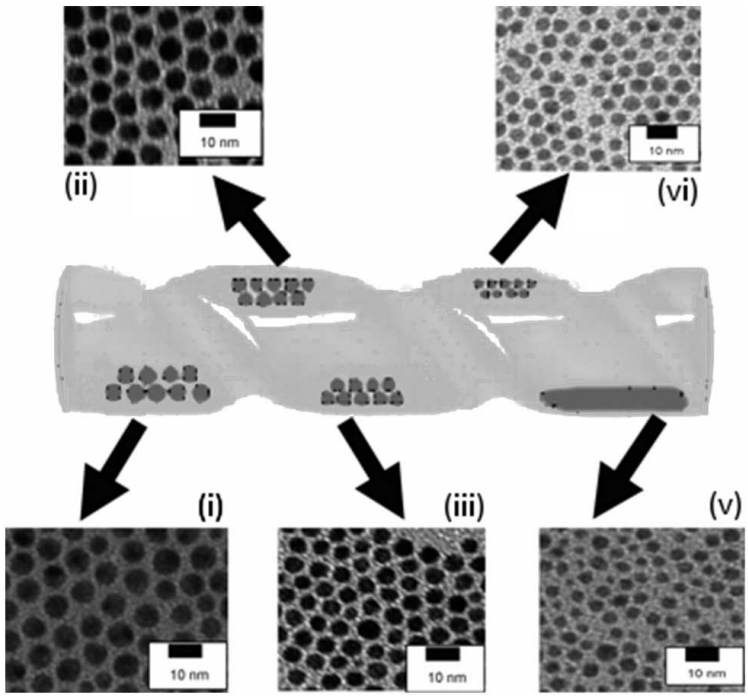

Figure 1.6: (a) Apparatus to size-selectively fractionate small quantities of nanoparticles using the GXL fractionation technique. Adapted from (McLeod *et al.*, 2005b). (b) TEM micrographs of DDT-stabilized silver nanoparticles fractionated from hexane using the GXL fractionation technique in the small-scale spiral tube apparatus. The nanoparticle fractions were collected at applied CO_2 pressure of (i) 0 - 37.9 bar, (ii) 37.9 - 41.4, (iii) 41.4 - 43.1, (vi) 43.5 - 44.8, (vi) 44.8-48.3. Reproduced from (Anand *et al.*, 2005)

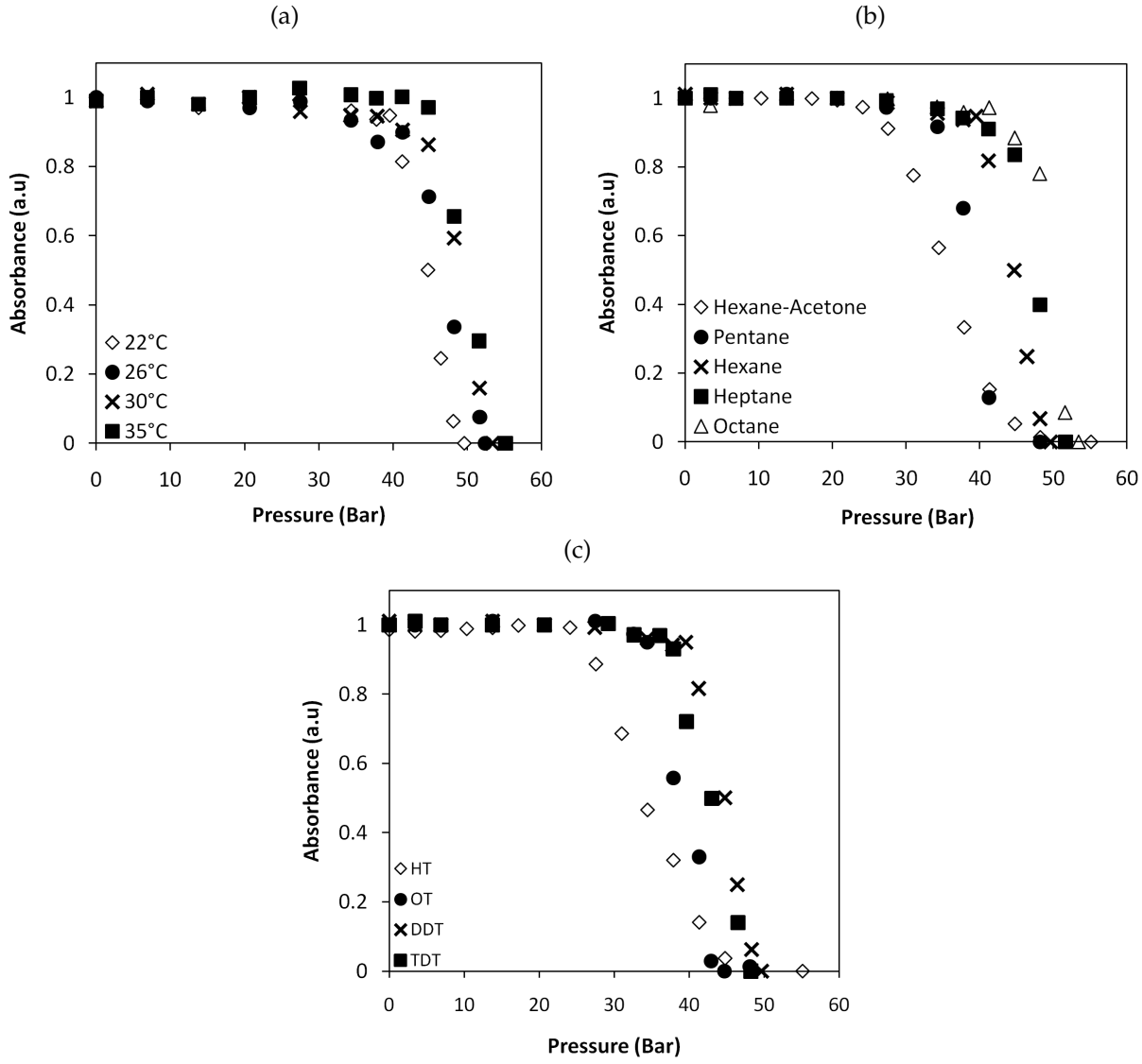

Figure 1.7: Effect of various factors on nanoparticle dispersion (as determined by tracking the intensity of the SPRB) as a function of applied CO_2 pressure. a) Effect of temperature on DDT-stabilized gold nanoparticles dispersed in hexane, b) Effect of solvent on DDT-stabilized gold nanoparticles at room temperature, and c) Effect of ligand on gold nanoparticles dispersed in hexane at room temperature. HT - Hexanethiol, OT - Octanethiol, DDT - Dodecanethiol, TDT - Tertdecanethiol. Adapted from (Anand *et al.*, 2005)

phase, the polarity of the organic decreases to the point that a phase separation occurs. This technique may also be beneficial for nanoparticle ligand exchange reactions where the nanoparticles need to be transferred from an aqueous phase to an organic phase without transitioning a phase boundry.

1.3 Thermodynamic Modeling of Nanoscale Systems

In order to better understand how certain processes function, it is necessary to develop fundamental thermodynamic models that are capable of accurate predictions. These models can offer insight as to what causes nanoparticles to precipitate or can help predict specific sizes of nanoparticles that would precipitate at a given set of solvent conditions. Many different methods of modeling nanoscale systems are available; however, the two of interest are total interaction energy models and stochastic simulations.

1.3.1 Total Interaction Energy

One method of modeling nanoparticle dispersions is through the adaptation of a model set forth by Shah *et al.* in which the total potential energy of the system is minimized. Nanoparticles, which do not create an electric or magnetic field, experience three forces which act upon the nanoparticles to maintain a dispersion: van der Waals forces of attraction, an osmotic repulsive force, and an elastic repulsive force (Shah *et al.*, 2002a; Shah *et al.*, 2002b). The van der Waals force of attraction is due to an electrostatic attraction between dipoles that exist for the metal atoms which constitute the nanoparticles and is well predicted by methods set forth by Hamaker (Hamaker, 1937). The van der Waals force of attraction is dependent upon the geometry of the system, size of the nanoparticles, separation distance between nanoparticle, and solvent conditions. The osmotic repulsive force arises due to solvation of the stabilizing ligand by the solvent as well interactions with other ligand tails (Vincent *et al.*, 1980; Vincent *et al.*, 1986). The osmotic repulsive force was modeled by Vincent *et al.* by an energy balance (free energy) between solvent-ligand

and ligand-ligand interactions and is highly dependent on solvent conditions and ligand length. The elastic repulsive force arises due to the entropic loss upon compression of the stabilizing ligands (Vincent *et al.*, 1980; Vincent *et al.*, 1986). The sum of these three potential energies provides the total interaction energy for two interacting nanoparticles. If this interaction energy is greater than the minimum threshold energy of $-3/2k_BT$ the nanoparticles possess enough energy to maintain Brownian motion and stay dispersed in a solvent, however if this total interaction energy is less than the minimum threshold energy, the nanoparticles will precipitate from dispersion as they do not have enough energy to stay dispersed. This method was used by Kitchens *et al.* to study copper nanoparticle size in conventional solvents (Kitchens *et al.*, 2003) as well as in compressed propane (Kitchens & Roberts, 2004), by Shah *et al.* to study gold and silver nanoparticle size in supercritical ethane (Shah *et al.*, 2002b) and supercritical CO_2 (Shah *et al.*, 2002a), and by Anand *et al.* to study silver nanoparticle size in CO_2 gas-expanded hexane (Anand *et al.*, 2008).

1.3.2 Stochastic Simulations

Nanoscale systems are very complex, and as such, simple models cannot capture the wide range of possible interactions. For example, the total interaction energy as presented above only captures the interactions between two nanoparticles of the same size, with the same ligand surface coverage. In real nanoparticle systems, the size of the nanoparticles in solution would be represented by a size distribution and surface coverage would not be constant across different nanoparticles. In addition, multiple nanoparticles of different sizes would interact in solution. To be able to capture this wide range of possible interactions stochastic computer simulations need to be used. Romero-Cano *et al.* used a Brownian dynamics simulation between two similarly sizes polystyrene nanoparticles (Romero-Cano *et al.*, 2000) to measure colloidal stability. Schapotschnikow *et al.* used a molecular simulation approach on several gold nanoparticles of the same size to predict

the potential of mean force (Schapotschnikow *et al.*, 2008). The amount of stochastic simulation in the nanoparticle field is still very limited as a debate exists as to whether it is best to model these systems at a molecular level or at a microscopic level.

1.4 Summary of Chapters

The goal of this work is to better understand the fundamentals of nanomaterial science through advancing the current state of the art in nanomaterial processing through the use of tunable solvent systems. This will be accomplished with several projects: (1) size-selective fractionation of application scale quantities of nanoparticles, (2) exploring the effect of varying the ligand length and solvent composition on the precipitation and fractionation of nanoparticles, (3) development of a basic thermodynamic model to predict the nanoparticle size that can be dispersed at a given set of solvent conditions, and (4) development of a robust thermodynamic model that includes a statistical method of predicting nanoparticle size distributions that can be recovered from a fractionation process.

1.4.1 Chapter 2 - Size-Selective Fractionation of Nanoparticles at an Application-Scale using CO_2 Gas-eXpanded Liquids

Size-based fractionation of nanoparticles remains a non-trivial task for the preparation of well-defined nanomaterials for certain applications and fundamental studies. Typical fractionation techniques prove to be inefficient for larger nanoparticle quantities due to the expense of equipment, low-throughput, and/or the amount of organic solvent waste produced. Through the use of the pressure-tunable physico-chemical properties of CO_2-expanded liquids, a rapid, precise, and environmentally sustainable size-selective fractionation of ligand-stabilized nanoparticles is possible through simple variations in applied CO_2 pressure. An apparatus capable of fractionating large quantities of thiol-stabilized nanoparticles into distinct fractions (targeted mean diameters with narrow

distributions) has been developed. This apparatus consists of three vertically mounted high pressure vessels connected in series with high pressure needle valves. This process at current design scales, operated at room temperature, and CO_2 pressures between 0 and 50 bar, results in a batch size-selective fractionation of a concentrated nanoparticle dispersion. This chapter presents this new apparatus, separation results of various single pass fractionations as well as for recursive fractionations, and methods for targeting fractions to specific sizes and standard deviations.

1.4.2 Chapter 3 - Tuning the Precipitation and Fractionation of Nanoparticles in Gas-eXpanded Liquid Mixtures

Previous investigations have demonstrated that through the use of the pressure-tunable physico-chemical properties of CO_2-expanded liquids, a rapid, precise, and environmentally sustainable size-selective fractionation of significant quantities of ligand-stabilized nanoparticles can be achieved through simple variations in applied CO_2 pressure. Unfortunately, an applied CO_2 pressure upwards of 35 bar has previously been required to precipitate 1-dodecanethiol stabilized gold nanoparticles from an n-hexane dispersion. However, this chapter demonstrates that the pressure required to induce nanoparticle precipitation can be tuned towards lower overall operating pressures by varying the length of the stabilizing ligand and/or the composition of the solvent. For example, a certain amount of a liquid antisolvent (e.g., acetone) can be introduced into a stable dispersion of nanoparticles in n-hexane such that the solvent strength of the liquid mixture (e.g., n-hexane + acetone) is reduced to near the threshold of nanoparticle precipitation prior to CO_2 addition. As such, these liquid solvent mixtures require an applied CO_2 pressure of only 20 bar to induce nanoparticle precipitation as opposed to the higher pressures necessary for the same nanoparticle dispersion in neat n-hexane. Moreover, changing the stabilizing ligand from 1-dodecanethiol to 1-hexanethiol allows for the precipitation of nanoparticles from a mixture of n-hexane and acetone to occur at

applied CO_2 pressures of less than 5 bar. This chapter will demonstrate that this technique allows for greater control of the stability of the nanoparticle dispersions allowing for a higher degree of precision when performing size-selective fractionations. Additionally, an empirical method of predicting the average diameter of recovered fractions from a size-selective fractionation process in these CO_2-expanded solvent mixtures is discussed.

1.4.3 Chapter 4 - Thermodynamic Analysis of Nanoparticle Size-Selective Fractionation using Gas-eXpanded Liquids

A thermodynamic model was developed for the size-selective fractionation of ligand stabilized nanoparticles using a CO_2 gas-expanded liquid precipitation process. The tunable solvent strength of gas-expanded liquids, via CO_2 pressurization, results in an effective method to fractionate nanoparticles, based on the size dependant dispersibility of the nanoparticles. Specifically, the thermodynamic model is used to estimate the size of 1-dodecanethiol stabilized silver nanoparticles that can be dispersed at a given CO_2 pressure by equating the total inter-nanoparticle interaction energy to the Boltzmann threshold stabilization energy ($-3/2k_BT$). The ligand-solvent interaction is found to have the greatest impact on the total interaction energy. This model illustrates that the entire length of the ligand is not accessible to the solvent and three phenomenological model variations were developed to vary the ligand-solvent interaction. This chapter presents this model, as developed by Madhu Anand, Seong-Sik You, Steven Saunders and others (Anand *et al.*, 2008).

1.4.4 Chapter 5 - Modeling the Precipitation of Polydisperse Nanoparticles Using a Total Interaction Energy Model

A thermodynamic model is presented that can accurately predict, typically within 5%, the average size and size distribution of size-selectively precipitated nanoparticles. A total interaction energy model was developed which accounts for: (1) the interaction of two

differently sized ligand-stabilized nanoparticles in a solvent plus antisolvent mixture, (2) the collapsing of the ligand shell as the solvent strength of the mixture decreases, and (3) the variability of the ligand surface coverage of the nanoparticle. A total interaction energy model equates the sum of potential energies for all forces acting on a nanoparticle pair (van der Waals attractive, osmotic repulsive, and elastic repulsive) to that of the Brownian motion threshold energy in order to predict the nanoparticle size combinations that can be dispersed or would be precipitated under varying solvent conditions. Combining this with simple probabilities describing the frequency of combinations between differently sized nanoparticles leads to average sizes and distributions of precipitated and dispersed nanoparticles at various solvent conditions. The application of this model has been successfully demonstrated by the size-selective fractionation of 1-dodecanethiol stabilized gold nanoparticles dispersed in hexane and precipitated by the addition of CO_2.

Chapter 2

Size-Selective Fractionation of Nanoparticles at an Application Scale Using CO_2 Gas-eXpanded Liquids

2.1 Introduction

Materials with nanoscale dimensions exhibit very unique mechanical, chemical, magnetic, electronic, and optical properties which are found neither at bulk scales nor at the molecular scale (Adair *et al.*, 1998). These unique properties are often found to be highly size-dependent, and as such, obtaining monodisperse samples of nanoparticles of a desired size is of the utmost importance for certain applications and fundamental studies. While it is possible to synthesize monodisperse nanoparticles, most notably through controlled growth methods (e.g., citrate reduction (Turkevich *et al.*, 1954; Frens, 1973) and seeded growth (Jana *et al.*, 2001c)) these methods are typically tailored for a particular material and produce low-concentration, aqueous dispersions of nanoparticles which are challenging to process. Thus, post-synthesis processing methods for obtaining monodisperse fractions are required that will be applicable to many different types of materials and that offer high throughputs. Current post-synthesis processing methods used to obtain monodisperse fractions from polydisperse samples include size-exclusion liquid chromatography (Wilcoxon *et al.*, 1998), high-pressure liquid chromatography (Fischer *et al.*, 1989; Jimenez *et al.*, 2003), isoelectric focusing electrophoresis (Arnaud *et al.*, 2005), gel electrophoresis (Hanauer *et al.*, 2007), and diafiltration (Sweeney *et al.*, 2006). However, each of these methods require expensive and specialized equipment and provide relatively low throughputs. A common technique used to size-selectively fractionate nanoparticles involves the use of a liquid solvent-antisolvent fractionation through an induced precipitation which requires centrifugation and produces large

quantities of organic waste (Murray *et al.*, 2000; Murray *et al.*, 2002). At application relevant processing scales (greater than milligram quantities), centrifugation is both inefficient and expensive. As an additional drawback, these processes produce large quantities of organic solvent waste which would be expensive to dispose of or require large amounts of energy to separate, thus making a liquid solvent-antisolvent a non-optimal solution. Through the use of Gas-eXpanded Liquids (GXL's), a similar system is possible without requiring centrifugation nor producing solvent waste.

Gas-expanded liquids are mixtures of an organic solvent and a pressurized gas (Eckert *et al.*, 2000; Jessop & Subramaniam, 2007). In these systems, an organic solvent (e.g., hexane) is pressurized with a gas (e.g., CO_2) where the gas partitions (dissolves) into the liquid phase to create a solvent mixture at greater than atmospheric pressure but less than the vapor pressure of the pure gas. At low applied pressures, very little gas is dissolved in the organic phase, however with increases in the applied pressure of the gas, the volume of the liquid phase drastically increases due to the increased solubility of the gas. The composition and physico-chemical properties (e.g., density, viscosity, diffusivity, solvent strength, surface tension, etc.) of the solvent mixtures can be easily tuned between those of the organic solvent and those of the pure gas by simply varying the applied pressure of the gas. An additional advantage of using these systems involves the recovery and recycle of both the organic phase and the gas through simple depressurization.

In previous studies (Anand *et al.*, 2005; McLeod *et al.*, 2005b; Anand *et al.*, 2007; Anand *et al.*, 2008), CO_2 was used as an antisolvent in a gas-expanded hexane system to size-selectively precipitate ligand (1-dodecanethiol and tri-n-octylphosphine oxide) stabilized nanoparticles (metal and semiconductor, respectively) into narrow sized fractions through simple variations in applied CO_2 pressure. Nanoparticles disperse in a solvent when the solvent-ligand interaction provides a sufficient repulsive force (osmotic repulsive force due to the solvation of the ligand tail by the solvent) to overcome the inherent van der Waals attractive forces between the ligand-stabilized nanoparticles (Vincent

et al., 1980; Vincent *et al.*, 1986; Shah *et al.*, 2002a; Shah *et al.*, 2002b; Kitchens *et al.*, 2003). The degree of solvent-ligand interaction can be reduced upon the gradual addition of CO_2, a known nonsolvent (i.e., antisolvent) for nonpolar, aliphatic ligands, through pressurization thereby enabling a gradual size-dependent precipitation of the nanoparticles. The magnitude of the van der Waals attractive force between nanoparticles scales with the nanoparticle diameter and thus the largest nanoparticles will precipitate first upon worsening solvent conditions (i.e., upon CO_2 addition). To paraphrase, by precisely adjusting the applied CO_2 pressure, the dispersability of nanoparticles can be controlled to obtain increasingly smaller-sizes nanoparticles fractions with increasing CO_2 pressure applied to the organic solvent dispersion. Due to the fact that the GXL solvent mixture's properties lie between those of the gas and those of the solvent, the addition of CO_2 reduces the viscosity (Kho *et al.*, 2003) and increases the diffusivity of the nanoparticles through the medium (Sassiat *et al.*, 1987; Maxey, 2006), thereby allowing precipitation to occur rapidly without the need for centrifugation.

This concept was previously illustrated through the use of an Archimedes-type open-ended spiral-tube placed inside a high pressure vessel within which a polydisperse sample of ligand-stabilized metallic (e.g., gold or silver) or semiconductor (e.g., CdSe/ZnS) nanoparticles could be fractionated into narrow-sized distributions (e.g., SD < 1 nm) using the GXL solvent-antisolvent system (Anand *et al.*, 2005; McLeod *et al.*, 2005b; Anand *et al.*, 2007). The spiral-tube apparatus (glass tube with a concentric, spiral indentation inside a stainless-steel high pressure vessel) was fabricated to allow for the collection of nanoparticle fractions from an initially polydisperse population (McLeod *et al.*, 2005b). The indented channel, or groove, allows for a small volume of a nanoparticle dispersion to rest within a specific area of the tube and easily traverse the length of the spiral channel by rotating the tube about the longitudinal axis. The high pressure apparatus was repeatedly pressurized with CO_2 to precipitate the nanoparticles and the spiral-tube rotated externally 180° to separate the remaining dispersion of smaller nanoparticles from the precipitated

larger nanoparticles which were affixed to the glass surface. This spiral-tube apparatus was initially designed as a proof-of-concept device and was never intended to be scaled-up in this spiral-tube configuration. In order to produce application-scale quantities (greater than milligram quantities) of nanoparticles with a targeted mean diameter and size distribution, this chapter presents a new apparatus that would provide an effective separation at larger scales in a configuration that lends itself to further scale-up.

2.2 Methods and Materials

Chloroform (99.8% purity), silver nitrate ($AgNO_3$, 99.99995%), and tetra-n-octylammonium bromide (TOABr, 98%) were obtained from Alfa Aesar. Deionized ultra filtered water (D-H_2O) and toluene (99.8%) were obtained from Fisher Scientific. Hydrogen tetrachloroaurate trihydrate ($HAuCl_4 \cdot 3\,H_2O$, 99.9+%), sodium borohydride ($NaBH_4$, 99%), hexane (97+%), and 1-dodecanethiol (98+%) were obtained from Sigma-Aldrich. Ethanol (200 proof) was obtained from Pharmco-Aaper. Carbon Dioxide (SCF / SFE grade) was obtained from Airgas. All materials were used as obtained without further purification.

2.2.1 Nanoparticle Synthesis

1-Dodecanethiol stabilized gold and silver nanoparticles were synthesized via the two-phase arrested precipitation method (Brust *et al.*, 1994; Sigman *et al.*, 2004). This method produces nanoparticles ranging in diameter from 2 to 12 nm with a broad size distribution. A typical silver nanoparticle synthesis is as follows: a solution of 0.19 g of $AgNO_3$ in 36 mL of D-H_2O was mixed with an organic solution consisting of 2.7 g of the phase-transfer catalyst TOABr in 24.5 mL of chloroform. This mixture was stirred for one hour or until the aqueous phase was clear and the organic phase appeared milky. The aqueous phase was then removed and 240 μL of 1-dodecanethiol was added and allowed to stir for 5 - 10 min. A freshly prepared solution of 0.5 g of $NaBH_4$ in 30 mL of D-H_2O was added as

the reducing agent and allowed to stir for 4-12 h. The aqueous phase was then discarded leaving an organic dispersion of thiol-stabilized nanoparticles. Gold nanoparticles were synthesized in a similar fashion, however the 0.19 g of $AgNO_3$ was replaced with 0.36 g of $HAuCl_4 \cdot 3\,H_2O$, replacing chloroform with toluene, adding the thiol after the 4-12 h stirring/reducing period, and stirring for an additional 4 h after adding the thiol. A large excess of ethanol was added to the organic dispersion of thiol-stabilized nanoparticles as an antisolvent to wash the nanoparticles. The nanoparticles in the solvent/antisolvent mixture was centrifuged (Labnet Hermle Z200A) at 4500 rpm for 5 min to precipitate the nanoparticles. The supernatant, containing the phase-transfer catalyst and the unbound thiol was discarded. This washing was repeated three times to ensure the nanoparticles were thoroughly cleaned. No liquid solvent-antisolvent size-fractionation was performed at this stage, only cleaning. The nanoparticles were then dispersed in neat hexane. The hexane dispersions of metallic nanoparticles were used for all experiments.

2.2.2 Cascaded-Vessel Fractionation Apparatus

A cascaded-vessel apparatus, schematic shown in Figure 2.1, was designed and fabricated to allow for the fractionation of application-scale quantities of nanoparticle dispersions into monodisperse fractions from an initially polydisperse sample by controlling the location of nanoparticle precipitation induced via CO_2-pressurization. The primary components of this apparatus are three high-pressure, stainless-steel Jerguson gages (R-20) each with an interior volume of approximately 40 mL, labeled Collection Vessel 1, 2, and 3 in Figure 2.1. Side ports were machined into the Jerguson gages to allow delivery of pressurized CO_2 to each vessel independently and to prevent vapor blocks. The fittings for the bottom of the vessels were specially machined with a conical shape to prevent entrainment of liquid when drained. Glass-tube inserts were fabricated to fit into the high pressure vessels and make a liquid-tight seal (Viton o-ring) with the fitting attached to the bottom of the vessel. The vessels are connected to each other in series and

compartmentalized by high-pressure needle valves which allow for the complete isolation of one vessel from the others. A high-pressure syringe pump (ISCO 260D) is used to controllably deliver CO_2 to a desired vessel. Alternatively, a simpler system, without the capability of quantitatively controlling CO_2 flow rates, utilizing a CO_2 tank (under vapor-liquid equilibrium conditions) and regulator could be used as all experiments are conducted below the vapor pressure of CO_2. A pressure transducer attached to the top of the cascade is used to monitor the system pressure. Unlike other current nanoparticle size-fractionation techniques, this apparatus consists of relatively inexpensive and common moderate-pressure equipment.

A significant amount of engineering and consideration has been put into the development and construction of the cascaded-vessel fractionation apparatus. The original version of the apparatus consisted of the three high pressure vessels connected in series via high pressure needle valves. This version failed as when the fluid, under pressurized conditions was to be transferred (drained) to the next vessel a vapor block occurred. The liquid would begin to drain until the downward force of the fluid was equal to the upward force of the gas in the next vessel causing drainage to halt. This was remedied with the addition of the side-ports. The side ports allowed CO_2 to be delivered to each vessel independently while preventing the vapor block. Fractionations with this iteration of the apparatus while preventing vapor blocks did not produce monodisperse fractions. Recovered fractions would always contain nanoparticles that were too small. This was due to the high pressure fittings connected to the bottom of the high pressure vessel having a flat surface. When the fluid containing smaller nanoparticles was to be drained to the next vessel, some of the fluid would be entrained on the vessel contaminating the recovered fraction with smaller nanoparticles that should have been drained to the next vessel. In order the remedy this, the fitting was machined with in a conical drain such that the fluid would be funneled into the next vessel. This modification proved to improve the results but still the recovered fractions were smaller than what

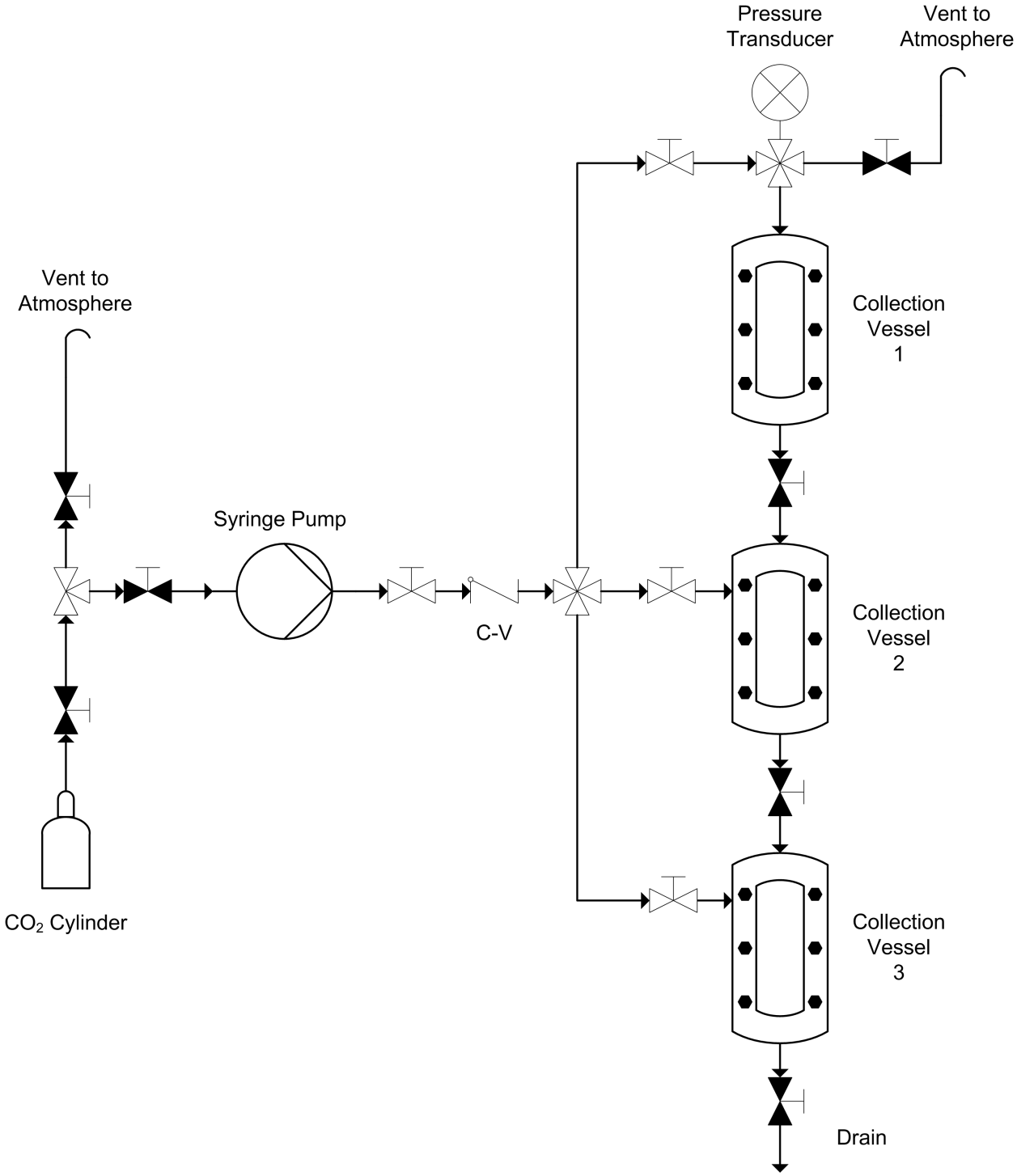

Figure 2.1: Cascaded-vessel apparatus for fractionating application-scale quantities of nanoparticle dispersions.

was expected, it was believed that fluid was still being entrained in the high pressure vessel. Glass-tube inserts were fabricated to fit into the high-pressure vessel and make a liquid-tight seal with the lower high-pressure fitting. The liquid tight seal was provided using several viton o-rings to make a seal between the glass-tube and the high-pressure fitting. With these modifications distinctly sized fractions were obtained.

2.2.3 Size-Selective Fractionation

A typical fractionation was initiated by saturating the apparatus with hexane vapor by rinsing the system with liquid hexane several times and then introducing up to 20 mL of a concentrated nanoparticle-hexane dispersion into Collection Vessel 1; with all the isolation valves closed the nanoparticle dispersion remained in the top vessel. The system was then sealed and all three vessels were pressurized to a CO_2 pressure of P_1, determined *a priori*. The system pressure was carefully controlled by delivering CO_2 from a high pressure syringe pump until the system reached mechanical equilibrium, which could take as long as 90 minutes depending on the magnitude of the pressure increase. During this equilibration period, the largest-sized fraction of nanoparticles, those which could no longer be stabilized in the hexane/CO_2 solvent mixture at an applied CO_2 pressure of P_1, precipitated from solution (Fraction 1) and adhered to the glass-tube inside Collection Vessel 1 via van der Waals interactions. In order to separate the smaller-sized nanoparticles that remained dispersed in the solvent mixture from the larger-sized nanoparticles that had adhered to the glass-tube, the isolation valve separating Collection Vessel 1 and 2 was slowly opened to allow the solvent mixture (at P_1) containing the smaller, still dispersed nanoparticles to drain (via gravity) away from the larger precipitated nanoparticles into Collection Vessel 2. This transfer was performed slowly and at constant pressure (P_1) to ensure that the precipitated nanoparticles (largest sized fraction) were not sheared from the glass-tube insert nor re-dispersed due to a change in system pressure, and therefore solvation strength. After the smaller, still dispersed nanoparticles were transferred to

Collection Vessel 2, the system was again slowly pressurized to an applied CO_2 pressure of P_2, again determined *a priori*. During this second pressurization process the largest nanoparticles that were still dispersed precipitated from solution (Fraction 2). The nanoparticles still capable of being stabilized in the solvent mixture at an applied CO_2 pressure of P_2, were then slowly drained into Collection Vessel 3 (Fraction 3) while maintaining constant pressure throughout the system. The isolation valves between each vessel were then closed and the system was slowly depressurized. The glass-tube inserts were removed from each vessel and separately washed with hexane to collect the precipitated fractions from each respective vessel. Carbon-coated TEM grids were then prepared via drop casting and TEM micrographs were acquired on a Zeiss EM 10 Transmission Electron Microscope and sized using the ImageJ software package.

The ability to target mean diameters and size distributions originates from judiciously selecting the pressure stages, P_1 and P_2. Figure 2.2 demonstrates this concept. Through pressurization at two stages, it is possible to make "pressure slices" through a size distribution. Each precipitation makes a cut through the original sample's size distribution. As seen in Figure 2.2A, P_1 corresponds to a threshold nanoparticle size, nanoparticles larger than this size precipitate in Collection Vessel 1 (Fraction 1) while nanoparticles smaller than this size remain dispersed and transferred to Collection Vessel 2. Fraction 2 consists of the nanoparticles that remained stabilized at P_1 but not at P_2, or the nanoparticles that exist between the P_1 and P_2 pressure slices in Figure 2.2A. This leaves the nanoparticles smaller than the P_2 pressure slice to comprise Fraction 3. When lower pressures are selected for P_1 and P_2 (demonstrated in Figure 2.2B), the pressure slices shift to larger nanoparticle threshold sizes, thus the recovered fractions have larger mean diameters when compared to the corresponding recovered fraction in Figure 2.2A. Likewise, if higher pressures are selected for P_1 and P_2, the recovered fractions would have smaller mean diameters. When the pressure difference between P_1 and P_2 is reduced (demonstrated in Figure 2.2C), the pressure slices approach each other, thus the fraction

recovered in Collection Vessel 2 would have a more narrow size distribution and fractions collected in Collection Vessels 1 and 3 would have wider size distributions when compared to the recovered fractions in Figure 2.2A.

Detail on a method of predicting the fractionation pressures to acheive a specific sized sample is discussed in Chapter 3 and Appendix A.

2.3 Results

An original sample of 20 mL (approximately 300 mg of metal) of 1-dodecanethiol-stabilized gold nanoparticles dispersed in hexane was used for a single pass fractionation. Previous UV-vis studies of gold nanoparticle dispersions in CO_2-expanded hexane revealed that nanoparticle precipitation occurs gradually between applied CO_2 pressures of 40 - 49 bar (Anand *et al.*, 2005). Pressure intervals for this fractionation were selected as 0 - 42.7 bar (Fraction 1) and 42.7 - 45.5 bar (Fraction 2). Nanoparticles that could not be precipitated at 45.5 bar were also collected (Fraction 3). The pressure interval for the first fraction was chosen such that there is a small difference between the pressure necessary to induce nanoparticle precipitation (i.e., the onset of nanoparticle precipitation) and the final pressure of that fractionation stage such that a narrow fraction would be obtained. The pressure interval for the second fraction was chosen such that it would provide a fraction with a similar mean diameter to that of the original sample but more narrow in terms of standard deviation. It is convenient to describe an experimental run in terms of the pressure change of the second fraction ΔP ($= P_2 - P_1$) and the median pressure of the second fraction P_2^m $\left(= \frac{P_2+P_1}{2}\right)$. TEM micrographs and size distributions of the original sample and each fraction can be seen in Figure 2.3. At least 1000 nanoparticles from several different locations on each TEM grid were sized such that a statistically relevant sample of the fraction population was analyzed. A statistical summary of the size distributions of both the original sample and three collected fractions can be seen in Table 2.1A.

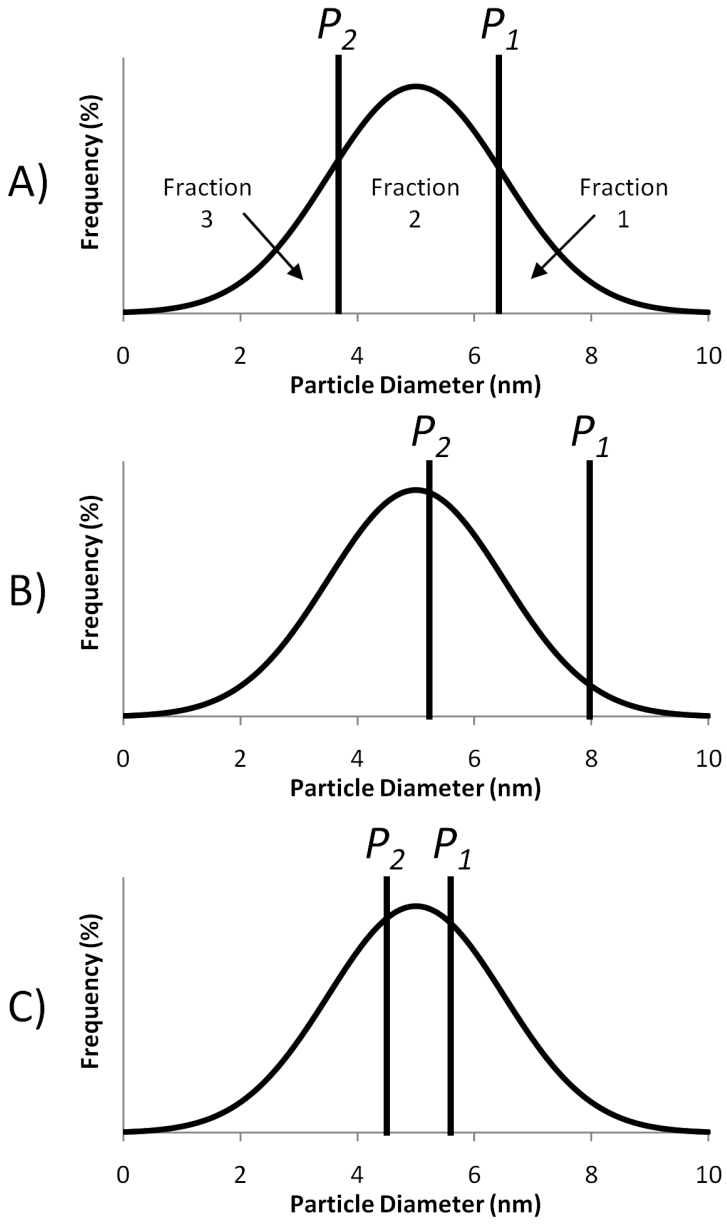

Figure 2.2: Demonstration of the ability to target a desired mean diameter and size distribution. (A) Fractionated prototypical size distribution, (B) Controlling mean diameters: by lowering P_1 and P_2 a larger mean diameter for all three fractions is obtained compared to the respective fractions produced in (A), and (C) Controlling size distribution: by narrowing the pressure difference between P_1 and P_2, Fraction 2 is more monodisperse than the respective fraction in (A).

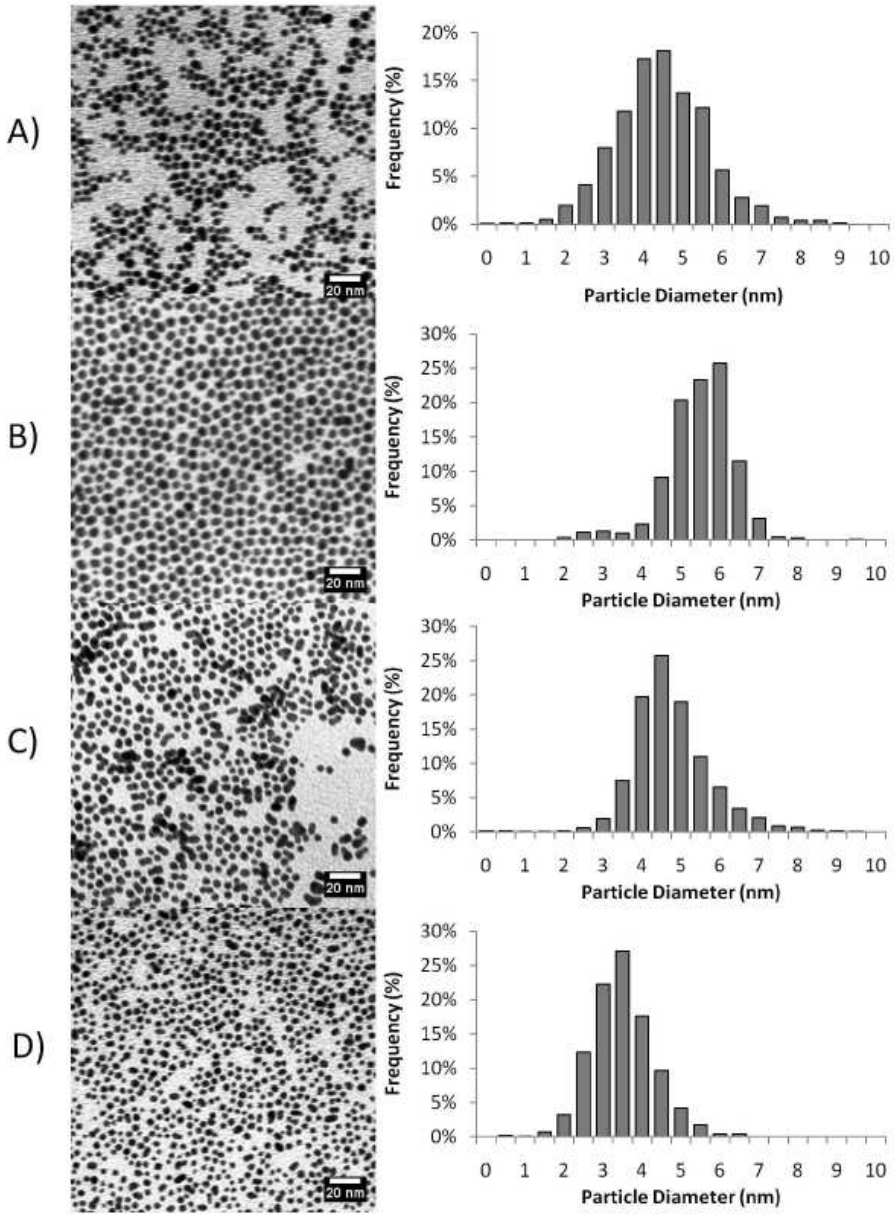

Figure 2.3: TEM micrographs and size distributions of a single pass fractionation of dodecanethiol-stabilized gold nanoparticles using CO_2-expanded hexane. (A) Original sample, (B) nanoparticles precipitated between 0 - 42.7 bar, (C) nanoparticles precipitated between 42.7 - 45.5 bar, and (D) nanoparticles collected that were not precipitated at 45.5 bar. Scale bars are 20 nm.

	Experiment		Pressure Interval	Mean Diameter	Standard Deviation	PDI	Number of Nanoparticles Sized
#	ΔP (Bar)	P_2^m (Bar)	(Bar)	(nm)	(nm)		
Original Sample				4.70	1.20	1.07	1218
	N/A	N/A	0-42.7	5.73	0.85	1.02	1222
A	2.8	44.1	42.7-45.5	5.02	0.99	1.04	1656
	N/A	N/A	45.5+	3.75	0.81	1.05	1708
	2.8	44.1	42.7-45.5	5.20	0.99	1.04	1656
B	1.4	44.1	43.4-44.8	5.20	0.92	1.03	1071
	0.7	44.1	43.8-44.5	4.87	0.66	1.02	1423
	1.4	43.4	42.7-44.1	5.32	1.11	1.04	1242
C	1.4	44.1	43.4-44.8	5.20	0.99	1.04	1656
	1.4	44.8	44.1-45.5	5.07	0.71	1.02	1253

Table 2.1: Statistical summary of single pass fractionations of gold nanoparticles. (A) All three collected fractions from one pass, (B) second fractions from several different passes, varying ΔP, and (C) Second fractions from several different passes, varying P_2^m.

It is proposed that a polydispersity index (PDI), similar to that used in the polymer industry, could be used to compare the broadness in size distribution of nanoparticle samples with differing mean diameters rather than relative standard deviation (RSD) since small changes in nanoparticle diameter causes significant changes in RSD. The polydispersity index provides a normalized measure of the broadness of a size distribution. The PDI is the ratio of the diameter-weighted average diameter $\overline{D_W}$ of a nanoparticle sample to the number average diameter $\overline{D_N}$ of a nanoparticle sample.

$$PDI = \frac{\overline{D_W}}{\overline{D_N}} \tag{2.1}$$

where

$$\overline{D_W} = \frac{\sum_i D_i^2}{\sum_i D_i} \tag{2.2}$$

$$\overline{D_N} = \frac{\sum_i D_i}{n} \tag{2.3}$$

where D_i is the diameter of a specific nanoparticle in a sizing sample and n is the total number of nanoparticles in a sizing sample. A truly monodisperse sample, where all nanoparticles are exactly the same size has a PDI of unity, however, as a sample becomes more polydisperse the PDI increases.

As can be seen qualitatively in Figure 2.3 and more quantitatively in Table 2.1A, three very distinct fractions are obtained. In fact, this is the same general result obtained using the previous bench-top (spiral-tube) apparatus even at these larger processing scales. The first fraction of nanoparticles (those collected between 0 - 42.7 bar) are the largest nanoparticles and the most monodisperse (by PDI) of the recovered fractions due to the small difference in pressure between the onset of nanoparticle precipitation and the end of the pressure interval (P_1). The second fraction (those nanoparticles collected between 42.7 - 45.5 bar) has a similar mean diameter (within 0.35 nm) but a more narrow distribution when compared to the original sample. The third recovered fraction has the smallest standard deviation of 0.81 nm, an improvement of 32.5% over the original

sample demonstrating that this method is capable of improving the monodispersity of large quantities of a nanoparticle dispersion. Thermogravimetric analysis (TGA) of the recovered fractions was performed to determine metal concentration of the dispersions. It was found that 98% (by mass) of the metal introduced into the apparatus was recovered after GXL fractionation. It is believed that the remaining 2% was trapped in valves where simple hexane washings were not able to redisperse the nanoparticles. The entire fractionation process was performed over the course of 4 hours, limited primarily by the diffusion of CO_2 into the organic phase.

Along with the single pass results already presented (Table 2.1A), several additional fractionations were performed where the pressure intervals were varied in order to investigate the controllability of the technique to provide samples with targeted mean diameters and size distributions. First, several fractionations (using a sample from the same original nanoparticle dispersion as above) were performed where the pressure difference of the second fraction (ΔP) was adjusted while maintaining the median pressure of the second fraction (P_2^m). Presented in Table 2.1B is the statistical summary of these fractionations. As the nanoparticles recovered from the second fraction would be the desired product, only the values for the second fraction are shown in Table 2.1B. It was found that as the pressure range of the second fraction is narrowed, the recovered fraction becomes more monodisperse (decreasing standard deviation and PDI) while maintaining a relatively constant mean diameter. Similarly, fractionations were performed (Table 2.1C) in which the median pressure of the second fraction (P_2^m) was varied while maintaining a constant pressure difference (ΔP). It was found with increasing the median pressure, smaller particles were recovered while maintaining constant monodispersity (PDI remains constant). Thus, it is possible to produce fractions with targeted mean diameters and distributions by simply choosing appropriate pressures.

In order to investigate the efficacy of this fractionation technique, recursive fractionations were performed over the same pressure intervals. 1-Dodecanethiol-stabilized silver nanoparticles dispersed in hexane were fractionated at pressure intervals of 0 - 43 bar and 43 - 45 bar. The nanoparticles that could not be precipitated at 45 bar were also collected. These pressure intervals were chosen such that the second fraction would be the most narrow of the three recovered fractions and have an mean diameter similar to that of the original sample. After one fractionation, the nanoparticles collected between 43 - 45 bar were reintroduced into Collection Vessel 1 and re-fractionated at the same pressure intervals to see if the distribution would change as a result of the recursive (repeated) fractionations. A total of three fractionations were performed at the same pressure intervals, each time collecting and analyzing Fraction 2 (nanoparticles precipitated between 43 - 45 bar). TEM micrographs and size distributions of the original sample as well as the second fraction from each pass can be seen in Figure 2.4. At least 1000 nanoparticles from several different locations on each TEM grid were sized such that a statistically relevant sample of the population was analyzed. Statistical summaries of the size distributions are presented in the insets of Figure 2.4. Relative standard deviations are reported in Figure 2.4 as the mean diameters are relatively uniform. Therefore, relative standard deviation is an acceptable normalized measure of the broadness of a distribution in this situation.

Each recursive fractionation produced incrementally more monodisperse fractions. The standard deviation of each recovered fraction decreased with each successive fractionation, improving by 36% after one pass, 43% after two passes, and finally, 55% after three passes when compared to the original sample. This is due to the interactions between nanoparticles of different sizes being reduced after each successive fractionation. The fractions become monodisperse enough to begin to locally self-assemble into close packed hexagonal-arrays on the TEM grid upon drop-casting. More than 35% of the nanoparticles, recovered after three passes, are within 5% of the mean diameter which is

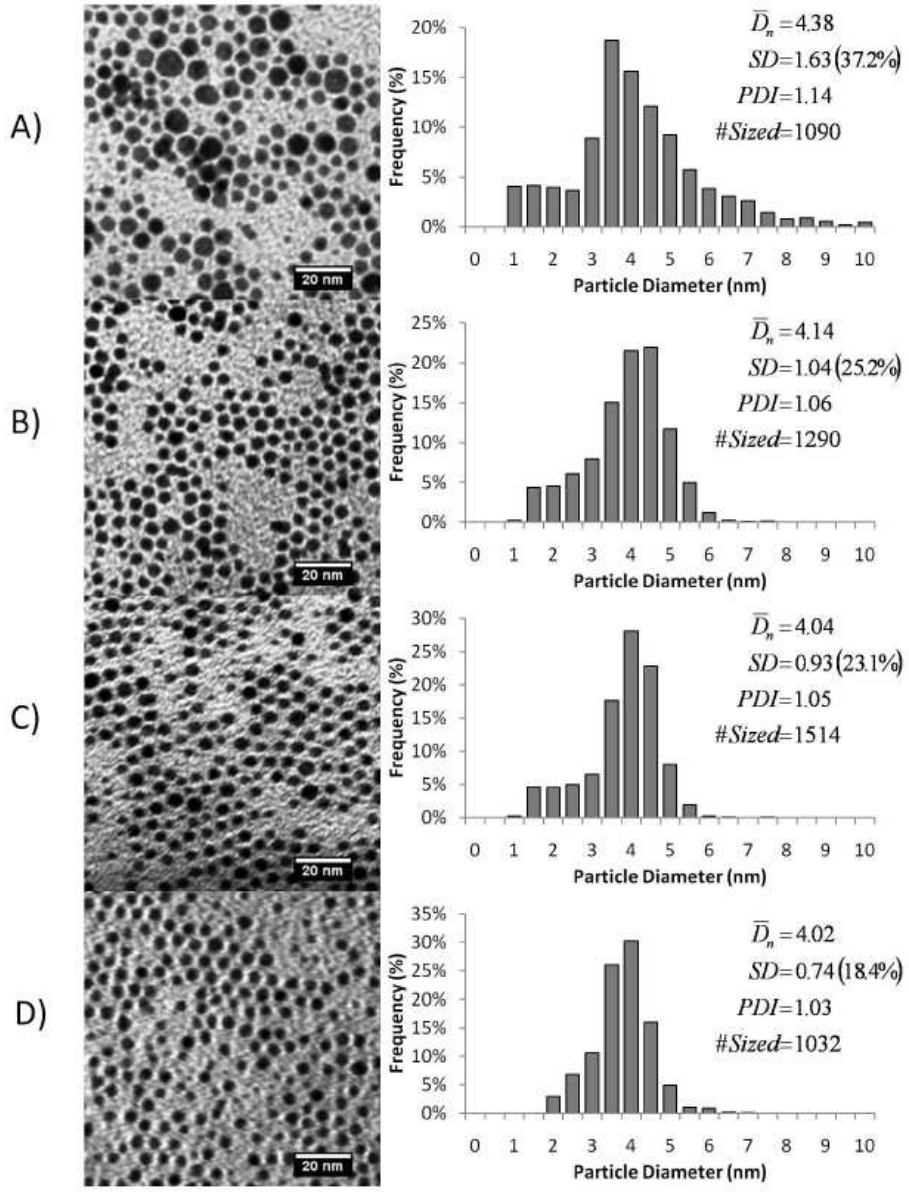

Figure 2.4: TEM micrographs and size distributions of a recursive fractionation of silver nanoparticles. (A) Original sample, (B) one pass, (C) two passes, and (D) three passes. Presented fractions collected between 43 - 45 bar. Scale bars are 20 nm.

an improvement over liquid-based solvent-antisolvent fractionation capable of reaching only 30% (Murray *et al.*, 2000).

2.4 Conclusion

Utilizing the pressure-tunable physico-chemical properties of gas-expanded liquids, application-scale quantities of nanoparticles can be size-selectively fractionated quickly, easily, precisely, without the use of expensive, specialized equipment and without producing large quantities of waste solvent. 1-Dodecanethiol-stabilized gold and silver nanoparticles can be precipitated by finely tuning the subtle balance between the van der Waals attractive forces and osmotic repulsive forces by simply varying an applied partial pressure of CO_2 above the hexane-nanoparticle dispersion. This technique enables the fractionation of large quantities of polydisperse nanoparticles into very narrow ($< \pm 1$ nm), monodisperse fractions with targeted mean diameters.

Chapter 3

Tuning the Precipitation and Fractionation of Nanoparticles in Gas-eXpanded Liquid Mixtures

3.1 Introduction

Nanoparticle size-selective fractionation is a widely used technique which is capable of narrowing the size-distribution of a nanoparticle dispersion while also targetting a specific size (Murray *et al.*, 2000) to make use of the highly size dependent properties of nanoscale materials (Adair *et al.*, 1998). Various methods have been used to size-selectively fractionate nanoparticles including size-exclusion liquid chromatography (Wilcoxon *et al.*, 1998), high pressure liquid chromatography (Fischer *et al.*, 1989; Jimenez *et al.*, 2003), isoelectric focusing electrophoresis (Arnaud *et al.*, 2005), gel electrophoresis (Hanauer *et al.*, 2007), and diafiltration (Sweeney *et al.*, 2006). The most common method makes use of a solvent-antisolvent interaction in which a ligand stabilized nanoparticle is dispersed in a solvent and an antisolvent is added to destabilize the nanoparticles and induce precipitation (Murray *et al.*, 2000). This method is typically performed using a liquid solvent and a liquid antisolvent. However, this method requires long processing times, produces large amounts of waste, and is only capable of yielding ~30% of the nanoparticles within 5% of the average diameter (Murray *et al.*, 2000; Murray *et al.*, 2002). A similar method making use of a liquid solvent and a gaseous antisolvent to create a gas-expanded liquid (GXL) has been developed (Anand *et al.*, 2005; McLeod *et al.*, 2005b; Saunders & Roberts, 2009) to aleviate some of the drawbacks of a liquid-liquid solvent-antisolvent fractionation. While this GXL fractionation method produces extremely high quality nanoparticle fractions it is necessary to subject the nanoparticle dispersion to significant levels of applied CO_2 pressure to induce nanoparticle precipitation. The goal of this work

is to demonstrate that the pressure required to induce nanoparticle precipitation can be reduced by varying the composition of the liquid solvent and by changing the length of the nanoparticle stabilizing ligand.

Gas-expanded liquids are mixtures of an organic solvent (e.g., n-hexane) and a pressurized gas (e.g., CO_2) in which the gas partitions (dissolves) into the liquid organic at applied gas pressures lower than the vapor pressure of the gas (Eckert *et al.*, 2000; Jessop & Subramaniam, 2007). As the applied gas pressure increases, the solubility of the gas in the liquid solvent also increases, thereby allowing significant amounts of the dissolved gas species to be present in the liquid mixture. This change in composition can significantly alter the physico-chemical properties (e.g., density, viscosity, diffusivities, surface tension, etc.) of the resultant liquid mixture by simply adjusting the applied pressure of the gas. An additional advantage of using these systems involves the recovery and recycle of both the liquid solvent and the gas through simple depressurization thus producing no waste.

In Chapter 2 and previous studies (Anand *et al.*, 2005; McLeod *et al.*, 2005b; Anand *et al.*, 2007; Saunders & Roberts, 2009) CO_2 was used as an antisolvent to precipitate alkanethiol-stabilized gold or silver nanoparticles or tri-n-octylphosphine-stabilized CdSe/ZnS nanoparticles from an alkane solvent. The addition of CO_2 to the nanoparticle dispersion weakens the overall solvent strength of the system to the point that the solvation of the stabilizing ligands is no longer able to maintain a stable dispersion of the nanoparticles in the solvent mixture and the nanoparticles begin to precipitate. This precipitation is caused by the inherent van der Waals attractive force between nanoparticles overcoming the weakened repulsive forces provided by the solvation of the ligand tails due to the addition of an antisolvent (Anand *et al.*, 2008; Saunders & Roberts, 2011). The nanoparticles that exhibit the largest van der Waals forces (i.e., the largest nanoparticles) will precipitate first upon worsening solvent conditions. Applied CO_2 pressures beyond 35 bar are required to precipitate 1-dodecanethiol stabilized nanoparticles from a neat n-hexane dispersion (McLeod *et al.*, 2005b).

Methods of reducing the pressure necessary to induce nanoparticle precipitation would reduce equipment costs, provide an opportunity to create higher quality nanoparticle fractions, as well as give new modeling insights into the GXL precipitation phenomenon. One method of accomplishing this is to "seed" a stable liquid nanoparticle dispersion with a poorer secondary liquid solvent such that the overall solvent strength of the liquid mixture is reduced creating a less stable nanoparticle dispersion. For example, a dispersion of nanoparticles in n-hexane could be seeded with enough acetone or ethanol (poor solvents for the alkanethiol ligands) to bring the nanoparticles to the verge of precipitation while remaining stabilized. When this dispersion mixture is pressurized with CO_2, the pressure required to completely destabilize the nanoparticles should be significantly reduced compared to a dispersion in neat n-hexane. Another method of reducing the pressure necessary to induce nanoparticle precipitation would be to use a shorter stabilizing ligand. Anand *et al.* demonstrated (Anand *et al.*, 2005) that shorter ligands provide a weaker repulsive force and require lower applied pressures of CO_2 to induce nanoparticle precipitation and therefore should afford further opportunities for affecting the conditions required for nanoparticle fractionation to be performed. It is necessary to quantify and compare these different precipitation strategies and investigate the effect they have on the quality of the size-selective fractionation using the GXL fractionation technique.

3.2 Experimental

Carbon dioxide (SFC/SFE grade) was obtained from Airgas. Gold (III) chloride trihydrate ($HAuCl_4 \cdot 3H_2O$, ≥99.9+%), sodium borohydride ($NaBH_4$, >98.0%), tetraoctylammonium bromide (TOABr, $[CH_3(CH_2)_7]_4NBr$, 98%), 1-dodecanethiol (DDT, $CH_3(CH_2)_{11}SH$, 98+%), 1-octanethiol (OT, $CH_3(CH_2)_7SH$, 98.5+%), and 1-hexanethiol (HT, $CH_3(CH_2)_5SH$, 95%) were obtained from Aldrich. n-Hexane (HPLC grade, 95%) was obtained from Alfa-Aesar. Acetone (99.9%) was obtained from BDH. Toluene (HPLC grade, 99.9%) and water

(DIUF) were obtained from Fisher. Ethanol (94.0-96.0%) was obtained from Mallinckrodt Chemicals. All chemicals were used as obtained without further purification.

3.2.1 Gold Nanoparticle Synthesis

Alkanethiol-stabilized gold nanoparticles were synthesized via the two-phase arrested precipitation method (Brust *et al.*, 1994; Sigman *et al.*, 2004). This method produces nanoparticles ranging in diameter from 2 to 12 nm with a broad size distribution. A typical gold nanoparticle synthesis is as follows: a solution of 0.36 g of $HAuCl_4 \cdot 3H_2O$ in 36 mL of H_2O was mixed with an organic solution consisting of 2.70 g of the phase-transfer catalyst TOABr in 24.5 mL of toluene. This mixture was vigorously stirred for one hour or until the aqueous phase was clear which was then removed and discarded. A freshly prepared solution of 0.50 g of $NaBH_4$ in 30 mL of H_2O was added as a reducing agent and allowed to stir for 8 h. The aqueous phase was then discarded and 1.00 mmol of the thiol was added and stirred for 4 hours. A large excess of ethanol was added to the organic dispersion of thiol-stabilized nanoparticles as an antisolvent to wash the nanoparticles. The nanoparticles in the solvent/antisolvent mixture was centrifuged (Labnet Hermle Z200A) at 4500 rpm for 5 min to precipitate the nanoparticles. The supernatant, containing the phase-transfer catalyst and the unbound thiol, was discarded. This washing was repeated three times to ensure the nanoparticles were thoroughly cleaned. No liquid solvent-antisolvent size-selective fractionation was performed at this stage, only cleaning. The nanoparticles were then redispersed in n-hexane. The n-hexane dispersions of gold nanoparticles were used for all experiments.

3.2.2 Monitoring Nanoparticle Precipitation

The conditions at which gold nanoparticle precipitation occurs can be easily monitored experimentally by tracking the intensity of the surface plasmon resonance band (SPRB) via UV-vis absorbance spectroscopy (Liu *et al.*, 2007; Schasfoort & Tudos, 2008). Measurement

of the intensity of the SPRB using varying amounts of the antisolvent allows for the precipitation process to be monitored where greater absorbance intensity corresponds to greater nanoparticle dispersability (Anand *et al.*, 2005; McLeod *et al.*, 2005b). Measurement of the intensity of the SPRB is performed slightly differently depending on the antisolvent employed. Precipitations performed using a liquid antisolvent (e.g., ethanol or acetone) must make use of a centrifuge to assist precipitation whereas a GXL precipitation performed with CO_2 is rapid enough to not require centrifugation and can therefore be monitored *in situ*. As a note, the SPRB intensity acquired from the following procedures is normalized to unity under fully dispersed conditions and set to zero under fully precipitated conditions such that fair comparisons can be made between systems.

Liquid-Liquid Precipitation

An aliquot of the nanoparticle dispersion was dried under nitrogen. The dried nanoparticles were then redispersed in a mixture of n-hexane and an antisolvent (e.g., ethanol or acetone). The dispersed nanoparticles were centrifuged at 4500 rpm for 10 minutes to induce nanoparticle precipitation. The supernatant, containing the still dispersed nanparticles, was collected and dried with nitrogen to remove the solvent mixture. The nanoparticles were redispersed in neat n-hexane. The intensity of the SPRB was measured by UV-vis absorbance sprectroscopy. The process was repeated for a different ratio of n-hexane and the selected antisolvent, using equal volumes of the original aliquot, solvent mixture, and neat n-hexane to maintain a fair comparison between solvent ratios.

GXL Precipitation

In order to monitor nanoparticle precipitiation induced via the addition of CO_2, a high pressure vessel specifically designed for UV-vis spectroscopy measurements is used (Anand *et al.*, 2005; McLeod *et al.*, 2005b). The stainless-steel high pressure vessel is

fitted with transparent windows and can be placed into a UV-vis spectrophotometer. A quartz cuvette that contains the liquid nanoparticle dispersion is placed inside the high pressure vessel inline with the viewing windows. This allows for the measurement of the UV-vis spectrum of the nanoparticle dispersion during pressurization of the vessel with applied CO_2 and the subsequent expansion of the liquid mixture within the cuvette. CO_2 is introduced into the vessel from a high pressure syringe pump (ISCO 260D). Applied CO_2 pressure is measured using a simple pressure gauge attached to the vessel.

To precipitate alkanethiol-stabilized nanoparticles, an aliquot of the nanoparticle dispersion was loaded into the cuvette within the high pressure vessel and the vessel was then sealed and purged of any nitrogen and oxygen. CO_2 was used to pressurize the system to a sub-vapor pressure level in order to destabilize and precipitate a portion of the nanoparticles. The UV-vis spectrum was measured once the system reached equilibrium (determined by stabilization of the UV-vis spectrum). The pressure was then increased to a higher applied CO_2 pressure, and the UV-vis spectrum was measured again. This process was repeated until the SPRB vanished. In order to account for the decrease in intensity of the SPRB due to dilution of the nanoparticle dispersion with CO_2, the data is corrected knowing the volume change from either experimental measurements or VLE predictions using the Peng-Robinson equation of state.

As an example, the experimentally measured intensity of the SPRB for the precipitation of 1-dodecanethiol stabilized nanoparticles from n-hexane is presented in Figure 3.1A (◆) as a function of applied CO_2 pressure. The intensity of the SPRB remains constant (i.e., all nanoparticles remain dispersed) until an applied CO_2 pressure of 35 bar is reached beyond which a monotonic decrease in the absorption intensity is observed with further applied CO_2 pressure. The increased CO_2 pressure induces progressive precipitation of the nanoparticles such that the largest nanoparticles precipitate first upon worsening solvent conditions, correspondingly reducing the absorption intensity of the still dispersed nanoparticles.

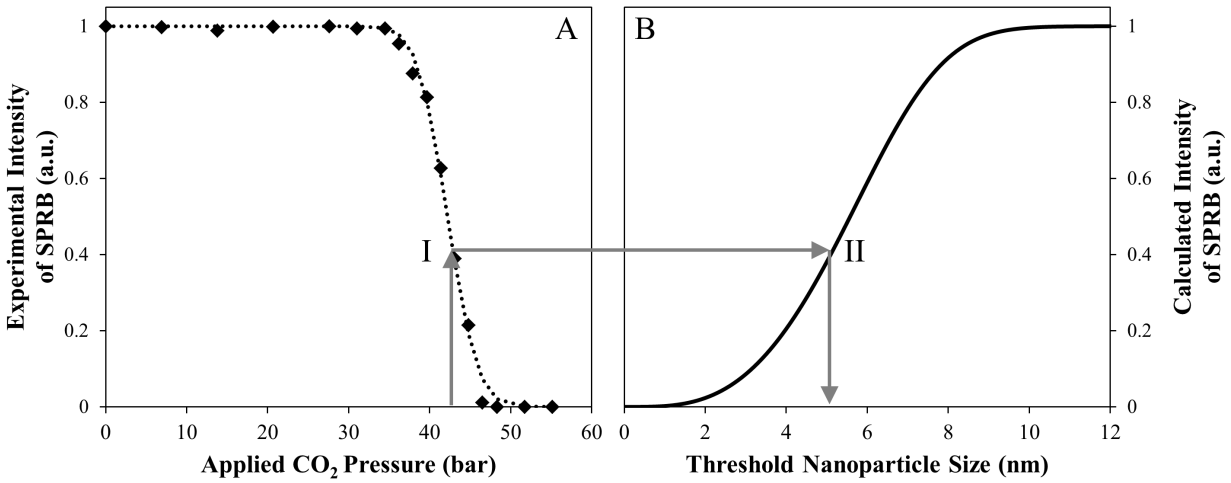

Figure 3.1: Intensity of the surface plasmon resonance band as 1-dodecanethiol stabilized gold nanoparticles precipitate. (A) Experimental intensity (◆) as as function of applied CO_2 pressure. (B) Calculated intensity due to the contributions from nanoparticles smaller than a given threshold nanoparticle size. Gray arrows demonstrate how the nanoparticle threshold size can be determined from the applied CO_2 pressures.

3.2.3 Size-Selective Fractionation

The GXL size-selective fractionation was performed as discussed in Chapter 2 and reported elsewhere (Saunders & Roberts, 2009). The size-selective fractionation apparatus consists of three high pressure vessels (vertically mounted in series) separated by valves such that each vessel can be isolated from each other. CO_2 can be delivered independently to each vessel from a high pressure pump. The applied CO_2 pressure is monitored using a pressure transducer attached to the high pressure vessels. A sample of the nanoparticle dispersion was loaded into the top vessel and the apparatus sealed and purged of any nitrogen and oxygen. All three vessels were pressurized with CO_2 to a sub-vapor pressure level (P_1) such that only a portion of the nanoparticles precipitate from the dispersion (Fraction 1). This portion of nanoparticles would be the largest nanoparticles and would precipitate onto the walls of the high pressure vessel. Then, while maintaining constant pressure throughout the system, the still dispersed smaller nanoparticles were drained (away from the precipitated larger nanoparticles) via gravity into the second high pressure vessel. The system was then pressurized with CO_2 to a higher pressure (P_2) but still below the vapor pressure of CO_2. As such, the next largest portion of nanoparticles precipitated onto the walls of the second high pressure vessel (Fraction 2). Again, while maintaining constant pressure throughout the apparatus, the still dispersed smallest nanoparticles were drained (away from the precipitated Fraction 2) via gravity into the third high pressure vessel. The system was subsequently slowly depressurized. The liquid containing the smallest nanoparticles was collected (Fraction 3). The precipitated fractions in the first and second vessel were collected by simply washing each vessel with n-hexane.

Carbon-coated TEM grids were then prepared via drop-casting and micrographs were acquired on a Zeiss EM 10 Transmission Electron Microscope and sized using the ImageJ software package. The polydispersity index (PDI) is a measure of the broadness of the size distribution which can be used to compare size distributions with varying average

diameters. A PDI of 1 indicates that all of the nanoparticles present are the same exact size and the larger the value of the PDI the more broad the distribution. The PDI is calculated as reported elsewhere (Saunders & Roberts, 2009).

3.3 Predicting the Sizes of Recovered Fractions

The ability to predict the average diameters of the nanoparticles obtained in each of the recovered fractions as a function of the applied CO_2 pressures would drastically ease experimentation. It is possible to equate the intensity of the SPRB found experimentally to a calculated intensity based on the size of nanoparticles that would remain dispersed at a given set of conditions. This calculated intensity is found by assuming that nanoparticles up to a specific threshold size are capable of being dispersed at a given set of conditions by accounting for the cumulative contributions of the differently sized nanoparticles that remain dispersed. As the experimental intensity of the SPRB is normalized (as described above), special care is given to maintaining the normalization throughout the following derivation.

It is important to have an accurate mathematical representation of a distribution of nanoparticles to be experimentally fractionated. For the purposes of this study, all distributions will be modeled as normally distributed.

$$PDF\,(D) = \frac{1}{\sqrt{2\pi\sigma^2}} e^{-\left(D-\mu\right)^2/2\sigma^2} \tag{3.1}$$

where D represents the diameter, and μ and σ are the average diameter and standard deviation, respectively, of the original nanoparticle distribution found experimentally. It should be noted that the distribution choice (normal vs. lognormal vs. etc.) should be made as to ensure the best agreement between the model and experimental observations. As a probability distribution function (*PDF*) represents the probability that a specific sized nanoparticle exists, it is important to scale the *PDF* to represent the number of gold atoms

(rather than individual nanoparticles) since the intensity of the SPRB would depend on the concentration of gold atoms (i.e., mass). It is easy to calculate the number of gold atoms (N_{Au}) that would exist in a specific sized nanoparticle based on the volume of that nanoparticle.

$$N_{Au}(D) = \frac{\pi \rho N_A}{6M} D^3 \tag{3.2}$$

where ρ is the density of bulk gold, N_A is Avogadro's number, and M is the molecular weight of gold. Multiplying Equation 3.1 and Equation 3.2 would lead to a probability distribution function that is in terms of the frequency of the number of gold atoms rather than the frequency of the number of the nanoparticles. Integrating this probability distribution function and restricting the intergration bounds would lead to an approximate concentration (C) of gold atoms in the sample. The restriction placed on the bounds of the integral are placed such that only the nanoparticle sizes that would be dispersed are included in the calculation so as to mirror what is seen experimentally (i.e., nanoparticles up to a specific sized can be dispersed at a given set of conditions).

$$C(D_T) \cong \frac{1}{c} \int_0^{D_T} N_{Au}(w) \frac{PDF(w)}{\int_0^{D_T} PDF(z)\, dz} dw \tag{3.3}$$

where D_T is the largest sized nanoparticle that can be dispersed (the "threshold nanoparticle size"), and c is a normalization constant calculated by including all possible sizes of nanoparticles in the calculation ($\lim_{D_T \to \infty}$). The denominator maintains the normalization constraint for a probability distribution function (as larger nanoparticles are removed from the calculation as they are precipitated, the normalization of the probability distribution must change). The concentration can be related to the intensity of the SPRB (A, absorbance) through the Beer-Lambert Law.

$$A(D_T) = C(D_T)\, l \epsilon \tag{3.4}$$

where l would be the path length of light through the sample, and ϵ would be the extinction coefficient of the sample. However, the extinction coefficient varies with respect to the solvent conditions and the size of the nanoparticles (Liu *et al.*, 2007), thus forcing the need to assume a value for ϵ. To retain the normalization necessary for a comparison to the experimental data, ϵ and l are assumed to be constant and equal to one leading to $A(D_T) = C(D_T)$.

This calculated intensity of the SPRB is presented in Figure 3.1B as a function of the threshold nanoparticle size and can easily be compared to the experimental intensity of the SPRB. As CO_2 is added to a stable dispersion (i.e., traversing along the data in Figure 3.1A from left to right) the intensity of the SPRB decreases due to the largest nanoparticles being destabilized and precipitating corresponding to a concomitant decrease in the calculated intensity of the SPRB as a function of the decreasing threshold nanoparticle size (i.e., traversing along the curve in Figure 3.1B from right to left). Therefore the experimental intensity of the SPRB at any given applied CO_2 pressure (point I in Figure 3.1) can be equated to a calculated intensity (point II in Figure 3.1) describing the largest sized nanoparticle that can be dispersed at a given set of conditions . It is assumed that nanoparticles smaller than the threshold nanoparticle size remain dispersed while nanoparticles larger than the threshold nanoparticle size precipitate from the dispersion. Knowing the original distribution, it is possible to calculate the average diameter of the precipitated nanoparticles using standard statistical methods.

$$\overline{D}_i = CDF^{-1}\left[\frac{CDF(D_{Ti-1}) + CDF(D_{Ti})}{2}\right] \tag{3.5}$$

where the CDF is the cumulative distribution function and CDF^{-1} is the inverse cumulative distribution function.

This methodology can be extended to mirror the fractionation process. At a given applied pressure of CO_2 (P_1) a portion of the nanoparticles are precipitated, and a

corresponding threshold nanoparticle size can be calculated (D_{T1}) using the methodology described above. Hence, the average size ($\overline{D}_1$) of this precipitated fraction (Fraction 1) can be determined knowing the statistical distribution of the original nanoparticle dispersion. A second portion (Fraction 2) of nanoparticles (of smaller average size) can then be precipitated at a second applied pressure of CO_2 (P_2) and its corresponding threshold nanoparticle size can be calculated (D_{T2}) along with its average size ($\overline{D}_2$). Given the assumption that all nanoparticles smaller than the threshold nanoparticle size remain dispersed while all nanoparticles larger than the threshold nanoparticle size precipitate, Fraction 2 would consist of the nanoparticles larger than D_{T2} but smaller than D_{T1}. The average diameter for Fraction 3 ($\overline{D}_3$) would be calculated as the nanoparticles smaller than D_{T2} from the original dispersion since those nanoparticles could not be precipitated at the solvent conditions created at an applied CO_2 pressure of P_2.

In order to demonstrate the accuracy of this method, an experimental size-selective fractionation of DDT-stabilized gold nanoparticles dispersed in n-hexane was performed with P_1 = 43.1 bar and P_2 = 43.8 bar. A summary of the average diameters found experimentally and calculated is presented in Table 3.1. Average diameters were calculated as described above and are well within 5% of the experimental findings. In practice, this method is used in the reverse order (i.e., the average sizes of the fractions are defined and the applied CO_2 pressures calculated). This method is used throughout the rest of this study in order to determine the experimental fractionation pressures that should be employed when switching solvent media and stabilizing ligands.

3.4 Results

A precipitation and fractionation of DDT-stabilized gold nanoparticles dispersed in n-hexane is used as the control for comparison with experiments performed using other solvent mixtures and stabilizing ligands. The precipitation of the DDT-stabilized nanoparticles from neat n-hexane using CO_2 as the antisolvent was monitored, as

Fractionation Pressure (Bar)	Experimental Average Diameter (nm)	Calculated Average Diameter (nm)	Error (%)
0 - 43.1	5.86	5.82	0.68
43.1 - 43.8	4.87	4.91	0.82
43.8+	3.97	3.87	2.52

Table 3.1: Comparison between experimental average diameters and calculated average diameters for a size-selective fractionation of 1-dodecanethiol stabilized gold nanoparticles dispersed in n-hexane.

described above, and the data presented in Figure 3.1 (◆). The fractionation of the DDT-stabilized nanoparticles from neat n-hexane using CO_2 was performed (experiment #1), as described above, with P_1 = 43.1 and P_2 = 43.8 bar. This fractionation took approximately 2 hours to complete: approximately 50 minutes for Fraction 1, 50 minutes for Fraction 2, and 20 minutes to depressurize and collect the fractions. TEM micrographs and size-distributions of the original sample and recovered fractions are presented in Figure 3.2 and the statistical summary presented in Table 3.2. This represents a typical result for the fractionation of DDT-stabilized gold nanoparticles dispersed in neat n-hexane.

In order to precipitate the nanoparticles at lower applied CO_2 pressures, a secondary antisolvent (e.g., ethanol or acetone) was added to the n-hexane nanoparticle dispersion prior to initial pressurization with CO_2. The goal was to add a quantity of the secondary antisolvent in order to lower the overall solvent strength of the solvent mixture (e.g., n-hexane + acetone) to the point where the nanoparticles are on the verge of precipitation. Figure 3.3 presents the nanoparticle precipitation of DDT-stabilized gold nanoparticles dispersed in n-hexane when using ethanol or acetone as the only antisolvent as indicated by the change in intensity of the SPRB. It was determined that the nanoparticle dispersion could be thermodynamically stabilized in a mixture consisting of 55 mol% n-hexane and 45% acetone or in a mixture consisting of 60% n-hexane and 40% ethanol. This indicates that ethanol is a slightly more effective antisolvent than acetone. By reducing the overall solvent strenght of the solvent media prior to CO_2 pressurization, the addition of the secondary solvent should have a signficant impact on the GXL precipitation process by lowering the applied CO_2 pressure required to induce precipitation.

Figure 3.4 presents the CO_2-induced precipitation of DDT-stabilized gold nanoparticles dispersed in neat n-hexane (◆), in a mixture of n-hexane and acetone (55/45 mol%, ▲), and in a mixture of n-hexane and ethanol (60/40 mol%, ■). Nanoparticles that were dispersed in the mixture of n-hexane and acetone precipitated at an applied CO_2 pressure that is approximately 43% lower than that necessary for nanoparticle

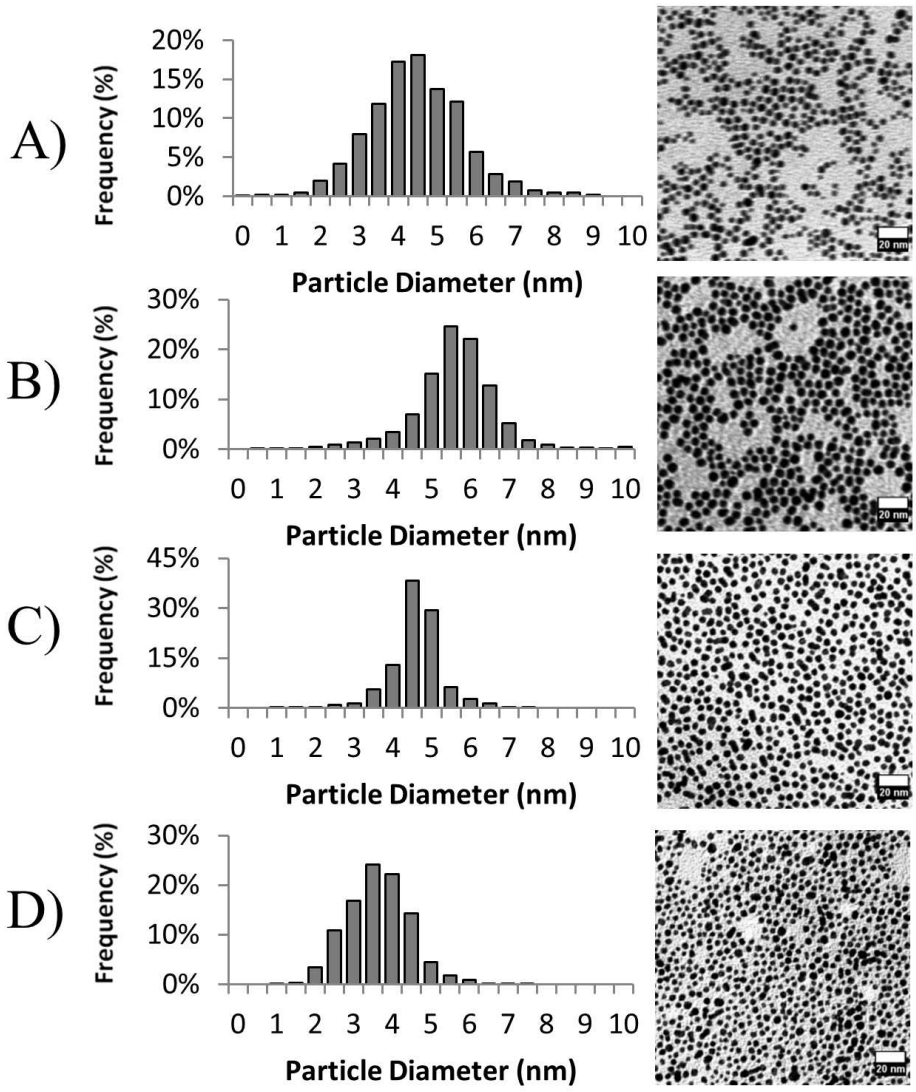

Figure 3.2: Size distributions and TEM micrographs of a size-selective fractionation of DDT stabilized gold nanoparticles dispersed in neat n-hexane. (A) Original sample, (B) nanoparticles precipitated between applied CO_2 pressures of 0 - 43.1 bar, (C) nanoparticles precipitated between applied CO_2 pressures of 43.1 - 43.8 bar, and (D) nanoparticles collected that were not precipitated at an applied CO_2 pressure of 43.8 bar. Scale bars are 20 nm.

Experiment			Fractionation Pressure	Mean Diameter	Standard Deviation	PDI
#	Ligand	Solvent	(Bar)	(nm)	(nm)	
1	DDT	n-Hexane	Original	4.70	1.20	1.068
			0 - 43.1	5.86	1.11	1.036
			43.1 - 43.8	4.87	0.66	1.018
			43.8+	3.97	1.83	1.045
2	DDT	n-Hexane/ Acetone (55/45 mol%)	Original	5.24	1.22	1.056
			0 - 36.1	5.63	0.61	1.011
			36.1 - 37.6	4.97	0.66	1.011
			37.6+	3.57	0.71	1.039
3	HT	n-Hexane	Original	3.88	1.44	1.138
			0 - 32.8	5.04	1.76	1.027
			32.8 - 37.9	3.83	0.97	1.055
			37.9+	3.02	0.75	1.062
4	HT	n-Hexane/ Acetone (55/45 mol%)	Original	3.88	1.44	1.138
			0 - 20.7	4.26	1.11	1.081
			20.7 - 27.7	4.12	1.45	1.120
			27.7+	2.80	0.94	1.106

Table 3.2: Statistical summary of single pass fractionations of gold nanoparticles. (1) Control, ligand: 1-dodecanethiol, solvent: neat n-hexane, (2) ligand: 1-dodecanethiol, solvent: mixture of n-hexane and acetone (55/45 mol%), (3) ligand: 1-hexanethiol, solvent: neat n-hexane, and (4) ligand: 1-hexanethiol, solvent: mixture of n-hexane and acetone (55/45 mol%).

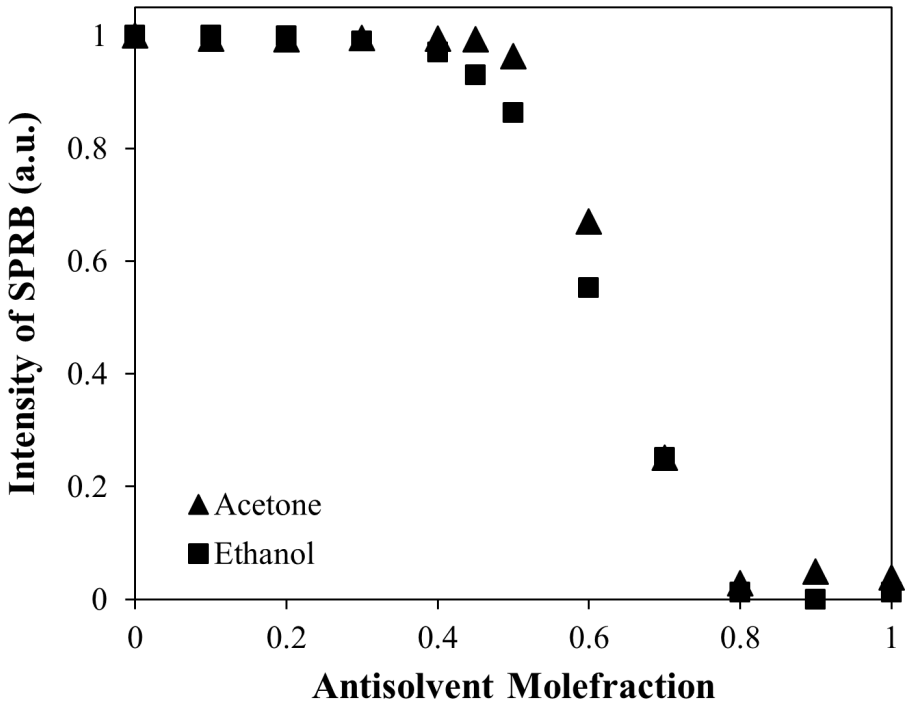

Figure 3.3: The intensity of the SPRB of DDT-stabilized gold nanoparticles that remain dispersed after precipitation from mixtures of n-hexane and (▲) acetone or (■) ethanol.

precipitation from neat n-hexane. This implies that the onset of nanoparticle precipitiation can be tuned between applied CO_2 pressures of approximately 35 bar and 20 bar by simply varying the amount of acetone present in the solvent mixture prior to precipitation. Nanoparticles that were dispersed in the mixture of n-hexane and ethanol precipitated at an applied CO_2 pressure that is approximately 10% greater than that that necessary for nanoparticle precipitation from neat n-hexane. While this might appear counter-intuitive, this is likely due to the fact that CO_2 is significantly less soluble in ethanol than in alkanes or acetone (Houndonougbo *et al.*, 2006). Therefore, a higher applied CO_2 pressure must be applied to induce nanoparticle precipitation using ethanol as the secondary solvent. As such, it is not beneficial to use ethanol as a secondary solvent and will not be further investigated in this study.

The 1-dodecanethiol stabilized gold nanoparticles dispersed in the mixture of n-hexane and acetone (55/45 mol%, respectively) were size-selectively fractionationed (experiment #2) with P_1 = 36.1 and P_2 = 37.6 bar (these pressures were calculated using the method described above in an effort to obtain similarly sized fractions as in experiment #1). This fractionation took approximately 3 hours to complete: approximately 80 minutes for Fraction 1, 80 minutes for Fraction 2, and 20 minutes to depressurize and collect the fractions (additional processing time was required for this precipitation as the solvent media was more liquid-like at the lower operating pressures). TEM micrographs and size-distributions of the original sample and recovered fractions are presented in Figure 3.5 and the statistical summary presented in Table 3.2. All three recovered fractions from this mixed solvent fractionation can be considered monodisperse based on their standard deviation whereas the fractionation performed in neat n-hexane produced only one monodisperse fraction (those nanoparticles precipitated between applied CO_2 pressure of 43.1 - 43.8 bar). This is obvious from the statistical summary but also evident based on the degree of hexagonal packing present in the TEM micrographs in Figure 3.5. The second fraction in both cases are almost identical with regard to the the average diameter

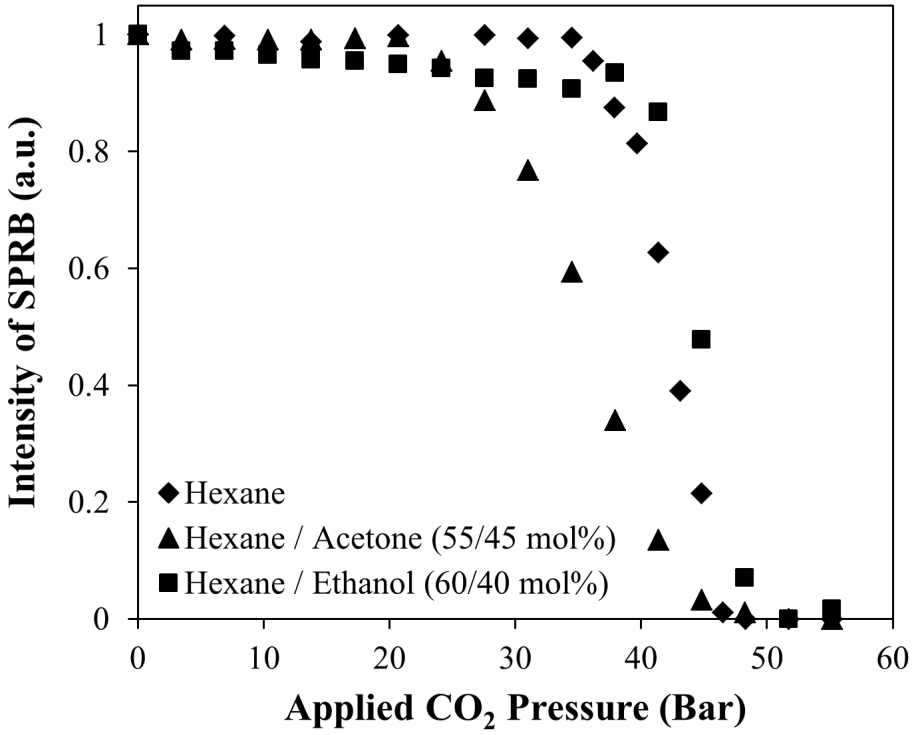

Figure 3.4: Intensity of the SPRB of dispersed DDT-stabilized gold nanoparticles at varying levels of applied CO_2 pressure when initially dispersed in (◆) neat n-hexane, (▲) a mixture of n-hexane and acetone (55/45 mol%), or (■) a mixture of n-hexane and ethanol (60/40 mol%).

and standard deviation even though the nanoparticles that were precipitated from neat n-hexane were collected within a pressure interval of 0.7 bar whereas the nanoparticles that were precipitated from the mixture were collected within a pressure interval of 1.5 bar. Because the introduction of the acetone reduced the pressure at which the onset of nanoparticle precipitation occurred, the pressure range over which the fractionation process can be performed has increased (i.e., both the onset of precipitation and the slope has been effected). This allowed for greater control over the size distributions of the recovered nanoparticle fractions and produced fractions of a significant higher quality.

Anand *et al.* demonstrated (Anand *et al.*, 2005) that as the length (number of carbons) of the alkanethiol is reduced, the degree to which the ligand can stabilize the nanoparticles in a solvent is reduced. Figure 3.6 presents the precipitation curves for nanoparticles stabilized using three different alkanethiols of varying length illustrating the reduction in applied CO_2 pressure necessary to induce nanoparticle precipitation as the thiol length is shortened. 1-Hexanethiol stabilized gold nanoparticles dispersed in neat n-hexane were size-selectively fractionated (experiment #3) with P_1 = 32.8 and P_2 = 37.9 bar. This fractionation took approximately 3 hours to complete. TEM micrographs and size-distributions of the original sample and recovered fractions are presented in Figure 3.7 and the statistical summary presented in Table 3.2. In this case, the quality of the nanoparticles is signficantly reduced (i.e., some of the nanoparticles are not completely spherical). This fractionation did produce significantly different sized fractions, indicating that obtaining an effective fractionation is possible with HT-stabilized nanoparticles, however, the recovered fractions were smaller with regard to the average size compared to what was predicted. This deviation is due to a thin film of nanoparticles that is formed along the high pressure vessel wall when the dispersed nanoparticles are drained from one vessel to the next. This thin film thereby contaminates the precipitated fraction with a portion of smaller nanoparticles that should have been otherwise carried into the next vessel (Saunders & Roberts, 2011), see 5.

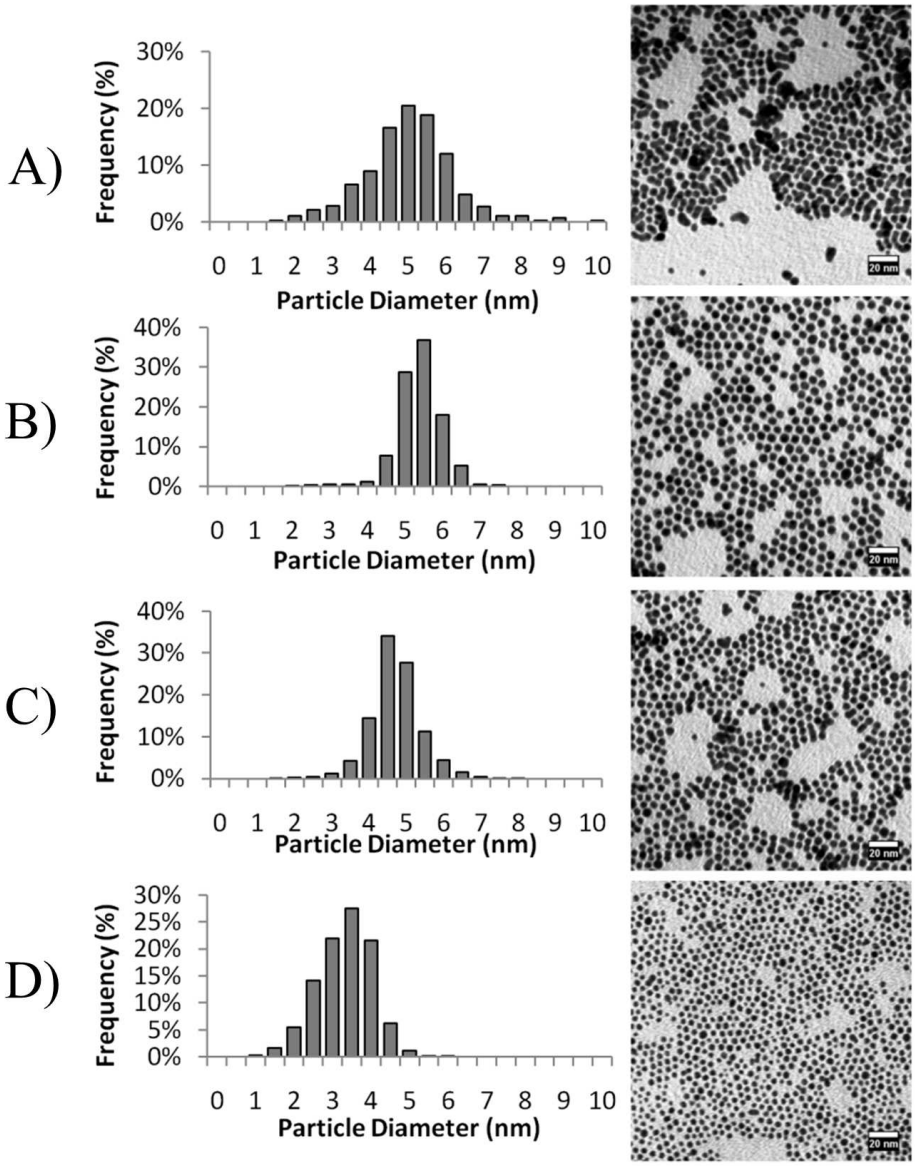

Figure 3.5: Size distributions and TEM micrographs of a size-selective fractionation of 1-dodecanethiol stabilized gold nanoparticles dispersed in a mixture of n-hexane and acetone (55/45 mol%). (A) Original sample, (B) nanoparticles precipitated between applied CO_2 pressures of 0 - 36.1 bar, (C) nanoparticles precipitated between applied CO_2 pressures of 36.1 - 37.6 bar, and (D) nanoparticles collected that were not precipitated at an applied CO_2 pressure of 37.6 bar. Scale bars are 20 nm.

As the dispersed nanoparticles are transferred from one vessel to the next, the liquid/vapor interface traverses the vessel wall depositing nanoparticles in a fashion similar to that of a Langmuir-Blodgett film. Fraction 1 did not contain a high concentration of nanoparticles (i.e., the recovered dispersion was very dilute upon visual inspection), indicating that very few nanoparticles precipitated. Since a small number of nanoparticles were precipitated at these conditions, the recovered fraction consisted of (1) the small number of large nanoparticles that should have precipitated this applied CO_2 pressure and (2) the nanoparticles that were inadvertently deposited during the creation of this thin film upon drainage of the dispersion to the next vessel. The impact of this effect can be seen in the size-distribution histogram for Fraction 1 (Figure 3.7B). The frequency of nanoparticles smaller than 3.5 nm is very similar to that of the original distribution due to this undesired film formation, whereas the frequency of the nanoparticles obtained that were larger than 3.5 nm show a marked increase compared to the original distribution due to the precipitation of the largest nanoparticles. Unfortunately, this phenomenon is not included in the empirical model, thus leading to deviations from the predicted results when small populations of nanoparticles are precipitated at a given set of conditions. This thin film deposition occurs with every fraction but has little impact when the number of nanoparticles precipitated at a given set of conditions is significantly larger than the number of nanoparticles deposited during the thin film formation.

The next set of experiments involved an effort to further reduce the required applied CO_2 pressure to induce precipitation of these HT-stabilized gold nanoparticles. A liquid-liquid precipitation was performed to determine the amount of acetone that could be added while retaining a thermodynamically stabilized dispersion. It was found that a mixture of 55 mol% n-hexane and 45% acetone (the same as that required for 1-dodecanethiol) maintained a stable dispersion of gold nanoparticles. When a dispersion of HT-stabilized gold nanoparticles in a mixture of n-hexane and acetone (55/45 mol%) was pressurized with CO_2, as demonstrated in Figure 3.8, precipitation occurred at an applied

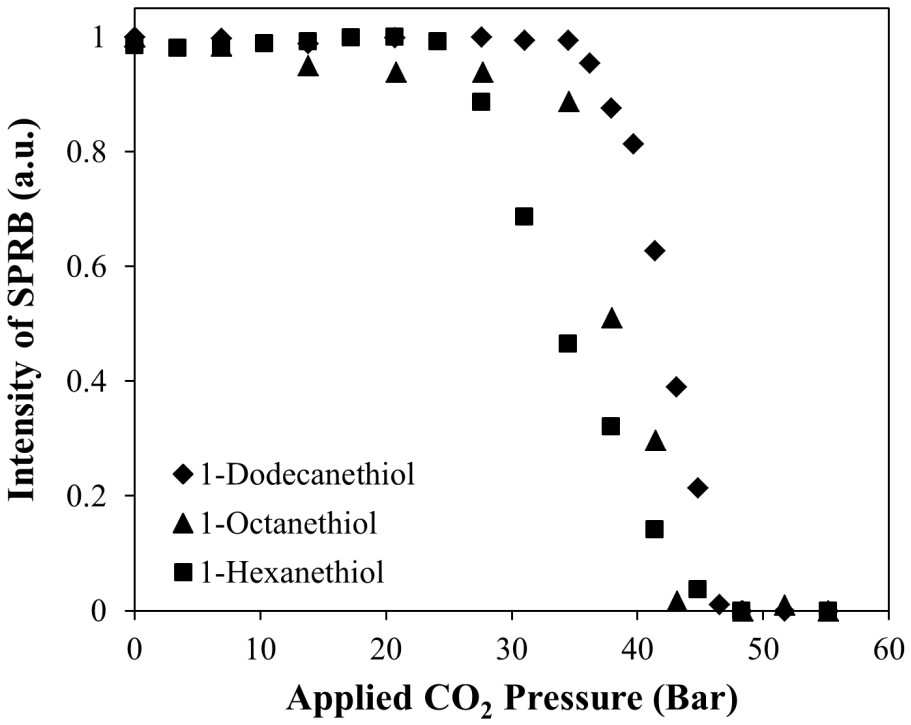

Figure 3.6: Intensity of the SPRB of dispersed gold nanoparticles at varying levels of applied CO_2 pressure initially dispersed in n-hexane when stabilized with (◆) 1-dodecanethiol (this work), (▲) 1-octanethiol (Anand *et al.*, 2005), or (■) 1-hexanethiol (this work).

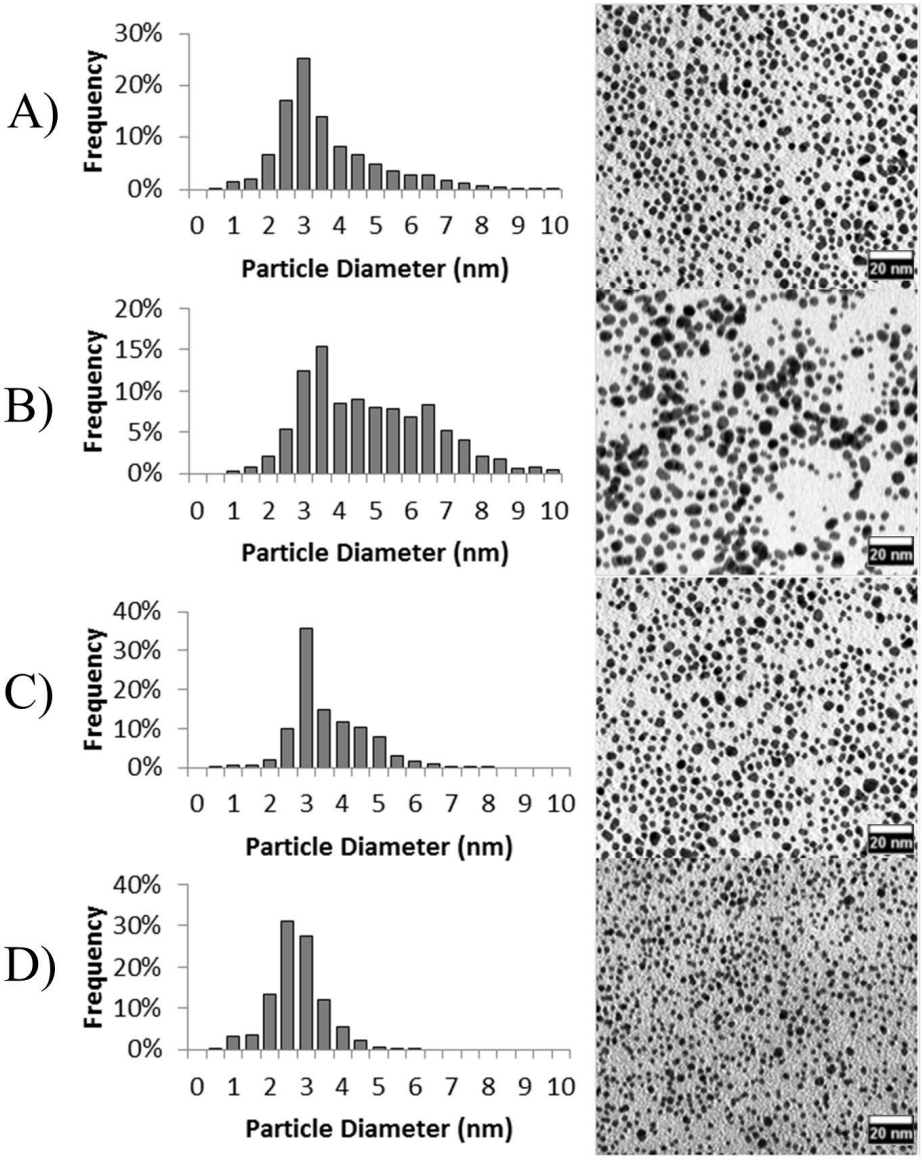

Figure 3.7: Size distributions and TEM micrographs of a size-selective fractionation of 1-hexanethiol stabilized gold nanoparticles dispersed in neat n-hexane. (A) Original sample, (B) nanoparticles precipitated between applied CO_2 pressures of 0 - 32.8 bar, (C) nanoparticles precipitated between applied CO_2 pressures of 32.8 - 37.9 bar, and (D) nanoparticles collected that were not precipitated at an applied CO_2 pressure of 37.9 bar.

CO_2 pressure of only 5 bar. This represents an 85% reduction in the applied CO_2 pressure necessary to induce nanoparticle precipitation compared to 1-dodecanethiol stabilized gold nanoparticles dispersed in neat n-hexane. This implies that the onset of nanoparticle precipitation can be tuned continuously between 35 bar and 5 bar of applied CO_2 pressure by adjusting the solvent media and/or the stabilizing ligand.

1-Hexanethiol stabilized gold nanoparticles dispersed in a mixture of n-hexane and acetone (55/45 mol%, respectively), were size-selectively fractionationed (experiment #4) with $P_1 = 20.7$ and $P_2 = 27.7$ bar. This fractionation took approximately 2 days to complete: approximately 1 day for Fraction 1, 1 day for Fraction 2, and 20 minutes to depressurize and collect fractions. TEM micrographs and size-distributions of the original sample and recovered fractions are presented in Figure 3.9 and the statistical summary presented in Table 3.2. While three differently sized fractions are recovered, the fraction that was predicted to be the most narrow, Fraction 2, was actually the most polydisperse. The results in this case do not match what was predicted by the empirical model due to two extenuating factors: (1) the thin film deposition process (discussed above) and (2) the long processing time. Due to the low operating pressures neccessary to induce nanoparticle precipitation from this solvent mixture, more time is required to allow the nanoparticles to precipitate once destabilized. The lower operating pressures leads to the solvent mixture being more liquid-like than the previous examples, thus having a higher viscosity (Kho *et al.*, 2003) and lower diffusivities through the medium (Hallett *et al.*, 2006; Sassiat *et al.*, 1987). The fluid properties are more similar to the traditional liquid-liquid solvent precipitation process which commonly invokes centrifugation to induce precipitation. This implies there is an embedded tradeoff between the reduction in operating pressure and the resulting increase in the necessary processing time for nanoparticle precipitation.

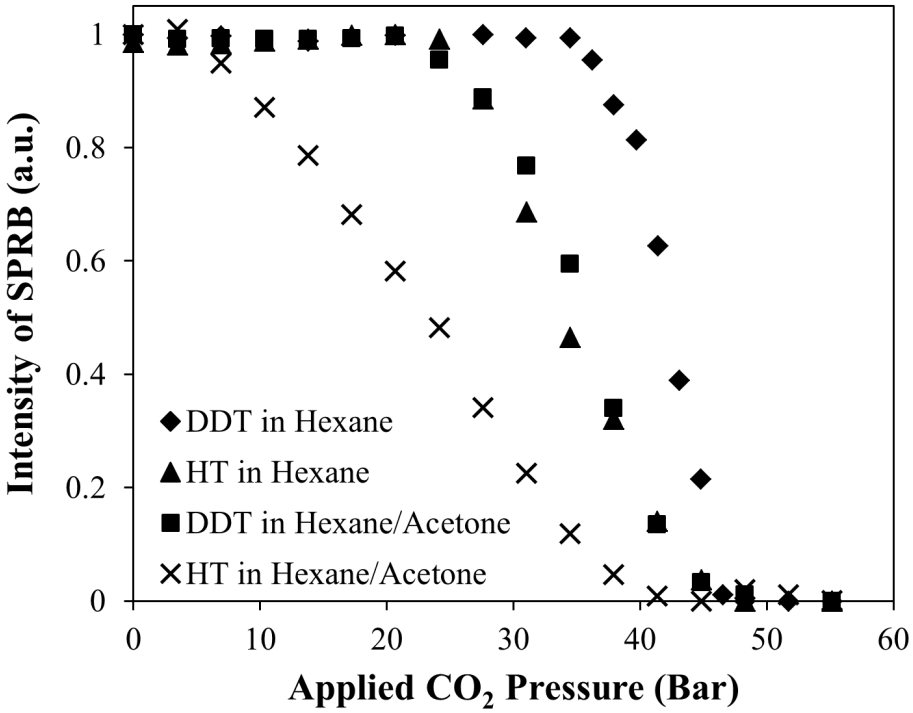

Figure 3.8: Intensity of the SPRB of dispersed gold nanoparticles at varying levels of applied CO_2: (◆) 1-dodecanethiol nanoparticles disperse in neat n-hexane, (▲) 1-hexanethiol nanoparticles dispersed in neat n-hexane, (■) 1-dodecanethiol nanoparticles dispersed in a mixture of n-hexane and acetone (55/45 mol%), and (×) 1-hexanethiol nanoparticles dispersed in a mixture of n-hexane and acetone (55/45 mol%).

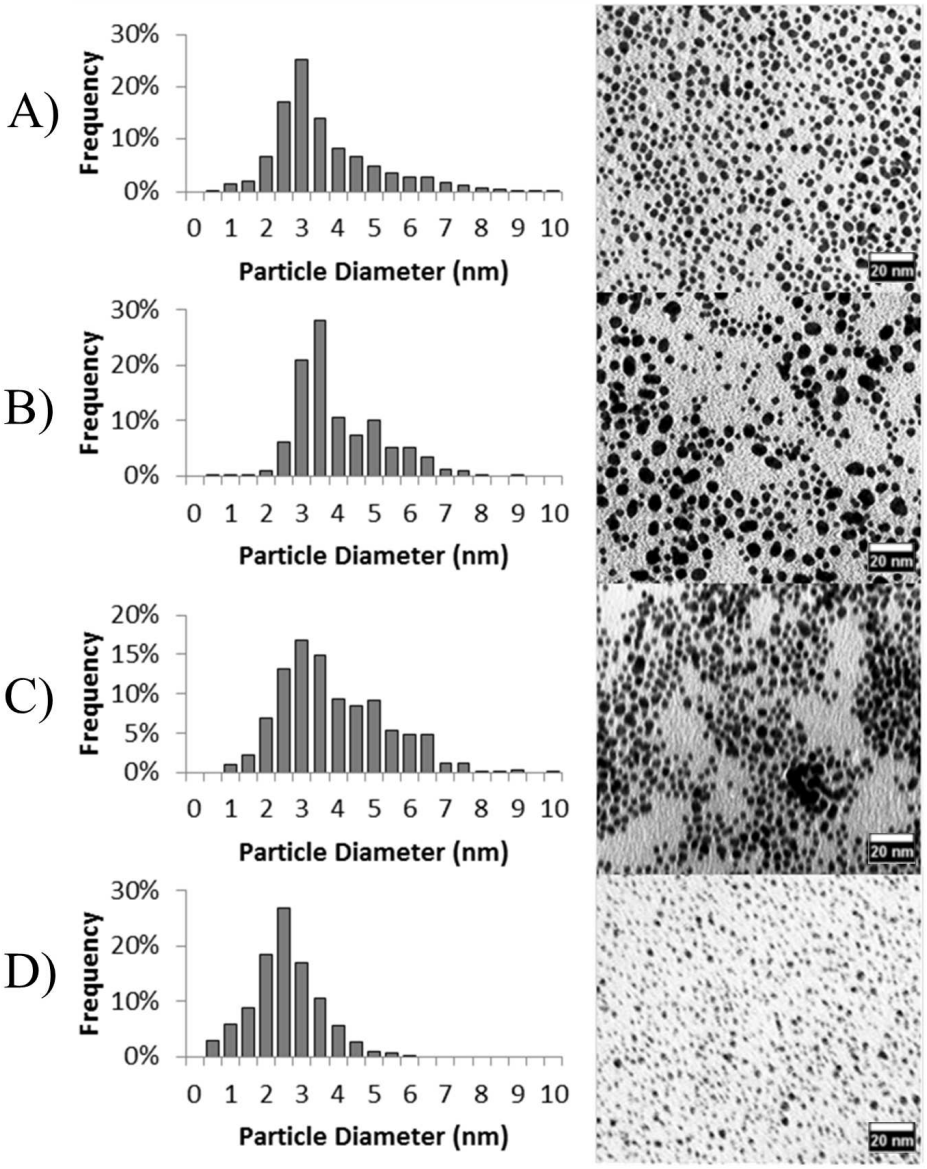

Figure 3.9: Size distributions and TEM micrographs of a size-selective fractionation of 1-hexanethiol stabilized gold nanoparticles dispersed in a mixture of n-hexane and acetone (55/44 mol%). (A) Original sample, (B) nanoparticles precipitated between applied CO_2 pressures of 0 - 20.7 bar, (C) nanoparticles precipitated between applied CO_2 pressures of 20.7 - 27.6 bar, and (D) nanoparticles collected that were not precipitated at an applied CO_2 pressure of 27.6 bar. Scale bars are 20 nm.

3.5 Conclusions

Through simple adjustments in the solvent composition and the stabilizing ligand of alkanethiol-stabilized gold nanoparticles, the CO_2 pressure required to induce nanoparticle precipitation can be tuned continuously from 35 bar (neat n-hexane, 1-dodecanethiol) to 5 bar (mixture of n-hexane, 55 mol%, and acetone, 45%, 1-hexanethiol). This tuning can be used to optimize the quality of the recovered nanoparticle fractions obtained from the size-selective GXL fractionation process. The use of longer alkanethiol stabilizing ligands created high quality initial nanoparticles in terms of sphericity. The use of shorter alkanethiol stabilizing ligands afforded a reduction in the required applied CO_2 pressure to induce nanoparticle precipitation. Of the conditions examined in this study, an optimum exists for 1-dodecanethiol stabilized gold nanoparticles dispersed in a mixture of n-hexane and acetone in which the best fractions (in terms of monodispersity) were obtained. This may not be the "global optimum," as other conditions and other solvent mixtures may be capable of producing even higher quality nanoparticle fractions. It was also demonstrated that a simple empirical model based on experimental UV-vis measurements and a simple size distribution can be used to quickly and accurately estimate the average size of recovered fractions from a GXL fractionation of nanoparticles.

Chapter 4

Thermodynamic Analysis of a Nanoparticle Size-Selective Fractionation Using Gas-eXpanded Liquids

4.1 Introduction

Ongoing research in the past decade has developed methods of nanoparticle synthesis and processing using carbon dioxide (CO_2) Gas-eXpanded Liquids (GXL's) in order to take advantage of their unique properties. GXL's are mixtures of dissolved gas (e.g. CO_2) in an organic solvent compressed to pressures between atmospheric and the pure gas vapor pressure (57.2 bar at 20 °C for CO_2). The main advantage of this solvent system lies in the ability to tune a number of physico-chemical properties (e.g., density, surface tension, viscosity, diffusivity, and solvent strength) with only slight changes in pressure. CO_2 gas-expanded liquids have also garnered a great deal of attention in applications such as tunable solvent separations, gas-antisolvent crystallization, organic and polymer microparticle formation, and chemical reaction tuning. GXL's are tunable solvents with desirable attributes of both pure components, including the high solvent strength of organic solvents as well as the low surface tension and viscosity of gases. In Chapter 2 and 3 previous work (Zhang *et al.*, 2001; McLeod *et al.*, 2005a; Liu *et al.*, 2006), the tunable solvent properties of CO_2 gas-expanded liquids were used to vary the solvent strength of nanoparticle dispersions, resulting in controlled nanoparticle precipitation and uniform-wide-area deposition.

In the previous chapters and studies (Anand *et al.*, 2005; McLeod *et al.*, 2005b; Anand *et al.*, 2007; Saunders & Roberts, 2009), CO_2 was used as an antisolvent in a GXL system to size-selectively precipitate and separate ligand-stabilized metal nanoparticle dispersions into narrow size distributions, relative standard deviation (RSD) ≈10%,

through fine adjustments in CO_2 pressure. Nanoparticle dispersibility in a solvent requires favorable solvent-ligand interaction to provide sufficient repulsive force necessary to overcome the van der Waals forces of attraction between nanoparticles in dispersion. The degree of solvent-ligand interaction is diminished upon the gradual addition of CO_2, a known antisolvent of aliphatic ligands, enabling gradual size-selective precipitation. The magnitude of the van der Waals attractive forces between nanoparticles scales with nanoparticle size and thus the largest nanoparticles precipitate first upon worsening solvent conditions. Therefore, by precisely adjusting the applied CO_2 pressure, the dispersibility of nanoparticles can be controlled to obtained monodisperse nanoparticle fractions.

A theoretical model based on total interaction energy is applied to the size selective fractionation process using the tunable physico-chemical properties of CO_2 GXLs to predict the threshold nanoparticle size (i.e., the maximum nanoparticle size that can be dispersed in the GXL as a function of CO_2 pressure). Theoretically, nanoparticles which are smaller than this maximum (threshold) nanoparticle size will remain dispersed while larger particles will precipitate from solution. Previous studies have predicted the nanoparticle size stabilized at a given set of conditions in conventional liquid solvents (Kitchens *et al.*, 2003), supercritical ethane (Shah *et al.*, 2002b), compressed propane (Kitchens & Roberts, 2004), and supercritical carbon dioxide (Shah *et al.*, 2002a).

4.2 Theory

Shah *et al.* (Shah *et al.*, 2002b) and Kitchens *et al.* (Kitchens *et al.*, 2003) have employed a total interaction energy model to correlate the solvent-ligand interaction with the maximum size of a ligand stabilized nanoparticle that can be dispersed within a given solvent system. The total interaction energy, Φ_{total}, is the sum of attractive and repulsive terms, Equation 4.1, depends on nanoparticle size, distance between nanoparticles, ligand

density, and solvent properties.

$$\Phi_{total} = \Phi_{vdW} + \Phi_{osm} + \Phi_{elas} \tag{4.1}$$

where Φ_{vdW} is the van der Waals attractive potential, Φ_{osm} is the osmotic repulsive potential, and Φ_{elas} is the elastic repulsive potential. The van der Waals attractive potential (Hamaker, 1937), given in Equation 4.2, increases with an increase in nanoparticle radius or with a decrease in center to center separation distance between the nanoparticles.

$$\Phi_{vdw} = -\frac{A_{131}}{6}\left[\frac{2R^2}{d^2 - 4R^2} + \frac{2R^2}{d^2} + \ln\left(\frac{d^2 - 4R^2}{d^2}\right)\right] \tag{4.2}$$

where A_{131} is the Hamaker constant, R is the nanoparticle radius, and d is the center-to-center separation distance. The Hamaker constant is a proportionality factor that accounts for the interaction between two nanoparticles of the same material (component 1) through a solvent medium (component 3).

$$A_{131} \approx \left(\sqrt{A_{11}} - \sqrt{A_{33}}\right)^2 \tag{4.3}$$

where A_{11} is a constant value for the metallic nanoparticle material (A_{11} = 2.185 eV for silver (Shah *et al.*, 2002a) interacting through a vacuum and A_{33}, for the solvent, is calculated by an equation of state based on Lifshitz theory (Israelachvili, 1985)

$$A_{33} = \frac{3}{4}k_B T\left(\frac{\epsilon_3 - \epsilon_{\text{vacuum}}}{\epsilon_3 - \epsilon_{\text{vacuum}}}\right)^2 + \frac{3h\nu_e}{16\sqrt{2}}\frac{\left(n_3^2 - n_{\text{vacuum}}^2\right)^2}{\left(n_3^2 - n_{vacuum}^2\right)^{3/2}} \tag{4.4}$$

where k_B is Boltzmann's constant, T is temperature, ϵ_3 and ϵ_{vacuum} are the dielectric constants for the solvent and vacuum, respectively, h is Planck's constant, ν_e is the main electronic UV absorption frequency (generally assumed to be $3 \cdot 10^{15}\ s^{-1}$), and n_3 and n_{vacuum} are the reflective constants for the solvent and vacuum, respectively. Values of

the refractive index and dielectric constant for CO_2 (Sun *et al.*, 2003) and organic solvents (Lide, 1994; Lide, 1995) at 25 °C are given in Table 4.1 and values of n_{vacuum} and ϵ_{vacuum} are taken as unity.

Equation 4.3 applies to a binary system with one solvent and one nanoparticle material. However, gas-expanded liquids are mixtures of two solvent components (in this case, CO_2 and hexane), therefore a new mathematical expression, Equation 4.5, was developed (Anand *et al.*, 2008) to calculate the Hamaker constant, where 3′ represents one of the solvent components (in this case CO_2) and 3″ represents the other solvent component (in this case hexane).

$$A_{131} \approx \left[\sqrt{A_{11}} - \left(\tilde{\phi}_{3'} \sqrt{A_{(33)'}} + \tilde{\phi}_{3''} \sqrt{A_{(33)''}} \right) \right]^2 \tag{4.5}$$

where $\tilde{\phi}_{3'}$ is the CO_2 volume fraction in the solvent mixture excluding the ligand, and $A_{(33)'}$ is the Hamaker constant for CO_2, $\tilde{\phi}_{3''}$ is the volume fraction of hexane in the solvent mixture excluding the ligand, and $A_{(33)''}$ is the Hamaker constant for hexane.

For the repulsive contribution, Vincent *et al.* (Vincent *et al.*, 1980; Vincent *et al.*, 1986) proposed osmotic and elastic repulsive terms where the osmotic term is related to the solvation of the ligand tails between nanoparticles. The osmotic term depends on the free energy of the solvent-ligand tail interactions. On the other hand, the elastic term results from the entropic losses due to the compression of ligand tails present between two metal cores. Shah *et al.* (Shah *et al.*, 2002b) introduced these two repulsive terms, originating from "soft sphere" theory, to the total interaction energy to balance the van der Waals forces of attraction between nanoparticles. These repulsive contributions, as given in Equation 4.6, depend largely on the ligand length and solvent parameters as well

Compound	Molar Volume v_L cm^3/mol	Solubility Parameter δ $(J/cm^3)^{1/2}$	Dielectric Constant ϵ	Refractive Index n
CO_2	55	12.3	1.483	1.185
Hexane	132	14.9	1.882	1.372

Table 4.1: Physical properties of carbon dioxide and hexane solvents at 25°C.

as on the nanoparticle radius and surface-to-surface separation distance.

$$\Phi_{osm} = \frac{4\pi R k_B T}{(v_{solv}/N_A)}\phi^2\left(\frac{1}{2}-\chi\right)\left(l-\frac{h}{2}\right)^2 \quad \text{if } l<h<2l \quad (4.6a)$$

$$\Phi_{osm} = \frac{4\pi R k_B T}{(v_{solv}/N_A)}\phi^2\left(\frac{1}{2}-\chi\right)\left[l^2\left(\frac{h}{2l}-\frac{1}{4}-\ln\left(\frac{h}{l}\right)\right)\right] \quad \text{for } h<l \quad (4.6b)$$

$$\Phi_{elas} = \frac{2\pi R k_B T l^2 \phi\rho}{MW_2}\left\{\frac{h}{l}\ln\left[\frac{h}{l}\left(\frac{3-h/l}{2}\right)^2\right]-6\ln\frac{3-h/l}{2}+3\left(1-\frac{h}{l}\right)\right\} \quad \text{for } h<l \quad (4.6c)$$

where v_{solv} is the molar volume of the solvent, N_A is Avogadro's number, χ is the Flory-Huggins interaction parameter, h is the separation distance from the nanoparticle surfaces calculated using Equation 4.7, ρ is the ligand density, and MW_2 is the ligand molecular weight.

$$h = d - 2R \quad (4.7)$$

The Flory-Huggins interaction parameter in the osmotic repulsive term and is a function of the Hildebrand solubility parameter (δ_i) of the solvent and ligand (component 2)

$$\chi_{32} = \frac{v_3}{\mathrm{R}T}(\delta_3-\delta_2)^2 \quad (4.8)$$

where v_3 is the molar volume of the solvent and R is the ideal gas constant.

The osmotic repulsive terms, given above, apply to one solvent interacting with the ligand tails, but in the case of the two solvents in the gas expanded liquid new mathematical expressions were developed (Anand *et al.*, 2008)

$$\Phi_{osm} = \frac{4\pi R k_B T}{(v_M/N_A)}\phi^2\left[x_{3'}\left(\frac{1}{2}+\tilde{\phi}_{3''}r_{3'}\chi_{3'3''}-r_{3'}\chi_{3'2}\right)+ x_{3''}\left(\frac{1}{2}-r_{3''}\chi_{3''2}\right)\right]\left(l-\frac{h}{2}\right)^2 \quad \text{if } l<h<2l \quad (4.9a)$$

$$\Phi_{osm} = \frac{4\pi R k_B T}{(v_M/N_A)}\phi^2\left[x_{3'}\left(\frac{1}{2} + \tilde{\phi}_{3''} r_{3'}\chi_{3'3''} - r_{3'}\chi_{3'2}\right) + x_{3''}\left(\frac{1}{2} - r_{3''}\chi_{3''2}\right)\right]\left[l^2\left(\frac{h}{2l} - \frac{1}{4} - \ln\left(\frac{h}{l}\right)\right)\right] \quad \text{if } h < l \quad (4.9b)$$

where v_M represents the molar volume of the solvent mixture of CO_2 and hexane excluding the ligand, $\tilde{\phi}_{3''}$ is the volume fraction of hexane in the CO_2 and hexane solvent mixture excluding the ligand, ϕ is the ligand volume fraction, r is the molecular segment lengths (assumed to be $r_{3'} = 1$ and $r_{3''} = v_{3''}/v_{3'}$), and $x_{3'}$ and $x_{3''}$ are mole fractions of CO_2 and hexane, respectively, in the solvent mixture of CO_2 and hexane *excluding* the ligand. Molar compositions and molar volumes of the liquid phase for CO_2 expanded hexane at 25°C, given in Table 4.2, were calculated using the Peng-Robinson equation of state with the binary interaction parameter set as 0.125 ($k_{12} = 0.125$ for CO_2 and hexane). The Peng-Robinson equation of state has been successfully applied to similar CO_2-expanded liquid systems at these operating conditions with $k_{12} > 0.1$ ($k_{12} = 0.12$ for a toluene - CO_2 system) (Dixon & Johnston, 1991; Anand *et al.*, 2005). As can be seen from these equations and from Figure 4.1, the repulsive energies do not contribute to the total interaction energy until the separation distance is less than twice the ligand length.

The ligand volume fraction was calculated by modeling the ligand as a cylindrical structure extending from the nanoparticle surface. Saunders and Korgel (Saunders & Korgel, 2004) state that the ligand surface coverage, defined as the percentage of nanoparticle surface atoms bound to a ligand molecule, varies with nanoparticle size from 30% for small nanocrystals (< 4 nm) to 60% for larger nanoparticles. Korgel et. al. (Saunders & Korgel, 2004) determined that thiol ligands have a surface coverage of 75 ± 10% on silver nanoparticle surfaces for nanoparticles 4 to 7 nm in diameter. Equation 4.10 gives the ligand volume fraction, ϕ, as a function of the ligand surface coverage, Γ, where Γ was taken as 0.75 in this study except where noted.

Pressure	Volume Fraction		Mole Fraction		Molar Volume
(bar)	Hexane	CO_2	Hexane	CO_2	(cm^3/mol)
0	1	0	1	0	131
34.5	0.732	0.268	0.529	0.471	88
37.9	0.670	0.330	0.460	0.540	84
41.4	0.634	0.366	0.416	0.584	79
43.1	0.600	0.400	0.380	0.620	76
44.8	0.560	0.440	0.350	0.650	74
48.3	0.468	0.532	0.265	0.735	68

Table 4.2: Composition and molar volumes of the liquid phase for CO_2-expanded hexane at 25°C calculated using the Peng-Robinson equation of state.

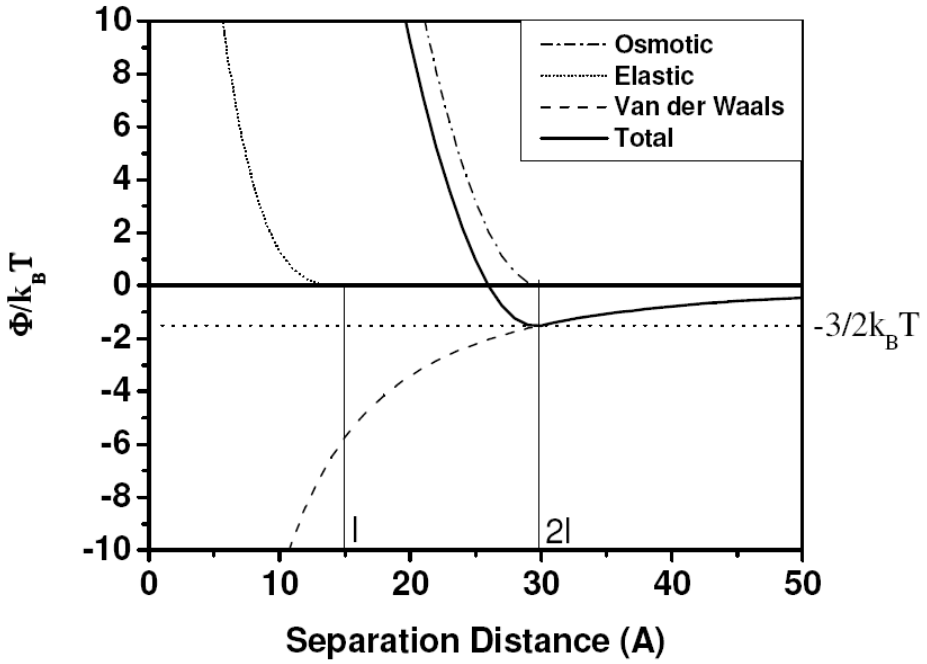

Figure 4.1: Representation of the attractive and repulsive potentials contributing to the total interaction energy for 12.6 nm 1-dodecanethiol-stabilized silver nanoparticles dispersed in CO_2-expanded hexane

$$\phi = \Gamma \left[\frac{3R^2 l}{(R+l)^3 - R^3} \right] \tag{4.10}$$

4.3 Results and Discussion

Contributions to the total interaction energy were calculated for CO_2-expanded hexane at various pressures below the vapor pressure of pure CO_2 (52.7 bar at 20°C). The relative contributions of these forces are shown in Figure 4.1 as a function of the separation distance, h, at a CO_2 pressure of 34.5 bar. The dotted-line in Figure 4.1 represents the minimum threshold energy, $-3/2k_BT$, necessary to disperse nanoparticles of a given size within the bulk solvent. The total interaction energy for a given nanoparticle size should be above this minimum threshold energy at a given set of conditions in order to disperse the nanoparticles. Due to van der Waals forces of attraction, if nanoparticles are not sufficiently stabilized and solvated in the medium, they will flocculate and precipitate. If nanoparticles are larger than the threshold size, the minimum in the total interaction energy curve for those sized nanoparticles would drop below $-3/2k_BT$ and those nanoparticles will precipitate. The sum of the elastic and repulsive forces thereby counteracts the van der Waals forces of attraction resulting in an increase in nanoparticle dispersibility.

The elastic term, which accounts for ligand-ligand interactions, depends on ligand density and the volume fraction. This term contributes minimally to the total interaction energy except at low separation distances (i.e., where the ligands of one nanoparticle interacts with the core of the other). On the other hand, the osmotic force strongly counteracts the van der Waals forces of attraction and enables nanoparticle dispersion within the bulk solvent. The osmotic force depends on the solvent molar volume, ligand length, ligand volume fraction, and solvent-ligand interaction. Adjusting the ligand-solvent interaction provides a means to control the inter-nanoparticle potential. Thus, stabilized particles can be induced to precipitate by the addition of an antisolvent, thereby

decreasing the solvent strength and reducing the solvent-ligand interaction below the value necessary to disperse a given nanoparticle. In the example shown in Figure 4.1, the maximum size of the particles that can be stabilized at the given conditions can be obtained by equating the total interaction energy with the Boltzmann threshold stabilization energy ($-3/2k_BT$). To improve the CO_2-expanded liquid nanoparticle precipitation process, it would be important to predict the threshold nanoparticle size where nanoparticles larger than this threshold size would precipitate and nanoparticles smaller than this threshold size would remain dispersed at a given set of conditions. In this study, the threshold nanoparticle size that can be precipitated/dispersed at various operating conditions in the CO_2-expanded mixtures has been calculated. In Figure 4.1, a hexane/CO_2 mixture at a CO_2 pressure of 34.5 bar results in a threshold particle size of 12.6 nm for dodecanethiol-stabilized silver nanoparticles.

Three basic phenomenological variations of the total interaction energy model were considered, based on the nature of the interaction between the ligand tails and the solvent. A schematic of these three models is given in Figure 4.2, illustrating the ligand tail arrangement and position within the solvent environment to depict differences in tail solvation and ligand length accessibility by the solvent. In the Extended Ligand Length Solvation Model (ELLSM), ligand tails are considered to be fully extended and the entire length of the tail is available to interact with the solvent. In the Condensed Phase Model (CPM), the ligand tails are considered to be condensed on the nanoparticle surface due to poor solvent strength and effective ligand lengths available for solvation were calculated by assuming the ligand volume fraction as unity. In the Limited Ligand Length Solvation Model (LLLSM), effective ligand lengths available for interaction with solvent were determined by matching the model predicted nanoparticle size to the size obtained from the size fractionation experiments at a given set of conditions using the ligand length as an adjustable parameter. Hence effective ligand lengths were calculated such that the model predictions matched the experimental data.

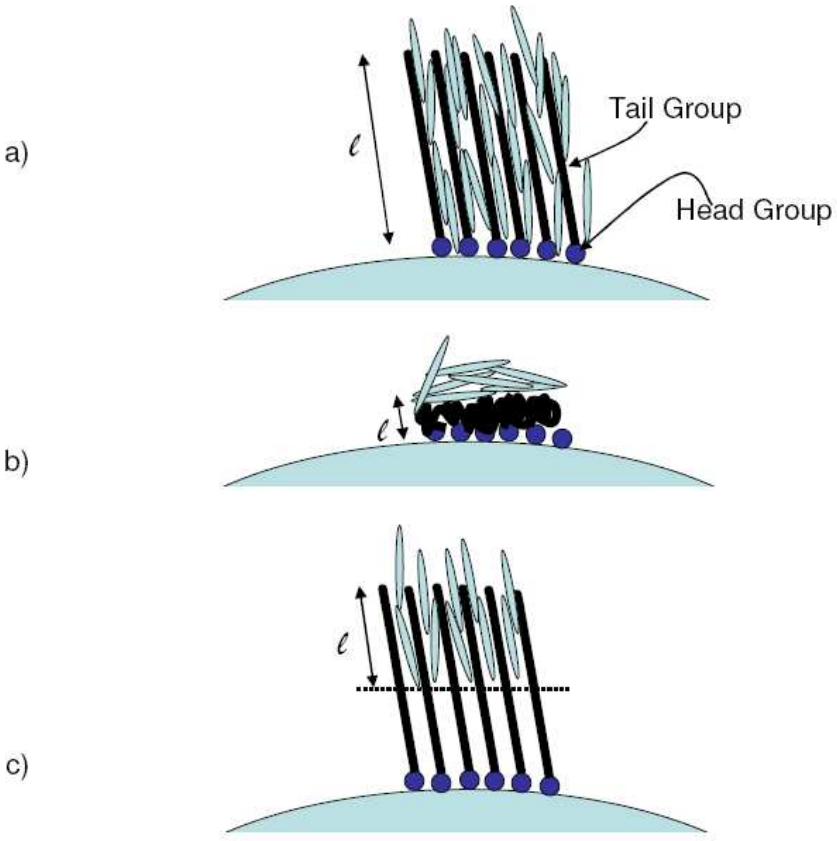

Figure 4.2: Schematic of the three phenomenological models used to estimate the threshold nanoparticle size for the precipitation/dispersion in CO_2-expanded hexane size fractionation process. (a) Extended Ligand Length Solvation Model, (b) Condensed Phase Model, and (c) Limited Ligand Length Solvation Model.

4.3.1 Extended Ligand Length Solvation Model (ELLSM)

In this model, it was assumed that the alkyl ligand tail is fully extended from the nanoparticle surface and solvated by the solvent as shown in Figure 4.2a. The threshold nanoparticle size precipitated/dispersed at a set of given solvent conditions was calculated by balancing the total interaction energy with the Boltzmann threshold stabilization energy ($-3/2k_BT$), assuming the entire ligand length (15 Å for dodecanethiol) interacts with the solvent. Table 4.3 presents the dispersed threshold nanoparticle size predicted by the model for various CO_2 pressures that correspond to conditions used in previous CO_2-expanded hexane nanoparticle precipitation experiments (Anand *et al.*, 2005). For the ELLSM, the calculated threshold nanoparticle diameters are consistently larger than experimental values. The calculated threshold nanoparticle size did not drastically change with increasing CO_2 pressure. Unfortunately, the ELLSM is unable to predict both the threshold size and the effect of pressure on this threshold size. To improve these calculations it is important to understand which parameters have the greatest influence on the stabilization threshold size and the effect of CO_2 pressure on this size as measured experimentally. A sensitivity analysis was performed on various parameters to understand which variables most affect these modeling results.

Given the non-ideality of these CO_2-expanded hexane mixtures, and the uncertainty of thermodynamic mixing rules, a sensitivity analysis was performed on literature obtained CO_2 properties to determine the impact of potential measurement errors on the predicted threshold nanoparticle sizes. The sensitivity analysis was also performed to analyze the impact of CO_2 properties and other model parameters such as effective ligand length, surface coverage of the ligands, solvent mixture volume, and the Hamaker constant of the silver nanoparticles on the predicted threshold nanoparticle size. The sensitivity analysis consisted of increasing or decreasing each parameter by 30% from the baseline value in order to determine the variation in the threshold nanoparticle size obtained. Note that at a CO_2 pressure of 34.5 bar using the ELLSM, the base parameter

Experimental		Theoretical			
Pressure Range (bar)	Mean Diameter (nm)	Pressure (bar)	Threshold Nanoparticle Diameter (nm)		
			ELLSM	CPM	LLLSM
0-34.5	6.7	34.5	12.6	6.7	6.7
34.5-37.9	6.6	37.9	12.5	6.6	6.6
37.9-41.4	5.8	41.4	12.4	5.8	5.8
41.4-43.1	5.3	43.1	12.3	5.3	5.3
43.1-44.8	4.8	44.8	12.2	4.8	4.8
44.8-48.3	4.1	48.3	12.0	4.1	4.1

Table 4.3: Comparison of experimental 1-dodecanethiol stabilized silver nanoparticle diameters obtained at different pressure intervals in the CO_2 gas-expanded liquid size fractionation process and predicted diameters using three models on total interaction energy.

values yielded a threshold size of 12.6 nm, and the sensitivity to these parameters is determined by comparing the increased and decreased values to this base case of 12.6 nm. Also note that the experimental nanoparticle size at these conditions is 6.7 nm, compared to the ELLSM predicted size of 12.6 nm. Among all the parameters investigated, the ligand length (15 Å) has the greatest influence on the threshold nanoparticle size, where the nanoparticle size increased from 12.6 nm to 16.4 nm with a 30% increase (19.5 Å) in the ligand length. The threshold nanoparticle size was also changed from 12.6 nm to 8.8 nm with a 30% decrease (10.5 Å) in the ligand length. It is reasonable, based on discussions below, that the entire ligand length would not be available for complete solvation by the solvent medium. Therefore, the effective ligand length in the model could be decreased more than the 30% used in this sensitivity analysis in order to finely tune the threshold nanoparticle size to match the experimental obtained results. The effect of the degree of ligand solvation accounted for in the model by adjusting the "effective" ligand length is demonstrated in Figure 4.3 which shows the total interaction energy for three different ligand lengths (10.5, 15, and 19.5 Å). Due to this sensitivity analysis, we find that the ligand length has the most pronounced effect on the threshold nanoparticle size predicted in the ELLSM. As such, two other variations of this model were developed to explain our experimental results based on differing degrees of tail solvation and "effective" ligand lengths for this solvation.

4.3.2 Condensed Phase Model (CPM)

De Gennes (De Gennes, 1976a; De Gennes, 1976b; Brochard & de Gennes, 1977) has shown that for a poor solvent, a polymer chain interacts more with itself than with the solvent and forms knots on itself. In other words, when polymers interact favorably with the solvent, they will extend more into the solvent whereas in a poor solvent the polymer collapses and condenses. In the current study, the addition of the CO_2 antisolvent decreases the solvent strength of the mixture thereby reducing the ligand length interacting with the

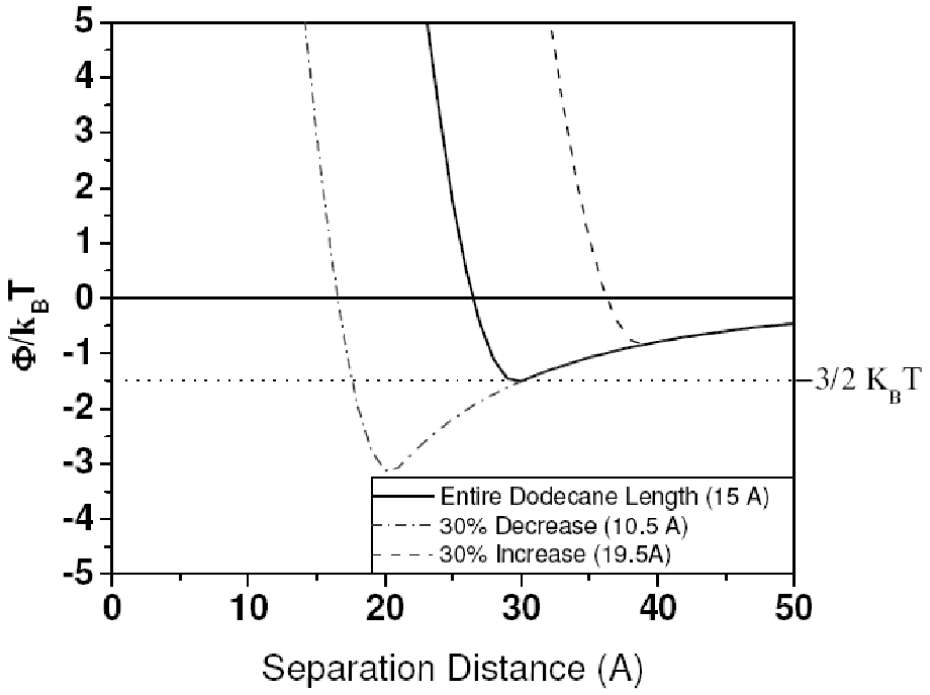

Figure 4.3: Demonstration of the effect of the degree of ligand solvation on the total interaction energy with a 30% increase and a 30% decrease in the effective 1-dodecanethiol ligand length

Pressure (bar)	Condensed Phase Model (75% Surface Coverage)		Condensed Phase Model (Variable Surface Coverage)			Limited Ligand Length Solvation Model (75% Surface Coverage)	
	Effective Ligand Length (Å)	Threshold Nanoparticle Size (nm)	Surface Coverage (%)	Effective Ligand Length (Å)	Threshold Nanoparticle Size (nm)	Effective Ligand Length (Å)	Threshold Nanoparticle Size (nm)
34.5	8.8	7.2	69.3	8.2	6.7	8.2	6.7
37.9	8.7	7.1	69.2	8.2	6.6	8.1	6.6
41.4	8.5	6.9	63.3	7.4	5.8	7.3	5.8
43.1	8.4	6.7	60.3	7.0	5.3	6.8	5.3
44.8	8.2	6.5	60.2	6.9	4.8	6.3	4.8
48.3	7.9	6.1	58.3	6.5	4.1	5.9	4.1

Table 4.4: Effective ligand lengths and threshold silver nanoparticle sizes as a function of CO_2 pressure.

now poorer solvent. An alternative to the ELLSM is a scenario where the solvent strength would be low enough that the ligand tails are completely condensed on the nanoparticle surface. Figure 4.2b demonstrates the condensed phase arrangement of thiol tails with a ligand volume fraction considered to be unity. This model is referred to as the Condensed Phase Model (CPM) since it assumes all the thiol tails are collapsed and condensed. The effective ligand length which is available for interaction is calculated by setting the ligand volume fraction in Equation 4.10 equal to one and solving for the ligand length, for a given nanoparticle diameter obtained experimentally. A ligand length of 8.8 Å was obtained for a 6.7 nm diameter particle as given in Table 4.4. The effective ligand length has reduced from 15 Å (ELLSM) to 8.8 Å (CPM) for a 6.7 nm nanoparticle diameter. The effective ligand lengths at different CO_2 pressures were calculated assuming a ligand surface coverage of 75% (Saunders & Korgel, 2004) for each experimental nanoparticle size obtained at a particular CO_2 pressure. Total interaction energy calculations were performed with these new effective ligand lengths and the respective ligand solubility parameters that correspond to these alkyl tail lengths. The predicted threshold nanoparticle size obtained from the CPM is significantly lower than the ELLSM and closer to the experimental data as shown in Figure 4.4. Unfortunately, these results still slightly over-predict the threshold nanoparticle diameters at the lowest pressure of 34.5 bar and while a decrease in diameter is observed with increasing CO_2 pressure the model does not demonstrate the pressure dependent variability on the threshold nanoparticle diameter observed experimentally. While the CPM does not capture the effect of CO_2 pressure compared to the experimental data, it does illustrate that limited tail solvation likely accounts for the differences in the ELLSM and the experimental results.

In an effort to account for the difference between the threshold nanoparticle diameters obtained from the Condensed Phase Model with constant surface coverage and the experimental data, the degree of surface coverage in the CPM was adjusted from the literature value of 75% (Saunders & Korgel, 2004). These results are shown in Table 4.4

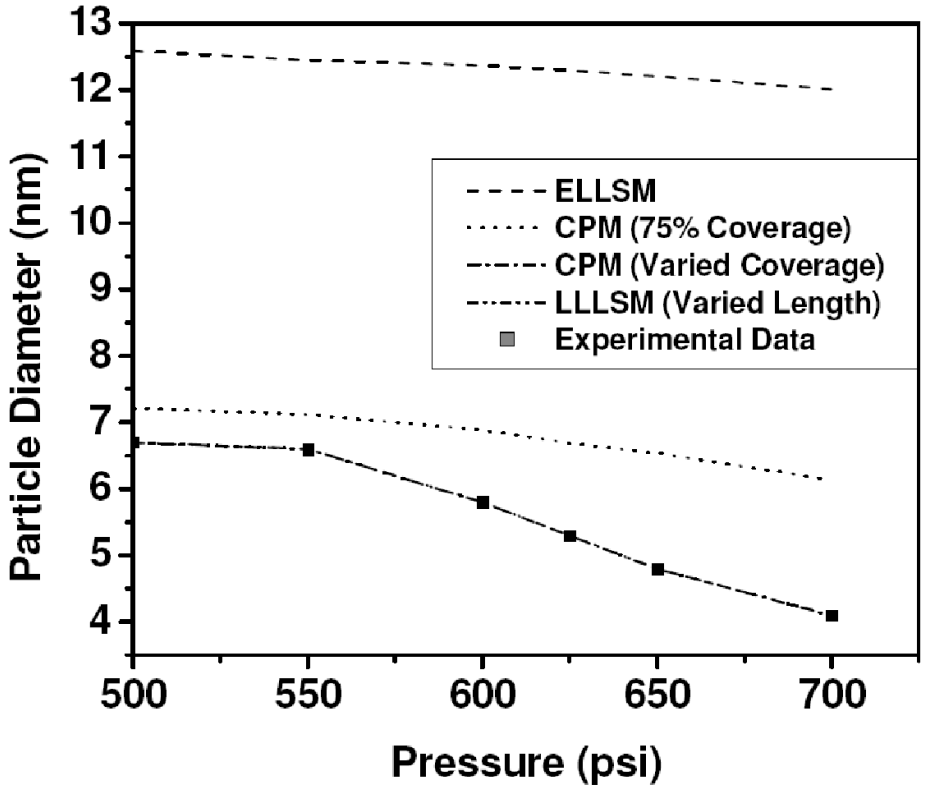

Figure 4.4: Comparison of 1-dodecanethiol stabilized silver nanoparticle diameters precipitated in CO_2 gas-expanded hexane experiments and threshold nanoparticle diameters predicted using ELLSM, CPM, and LLLSM compared to experimental results

and indicate that a small variation in surface coverage from 69.3% to 58.3% can account for the change in particle size precipitated at the various experiment pressures. The model was fit to the experimental data at each pressure by adjusting the surface coverage and determining the corresponding effective length according to Equation 4.10. These results also indicate that the degree of ligand tail solvation and the ligand surface coverage are the most important parameters for controlling nanoparticle dispersability. It has been shown in literature that the ligand surface coverage does not remain constant for all nanoparticle sizes (Dixon & Johnston, 1991). One major concern with the CPM model involves the duality of the ligand tails being completely condensed on the nanoparticle surface while also being able to interact with the solvent through tail solvation. There is experimental evidence that thiol tails (carbon backbones greater than 9 carbons) on a metal surface are in the extended mode (Porter *et al.*, 1987). This suggests that the Condensed Phase Model may not be the correct phenomenological model for our experimental system.

4.3.3 Limited Ligand Length Solvation Model LLLSM

Another model where the ligand tails are fully extended yet the entire length is not accessible to the solvent, such that the effective ligand length which is interacting with the solvent is smaller than the total ligand length. This effective ligand length decreases with an increase in the antisolvent CO_2concentration (i.e., pressure) due to the weaker solvent mixture being unable to completely solvate the ligand tails was considered. In other words, the total ligand length is extended but only part of it is interacting with the solvent because only a portion of the ligand length is in contact with the solvent. As shown in Figure 4.2c, if the ligand tails are densely packed it would be very difficult for the hexane solvent molecules, which are half the length of dodecanethiol ligand molecules, to penetrate the tortuous path between the ligand tails and solvate the entire ligand length. Effective ligand lengths were obtained by matching the threshold nanoparticle size predicted from the total interaction energy model with the experimental results at

constant ligand surface coverage of 75%. Ligand solubility parameters were also adjusted according to the effective alkyl tail length in this model. The results from this Limited Ligand Length Solvation Model are given in Table 4.4. The effective ligand length required to disperse a threshold nanoparticle size of 6.7 nm at a CO_2 pressure of 34.5 bar is 8.2 Å compared to the 15 Å needed for complete solvation of the total length of the dodecanethiol ligand. Similarly, effective ligand lengths were calculated at each of the antisolvent CO_2 pressures by fitting the threshold nanoparticle size from the model to the experimental data at each of these CO_2 pressures. The total interaction energy model indicates that the effective ligand length of the dodecane alkyl tail which is available to the solvent decreases from 8.2 Å to 5.9 Å for the LLLSM corresponding to the silver nanoparticle sizes of 6.7 nm to 4.1 nm, and CO_2 pressures from 34.5 bar to 48.3 bar, respectively. These results indicate that changes in the effective ligand length, due to solvation changes, can account for both the dispersed particle size as well as the effect of CO_2 pressure.

4.4 Conclusions

A model was developed on the basis of total interaction energy to predict the threshold silver nanoparticle size which can be precipitated/dispersed in CO_2 gas-expanded liquids at various antisolvent CO_2 pressures. After deriving expressions for the osmotic energy term and the Hamaker constant that account for multiple solvent systems, the model was successfully applied to the CO_2-expanded liquid size separation process using the thermodynamic properties of CO_2 gas-expanded liquids. However, allowing complete solvation of the ligand length in the model results in threshold nanoparticle sizes too large when compared to the experimental results. Thus, three phenomenological variations of this total interaction energy model were considered where the Limited Ligand Length Solvation Model provided the best match of the threshold predicted nanoparticle sizes with the experimental results. This model shows that the degree of tail solvation strongly impacts the nanoparticle sizes and that limited ligand solvation is occurring and is a

function of CO_2 pressure. Very subtle changes in solvent strength result in a fine tuning of dispersed nanoparticle size and this modeling study improves our understanding of nanoparticle dispersability at various conditions alleviating the need for extensive experimentation.

Chapter 5

Modeling the Precipitation of Polydisperse Nanoparticles Using a Total Interaction Energy Model

5.1 Introduction

The precipitation and size-selective fractionation of nanoparticles is a crucial and, sometimes, necessary stage of post-synthesis nanomaterial processing in order to fine-tune the size-dependent properties of nanoparticles for their intended application. Unfortunately, these processes (specifically size-selective fractionation) are somewhat trial-and-error in their application and predicting the size and size-distribution of the recovered nanoparticle fractions is quite difficult. The ability to predict the size and size distributions of the nanoparticles that would disperse and precipitate at different solvent conditions would greatly reduce the need for experimentation and would provide new, physical insights into the underpinning thermophysical phenomena.

Traditionally, size-selective fractionation of nanoparticles has been accomplished through the controlled reduction of solvent strength of a thermodynamically stable nanoparticle dispersion by the addition of an antisolvent (Murray *et al.*, 2000) (e.g. aliphatic thiol stabilized nanoparticles dispersed in hexane can be precipitated and fractionated through the addition of ethanol). This liquid-liquid solvent/antisolvent precipitation and fractionation process produces large amounts of organic waste, is very time-intensive, and is only capable of producing monodisperse fractions through repetition. Another method of size-selectively precipitating nanoparticles was developed (Anand *et al.*, 2005; McLeod *et al.*, 2005b; Saunders & Roberts, 2009) in order to alleviate some of the drawbacks of the liquid-liquid precipitation and fractionation process which makes use of the tunable physico-chemical properties of gas-expanded liquids (GXL's): mixtures of an

organic solvent and a pressurized gas. An organic solvent (e.g. hexane) dispersion of aliphatic ligand (e.g. 1-dodecanethiol) stabilized metallic (e.g. gold) nanoparticles can be precipitated when pressured to sub-vapor pressure levels with CO_2. The CO_2 partitions (dissolves) into the organic solvent, and as CO_2 is a nonsolvent for the aliphatic ligand tails, the solvent strength of the overall solvent mixture is reduced, thus, inducing precipitation of the nanoparticles. The degree to which CO_2 is added to the solvent is simply a function of the applied CO_2 pressure (i.e. CO_2 has a greater solubility at higher applied pressures). Several apparatuses have been developed to make use of this phenomenon in order to size-selectively fractionate polydisperse nanoparticles. Details on this method is available elsewhere (McLeod *et al.*, 2005b; Saunders & Roberts, 2009), but in short, if an organic dispersion of nanoparticles is pressurized with CO_2 to a point where only a portion of the nanoparticles precipitate (the largest nanoparticles will precipitation first upon worsening solvent conditons), the nanoparticles which remain dispersed (the smallest nanoparticles) in the solvent mixture can be removed from the precipitated nanoparticles, thereby achieving an effective fractionation.

Modeling of these post-synthesis processes involving aqueous nanoparticle dispersions have been successfully accomplished through the use of Derjaguin, Landau, Verwey and Overbeek (DLVO) theory (Adamczyk & Weronski, 1999; Kim *et al.*, 2005; Kim *et al.*, 2008). In order to reduce the difficulty of accomplishing nanoparticle precipitation and size-selective fractionation, many of the processes make use of organics solvents (e.g. the liquid/liquid and GXL precipitation and fractionations). DLVO theory is unable to make accurate predictions of non-aqueous nanoparticle dispersions due to the lack of electrostatic repulsions (Sato, 1993). Similar to the basic principles of DLVO theory, total interaction energy models make use of the sum of the attractive and repulsive potentials for all forces which act upon the nanoparticles, albeit different forces than those employed in DLVO theory. Total interaction energy models have been applied to nanoparticle dispersions in traditional liquids (Kitchens *et al.*, 2003), compressed fluids (Kitchens &

Roberts, 2004), supercritical fluids (Shah *et al.*, 2002a; Shah *et al.*, 2002b), and, most recently, GXL's (Anand *et al.*, 2008).

The model developed by Anand *et al.* (Anand *et al.*, 2008) attempted to predict the size of a nanoparticle that could be dispersed at a defined set of solvent conditions in a GXL by calculating the total interaction energy of two identical nanoparticles interacting through the solvent medium. This size was defined as a "threshold size" (i.e., all nanoparticles above this size would precipitate and all smaller nanoparticles would remain dispersed). Three phenomenological models were used to explain the physical nature of the solvent-ligand interactions. In the Extended Ligand Length Solvation Model (ELLSM), ligand tails were considered to be fully extended and the entire length of the tail is available to interact with the solvent. In the Condensed Phase Model (CPM), the ligand tails were considered to be condensed on the nanoparticle surface due to poor solvent strength. In the Limited Ligand Length Solvation Model (LLLSM), only a portion of the ligand length was available for solvation. However this model only accounted for nanoparticles of the same size interacting with each other which does not accurately represent the range of interactions that would occur in a polydisperse distribution of nanoparticles. Nonetheless, one of the major findings of this previous study was that the ligand length available for solvation would be reduced as the solvent strength of the system weakens (i.e., as CO_2 is added to the system). This finding was later confirmed by White *et al.* by small angle neutron scattering of nanoparticle dispersions in a GXL. White and coworkers found that as CO_2 is added to a hexane dispersion of 1-dodecanethiol-stabilized silver nanoparticles, the thickness of the ligand shell decreased, as seen in Figure 5.1 (White & Kitchens, 2010).

The model presented here attempts to accurately predict the size and size distribution of precipitated and dispersed nanoparticle fractions by calculating the total interaction energy for two differently sized nanoparticles interacting while accounting for the known, and well defined, ligand collapse through the presentation of a new phenomenological model describing the interaction between the solvent and ligand. While the model

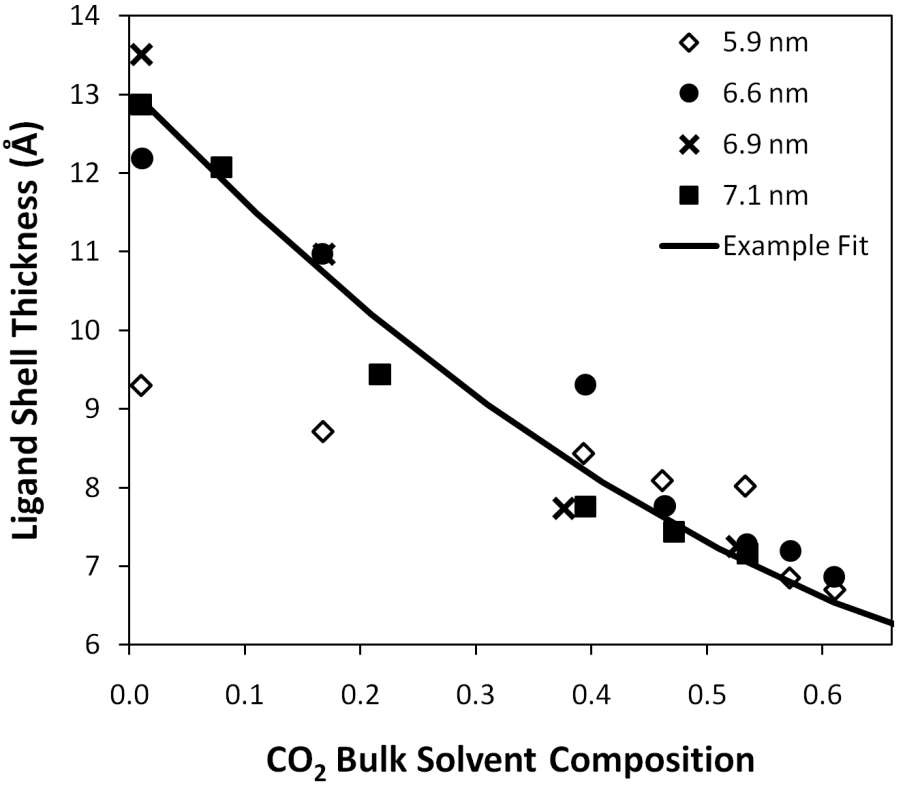

Figure 5.1: Ligand shell thickness of varying sized silver nanoparticles stabilized with 1-dodecanethiol as a function of CO_2 solvent composition (White & Kitchens, 2010)

presented compares results to a size-selective fractionation process, this model could potentially be used to model any system of sterically stabilized polydisperse nanoparticles and the effect of varying the ligand length, solvent strength, etc.

5.2 Theory

The total interaction energy, Φ_{total}, of two interacting nanoparticles is the sum of all known attractive and repulsive forces acting on the system and is given as

$$\Phi_{\text{total}} = \Phi_{\text{vdw}} + \Phi_{\text{osm}} + \Phi_{\text{elas}} \tag{5.1}$$

where Φ_{vdw} is the van der Waals attractive potential, Φ_{osm} is the osmotic repulsive potential, and Φ_{elas} is the elastic potential. The non-retarded van der Waals potential (Hamaker, 1937) for two interacting spheres of different sizes is given as

$$\Phi_{\text{vdw}} = -\frac{A_{131}}{6}\left[\frac{2R_1R_2}{f_1} + \frac{2R_1R_2}{f_2} + \ln\left(\frac{f_1}{f_2}\right)\right] \tag{5.2a}$$

where

$$f_1 = h^2 + 2R_1h + 2R_2h \tag{5.2b}$$

$$f_2 = h^2 + 2R_1h + 2R_2h + 4R_1R_2 \tag{5.2c}$$

where A_{131} is the Hamaker constant for the nanoparticle material interacting through the solvent (see Table 5.1 for subscript summary), R_1 and R_2 are nanoparticle diameters, and h is the surface-to-surface centerline separation distance (Hiemenz, 1986). The Hamaker constant must account for the binary gas-expanded solvent (CO_2-expanded hexane) which can be approximated (Anand *et al.*, 2008) as

$$A_{131} \approx \left[\sqrt{A_{11}} - \left(\tilde{\phi}_{3'}\sqrt{A_{3'3'}} + \tilde{\phi}_{3''}\sqrt{A_{3''3''}}\right)\right]^2 \tag{5.3}$$

where A_{ii} is the i-th component (see Table 5.1) Hamaker constant interacting in a vaccuum, and $\tilde{\phi}_i$ is the bulk solvent (beyond the nanoparticle ligand shell) volume fraction of component i. The nanoparticle Hamaker constant (A_{11}) is taken as the literature value ($3.5 \cdot 10^{-19}$ J for gold (Parsegian, 1981)) whereas the solvent Hamaker constants ($A_{3'3'}$ and $A_{3''3''}$, for CO_2 and hexane, respectively) are calculated according to Liftshitz theory(Israelachvili, 1985).

Two repulsive contributions (Vincent *et al.*, 1980; Vincent *et al.*, 1986), an osmotic repulsion and elastic repulsion, are used to balance the attractive van der Waals potential. The osmotic repulsive force arises from the free energy of the solvent-ligand interaction (i.e., competition of the solvent to solvate the ligands). This contribution only arises when the ligands of one nanoparticle can interact with the ligands of another nanoparticle, specifically, when $L < h < 2L$ where L is the thickness of the ligand shell. Vincent *et al.* (Vincent *et al.*, 1986) gave this potential for a polymer stabilized ligand dispersed in a neat solvent as

$$\Phi_{\text{osm}} = \frac{4\pi R_1 k_B T}{(v_{solv}/N_A)} \phi^2 \left(\frac{1}{2} - \chi\right)\left(L - \frac{h}{2}\right)^2 \quad \text{for } L < h < 2L \tag{5.4}$$

where k_B is the Boltzmann constant, T is the temperature, v_{solv} is the solvent molar volume, N_A is Avogadro's constant, ϕ is the volume fraction of the ligand in the ligand shell, and χ is the Flory-Huggins interaction parameter. As the surface-to-surface separation distance between the nanoparticles decreases to the point where the ligands of one nanoparticle can interact with the core of the other nanoparticle ($h < L$), the osmotic repulsive term needs to account for the elastic deformation of the ligands and was given as

$$\Phi_{\text{osm}} = \frac{4\pi R_1 k_B T}{(v_{solv}/N_A)} \phi^2 \left(\frac{1}{2} - \chi\right)\left[L^2\left(\frac{h}{2L} - \frac{1}{4} - \ln\left(\frac{h}{L}\right)\right)\right] \quad \text{for } h < L \tag{5.5}$$

At these small surface-to-surface separation distances ($h < L$) the elastic repulsive contribution arises from the entropic losses due to compression of the ligand tails (i.e.,

Subscript	Component	Example
1	Nanoparticle Material	Gold
2	Ligand	1-Dodecanethiol
3	Solvent Mixture	CO_2 and Hexane
3′	Solvent Component	CO_2
3″	Solvent Component	Hexane

Table 5.1: Summary of component subscripts

analogous to a spring effect). Vincent *et al.* gave this repulsive contribution as

$$\Phi_{\text{elas}} = \frac{2\pi R_1 k_B T L^2 \phi \rho}{MW_2} \left\{ \frac{h}{L} \ln \left[\frac{h}{L} \left(\frac{3 - h/L}{2} \right)^2 \right] - 6 \ln \frac{3 - h/L}{2} + 3 \left(1 - \frac{h}{L} \right) \right\} \quad \text{for } h < L \tag{5.6}$$

where ρ and MW_2 are the density and molecular weight, respectively, of the ligand. These repulsive contributions are dependent on the assumption that the ligand volume is uniformly distributed throughout the ligand shell (Vincent *et al.*, 1986).

In order for two interacting nanoparticles to disperse, the minimum of the total interaction energy, where the repulsive forces perfectly balance the attractive forces, must be greater than or equal to the Brownian (thermal) motion energy.

$$\Phi_{\text{total}}\Big|_{min} \geq -\frac{3}{2} k_B T \tag{5.7}$$

The nanoparticles will be at the lowest possible energy state for the given conditions, all forces on the nanoparticles will be perfectly balanced and the nanoparticle pair will have enough energy to maintain normal Brownian motion. If the minimum of the total interaction energy of the interacting nanoparticles is less than the Brownian motion energy, the nanoparticle pair is unable to maintain the dispersion and must precipitate. Of particular interest is when the minimum of the total interaction energy is equal to the Brownian motion energy, as demonstrated in Figure 5.2. A system under these conditions would be dispersable and stable, any change to the system that would decrease the total interaction energy (e.g., increasing the nanoparticle sizes or decreasing the overall solvent strength) would create a situation where the nanoparticles would precipitate therefore the system is at the "threshold condition."

Vincent *et al.* developed the repulsive expressions for nanoparticles dispersed in a neat solvent. Anand *et al.* updated (Anand *et al.*, 2008) the expressions in order to account for the binary solvent of the gas-expanded liquid. In order to account for the

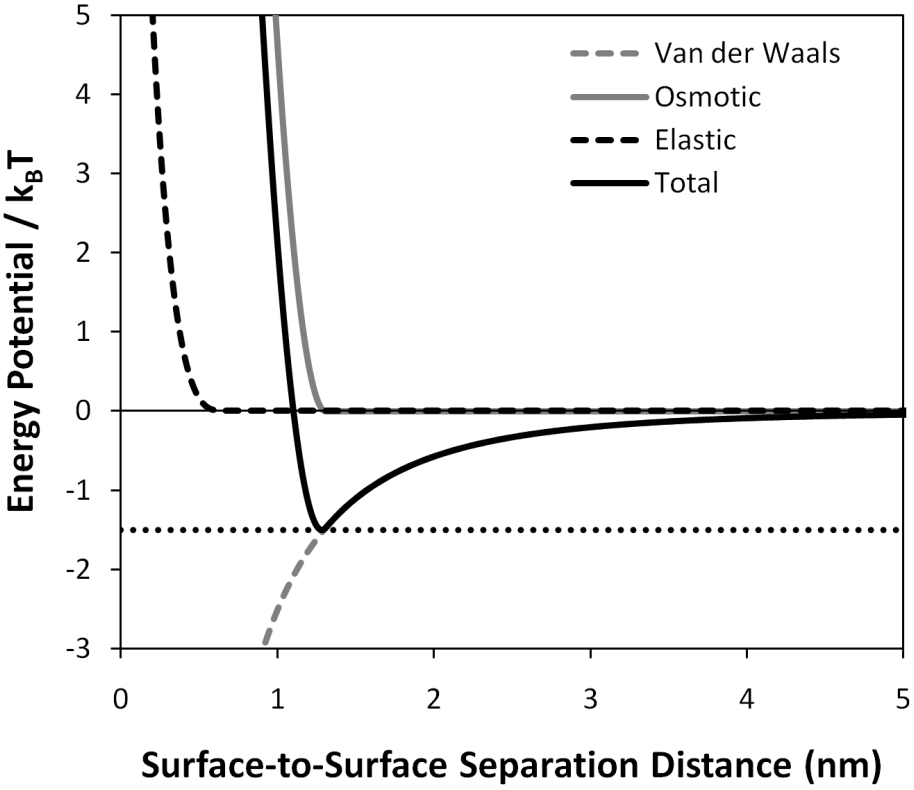

Figure 5.2: Contributions to the total interaction energy for a 5.0 nm gold nanoparticle interacting with a 7.1 nm gold nanoparticle in a solvent that is 40% hexane and 60% CO_2 (mol% in the bulk solvent). As the minimum of the total interaction energy is equal to $-3/2k_BT$, this situation is at the "threshold condition."

collapsing ligands as predicted by Anand *et al.* and confirmed by White *et al.* the bounds on the repulsive contributions need to be adjusted. It is assumed that the entire length of the ligand can be solvated by the solvent therefore the magnitude of the repulsive contributions when the ligands are collapsed are assumed to be equivalent to those when the ligands are fully extended. To paraphase, a new phenomenological model is presented which assumes the ligand shell is partially collapsed to a known degree but the entire length of the ligand is available for solvation. The repulsive contributions with these adjustments (accounting for the binary solvent mixture and the collapsing ligands) can be calculated by

$$\Phi_{\text{osm}} = \begin{cases} \dfrac{4\pi R_1 k_B T}{(v_{solv}/N_A)} \phi^2 \chi_{\text{osm}} \left(L_{ext} - \dfrac{h}{2} \right)^2 & \text{for } 1 < \dfrac{h}{L} < 2 \\ \dfrac{4\pi R_1 k_B T}{(v_{solv}/N_A)} \phi^2 \chi_{\text{osm}} \left[L_{ext}^2 \left(\dfrac{h}{2L_{ext}} - \dfrac{1}{4} - \ln\left(\dfrac{h}{L_{ext}} \right) \right) \right] & \text{for } \dfrac{h}{L} < 1 \, . \end{cases} \tag{5.8}$$

where

$$\chi_{\text{osm}} = x_{3'} \left(\frac{1}{2} + \tilde{\phi}_{3''} r_{3'} \chi_{3'3''} - r_{3'} \chi_{3'2} \right) + x_{3''} \left(\frac{1}{2} - r_{3''} \chi_{3''2} \right) \tag{5.9}$$

and

$$\begin{aligned} \Phi_{\text{elas}} = & \frac{2\pi R_1 k_B T L_{ext}^2 \phi \rho}{MW_2} \left\{ \frac{h}{L_{ext}} \ln \left[\frac{h}{L_{ext}} \left(\frac{3 - h/L_{ext}}{2} \right)^2 \right] \right. \\ & \left. -6 \ln \frac{3 - h/L_{ext}}{2} + 3 \left(1 - \frac{h}{L_{ext}} \right) \right\} \qquad \text{for } \frac{h}{L} < 1 \end{aligned} \tag{5.10}$$

where L_{ext} is the extended ligand length (12.8 Å for 1-dodecanethiol)(Porter *et al.*, 1987; Dubois & Nuzzo, 1992), x_i is the mole fraction of the i-th component (see Table 5.1) in the bulk solvent (determined by the Peng-Robinson equation of state), r_i is the segment length of the i-th component (assumed to be $r_{3'} = 1$ and $r_{3''} = v_{3''}/v_{3'}$), and χ_{ij} is the Flory-Huggins interaction parameter between components i and j (determined by solubility parameters). These forms of the repulsive contributions reduce to the Vincent equations (Equations 5.4-5.6) when the ligands are fully extended in a neat solvent.

The thickness of the ligand shell was determined from the White *et al.* SANS data (White & Kitchens, 2010). The data set was regressed with an expression of the form

$$L\left(x_{3'}\right) = c_1\left(x_{3'} - 1\right)^2 + L_{collapsed} \tag{5.11}$$

where c_1 is a regression parameter and $L_{collapsed}$ is the thickness of the ligand when fully collapsed. $L_{collapsed}$ was determined based on the size of the nanoparticle and evaluated by forcing $\phi = 1$, this is a physical constraint to ensure the system is physically plausible (i.e., the ligand never occupies more than 100% of the ligand shell) as the regression does extrapolate ligand shell thicknesses beyond $x_{3'} = 0.60$. White *et al.* hypothesized that the thickness of the ligand shell is a function of nanoparticle size due to the decreased thickness measured for the 5.9 nm nanoparticles as seen in Figure 5.1. However, as the other three data sets were grouped tightly, for the purposes of this study, the ligand thickness data for the 5.9 nm nanoparticles was disregarded as it was a single outlier relative to the others. An example fit is show in Figure 5.1.

The volume fraction of the ligand in the ligand shell (ϕ) was determined from the volume of the ligand per volume of the ligand shell.

$$\phi = \frac{3R_1^2\left(\frac{A_{thiol}}{A_{Au}}\right)\Gamma\left(R_1\right)L_{ext}}{\left(R_1 + L\right)^3 - R_1^3} \tag{5.12}$$

where A_{thiol} is the cross-sectional area of the ligand tail (14.5 Å^2 for dodecanethiol)(Korgel *et al.*, 1998; Saunders & Korgel, 2004), A_{Au} is the atomic gold radial cross-sectional area (6.51 Å^2)(Lide & Frederikse, 1995), and $\Gamma\left(R_1\right)$ is the ligand surface coverage ratio which is defined as

$$\Gamma \equiv \frac{\text{number of thiol molecules per nanoparticle}}{\text{number of gold surface atoms per nanoparticle}} \tag{5.13}$$

Hoestetler *et al.* have demonstrated (Hostetler *et al.*, 1998) that the surface coverage of ligand on a nanoparticle is a function of the nanoparticle size (see Figure 5.3). As the

nanoparticle radius approaches zero, a model of the ligand surface coverage ratio should asymptotically increase while as the nanoparticle radius increases, the ligand surface coverage ratio model should approach the flat surface coverage value. The data set was regressed with an expression of the form below as in inverse relationship statistically fit better than an exponential.

$$\Gamma(R_1) = \frac{c_2}{R_1} + \Gamma_{slab} \tag{5.14}$$

where c_2 is the regression parameter ($c_2 \approx 0.205$ nm) and Γ_{slab} is the ligand surface coverage of a flat surface, $\Gamma_{slab} = 1/3$ for gold(Dubois & Nuzzo, 1992).

5.2.1 Precipitation Threshold

In order to determine the nanoparticle size-combinations which will disperse or precipitate at a given set of solvent conditions, the total interaction energy needs to be calculated. The threshold nanoparticle size, R_2, is determined by a nonlinear solution algorithm (Levenberg-Marquardt) that would create the threshold condition with a nanoparticle of radius R_1

$$R_2 = f(R_1) : \Phi_{\text{total}} = -\frac{3}{2} k_B T \tag{5.15}$$

Any nanoparticle of radius greater than R_2 would precipitate when interacting with a nanoparticle of radius R_1 as the van der Waals potential would increase. It is assumed that the ligand shells of both nanoparticles are identical (i.e., L, ϕ, and Γ are calculated based on R_1). Examples of the threshold nanoparticle sizes are displayed in Figure 5.4. As the concentration of CO_2 in the bulk solvent increases, the threshold nanoparticle sizes decreases indicating that smaller and smaller nanoparticles are able to be dispersed in the weaker solvent. At a given set of solvent conditons, any combination of nanoparticle sizes that lie above that respective threshold curve will precipitate while those combinations that lie on or below the same curve will remain dispersed.

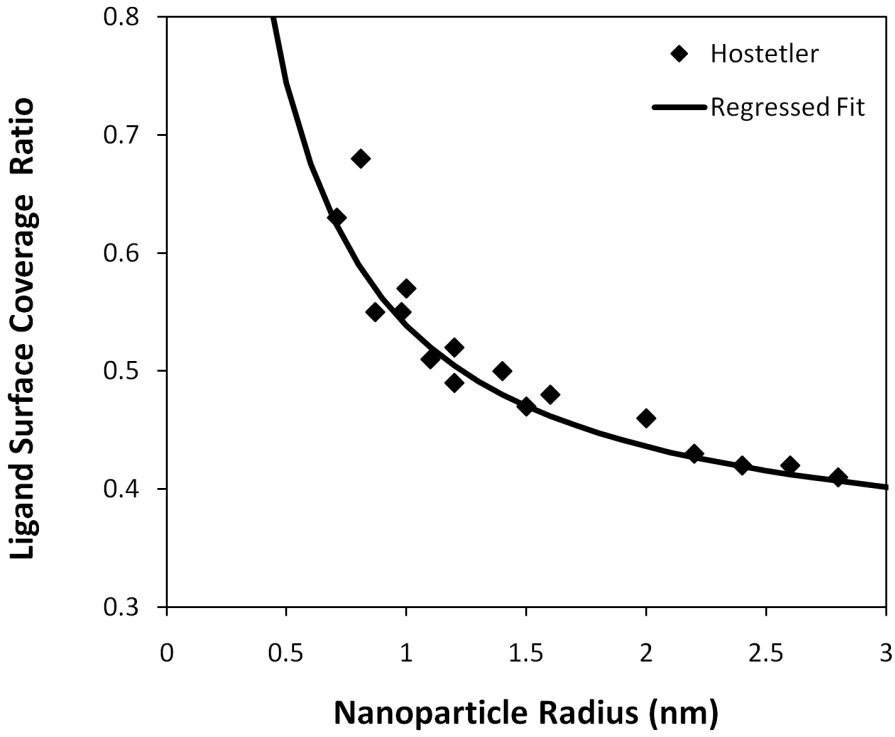

Figure 5.3: Ligand surface coverage ratio as a function of nanoparticle radius for 1-dodecanethiol stabilized-gold (Hostetler *et al.*, 1998) with a regressed fit.

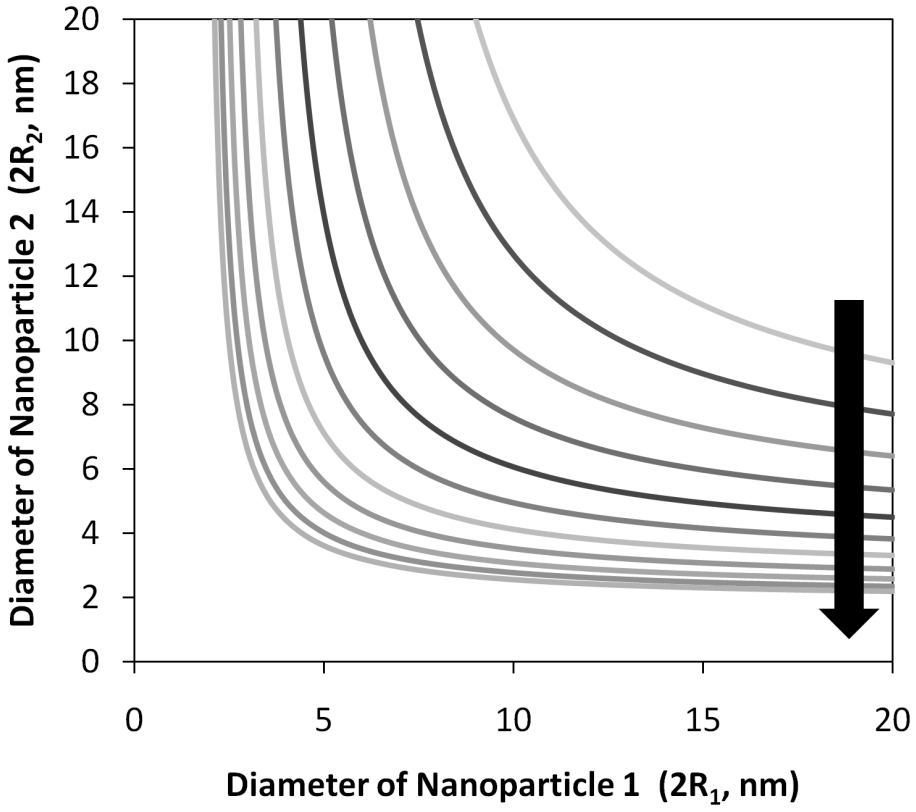

Figure 5.4: Selected threshold nanoparticle sizes for 1-dodecanethiolmstabilized gold nanoparticles dispersed in hexane when precipitated with CO_2 as the antisolvent. Arrow in direction of increasing CO_2 bulk solvent concentration ranging from neat hexane to neat CO_2

5.2.2 Precipitation Probability

Calculation of the threshold nanoparticle sizes indicates which nanoparticle combinations will disperse and which will precipitate however it does not indicate how often those combinations occur. The probability that a specific sized nanoparticle will precipitate is a function of (1) the probability that a nanoparticle of a specific size (R_1) exists and (2) the probability of that nanoparticle interacting with another nanoparticle that is larger than the threshold size (R_2). These two probabilities can be calculated from the probability distribution function ($PDF(R)$) and cumulative distribution function ($CDF(R)$) of a nanoparticle dispersion and, as such, should represent the size distribution obtained experimentally for a given nanoparticle dispersion. For the purposes of this study, nanoparticle distributions will be modeled as normally distributed, as the nanoparticle dispersions synthesized for this study are best fit by a normal distribtion. A distribution that best fits the nanoparticle dispersion should be used whether it be normal, lognormal, etc.

$$PDF(R) = \frac{1}{\sqrt{2\pi\sigma^2}} e^{-\frac{(R-\mu)^2}{2\sigma^2}} \tag{5.16}$$

$$CDF(R) \equiv \int_{-\infty}^{R} PDF(z)\, dz \tag{5.17}$$

where μ and σ are the mean radius and standard deviation, respectively, of a nanoparticle distribution as determined from a sizing study. The probability of a specific sized nanoparticle existing is simply equal to the PDF of that size. The probability that this nanoparticle will interact with a nanoparticle larger than the threshold size is equal to the percentage of total nanoparticles larger than the threshold size ($1 - CDF(R_2)$). As these two events are mutually exclusive, the probabilitiy that a specific sized nanoparticle will precipitate is

$$precip(R_1) = PDF(R_1) \cdot [1 - CDF(R_2)] \tag{5.18}$$

recalling that R_2 is a function of R_1. Similarly, the probability that a specific sized nanoparticle will remain dispersed is

$$disperse\,(R_1) = PDF\,(R_1) \cdot CDF\,(R_2) \tag{5.19}$$

Equations 5.18 and 5.18 reflect that the sample is large enough such that the interactions occur according to the calculated probabilities. However, allowing for a nanoparticle to interact with another nanoparticle only once is not sufficient to approximate equilibrium. For example, if a nanoparticle interacts with another nanoparticle and remains dispersed it can then go on to interact with another nanoparticle that has remained dispersed after its first interaction and that pair of nanoparticles could still precipitate at the current solvent conditions. Therefore this precipitation/dispersion calculation is repeated, tracking both the nanoparticle distributions of the dispersed and precipitated nanoparticles until equilibrium is reached. Upon normalization of the obtained size distributions (according to Equations 5.18 and 5.18), the new probability distribution functions of the precipitated and dispersed nanoparticle distributions are obtained. The average size and standard deviation of the precipitated nanopartion distribution can then be determined by standard statistics.

$$\mu = \int_D x \cdot precip\,(x)\,dx \tag{5.20}$$

$$\sigma = \sqrt{\int_D (x-\mu)^2 \cdot precip\,(x)\,dx} \tag{5.21}$$

5.3 Problem Definition and Solution Methodology

The goal of this model is to calculate the size distributions (including the average size and standard deviation) of the nanoparticles that would precipitate at varying operating conditions. A generalized flowchart explaining the solution methodology is available in Figure 5.5. The complete simulation code is available in Appendix B.

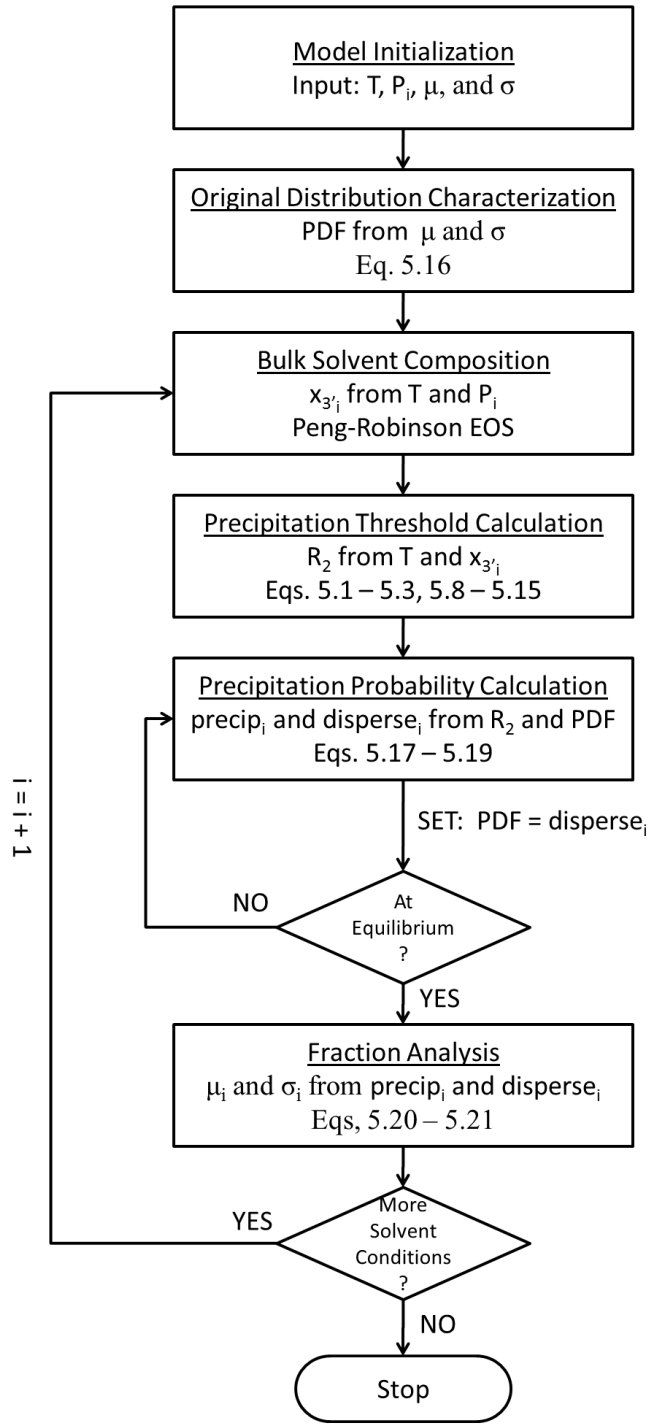

Figure 5.5: Calculation flowchart demonstrating the solution methodology. (ROW 1) Calculation step, (ROW 2) Variables involved, and (ROW 3) Equations.

5.4 Validation and Results

The precipitation of gold nanoparticles can be easily quantified experimentally by tracking the surface plasmon resonance band (SPRB) via UV-vis absorbance spectroscopy (Liu *et al.*, 2007; Schasfoort & Tudos, 2008). Measurement of the intensity of the SPRB at varying levels of applied CO_2 pressure allows for the tracking of the amount of gold nanoparticles that are dispersed (Anand *et al.*, 2005; McLeod *et al.*, 2005b). However, the extinction coefficient of gold nanoparticles varies with the diameter of the nanoparticle (Liu *et al.*, 2007). Compound this with being unable to know precisely the size distribution of nanoparticles that are dispersed *in-situ*, it is rather difficult to translate the intensity of the SPRB into a more meaningful quantity, such as the number of nanoparticles dispersed or the mass of gold dispersed. Even with these shortcomings, tracking of the SPRB of dispersed nanoparticles remains the best experimental measure of the amount of nanoparticles that are dispersed in CO_2-expanded hexane. Figure 5.6 presents a comparison between the SPRB measurements and quantities obtained from this model.

According to the model, the onset of nanoparticle precipitation occurs at lower CO_2 concentrations than that determined from experimental measurements. This could be due to the assumption that solvent conditions are identical inside and outside of the ligand shell. Taking this into account, the model would imply that the solvent inside the ligand shell is hexane-rich compared to the solvent outside the ligand shell which would be consistent with the aliphatic ligand tails being selectively solvated by only the hexane. This would shift the onset of nanoparticle precipitation to larger *bulk* CO_2 solvent concentrations which would better agree with experimental observations. The model predicts that when enough antisolvent has been added such that the solvent can be approximated as pure CO_2, approximately 30% of the nanoparticles (by number) remain dispersed whereas it is known experimentally, via SPRB tracking and visual inspection, that nanoparticle precipitation is completed by the point at which the solvent reaches

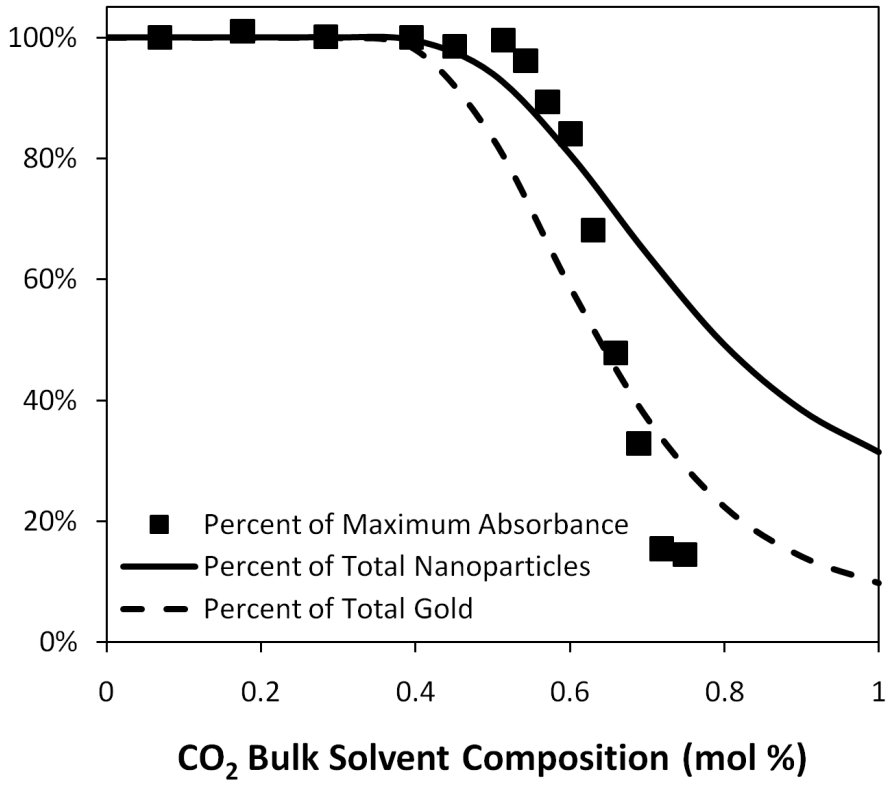

Figure 5.6: Comparison of different methods of quantifying nanoparticle precipitation including: (■) Experimental surface plasmon resonance band tracking by UV-vis absorbance sprectroscopy, (solid line) model predicted percentage of the total number of nanoparticles, and (dashed line) model predicted percentage of the total mass of gold

approximately 80% CO_2. However, it should be noted that the 30% of nanoparticles that are still dispersed comprises only about 10% of the mass of gold that was initially present and that the average diameter of these nanoparticles is only 3.36 nm. Hoestetler and coworkers have demonstrated that the SPRB intensity decreases with size for nanoparticles smaller than approximately 4.4 nm (Hostetler *et al.*, 1998). This implies that even when no SPRB is found, small nanoparticles may still be dispersed and a true measure of the amount of nanoparticles that are dispersed is closer to the model's prediction rather than the measured change in SPRB intensity. Taking these deviations between model and experiment into account, there is a reasonable level of agreement between the two such that a virtual fractionation could be performed.

As mentioned above, it becomes possible to perform virtual fractionations where a nanoparticle dispersion is subjected to a change in solvent conditions, the nanoparticle distributions of both the precipitated and dispersed nanoparticles are calculated and the dispersed nanoparticles further subjected to another change in solvent conditions. This leads to obtaining three fractions of nanoparticles: (1) the nanoparticles that precipitate at the first set of solvent conditions, (2) the nanoparticles that precipitate at the second set of solvent conditions, and (3) the nanoparticles that remain dispersed at the second set of solvent conditions. This mirrors the size-selective fractionation experimental procedure, described in Chapter 2 and elsewhere (Saunders & Roberts, 2009), and allows for a fair comparison between predicted and experimental results. Experimentally, a sample of 4.70 ± 1.20 nm 1-dodecanethiol-stabilized gold nanoparticles dispersed in hexane was subjected (Saunders & Roberts, 2009) to applied CO_2 pressures of 43.4 and 44.8 bar, corresponding to CO_2 bulk solvent compositions of 0.630 and 0.688 mol %, respectively. The results of this size-selective fractionation are displayed as the histograms in Figure 5.7 and statistically in Table 5.2. Calculations were performed as described aboved, starting with an original nanoparticle distribution modeled as a normal distribution with a mean

of 4.70 and standard deviation of 1.20, and results are presented as the curves in Figure 5.7 and statistically in Table 5.2.

There is good agreement qualitatively, as seen in Figure 5.7, between the model predicted results and the experimental observations. It should be noted that there is one adjustable parameter, the extended ligand length (L_{ext}) and it represents the length of the ligand that is solvated. Since this parameter is adjustable, a sensitivity analysis was performed to investigate the effect of varying this parameter from the fully solvated state to lesser degrees of solvation. A small improvement with respect to accuracy (based on the overall coefficient of determination) can by made by reducing the length of the ligand that is solvated in the model from 100% to 60% (from 12.8 Å to 7.7 Å), possibly implying that only a portion of the ligand tails are actually solvated in the experimental system. While this adjustment improves the correlation between predicted values and experimental results for the first and second fractions, this adjustment reduces tthe prediction accuracy for the third fraction. Various methods of adjusting this parameter (e.g., a reduced constant solvation length, variable solvation length for each fraction, estimated solvation length from SANS data, etc.) only show a very slight improvement with respect to overall accuracy, as such, the parameter is left at the assumed value (full solvation, 12.8 Å) for all calculations presented in this chapter.

Nanoparticle probability distribution functions for Fractions 1 and 3 match the shape of the experimental histograms almost perfectly and, statistically, the error between the average diameter experimentally and from the model is only 1.5% and 3.1%, respectively. The model predicted nanoparticle probability distribution function for Fraction 2 is significantly more narrow and has a slightly larger average diameter when compared to the experimental value. The difference is attributed to a limitation of the experimental procedure. After the nanoparticles are precipitated and the still dispersed nanoparticles are moved away from the precipitated nanoparticles, there is a level of film formation that occurs as the liquid/vapor interface traverses the containing vessel. The small amount of

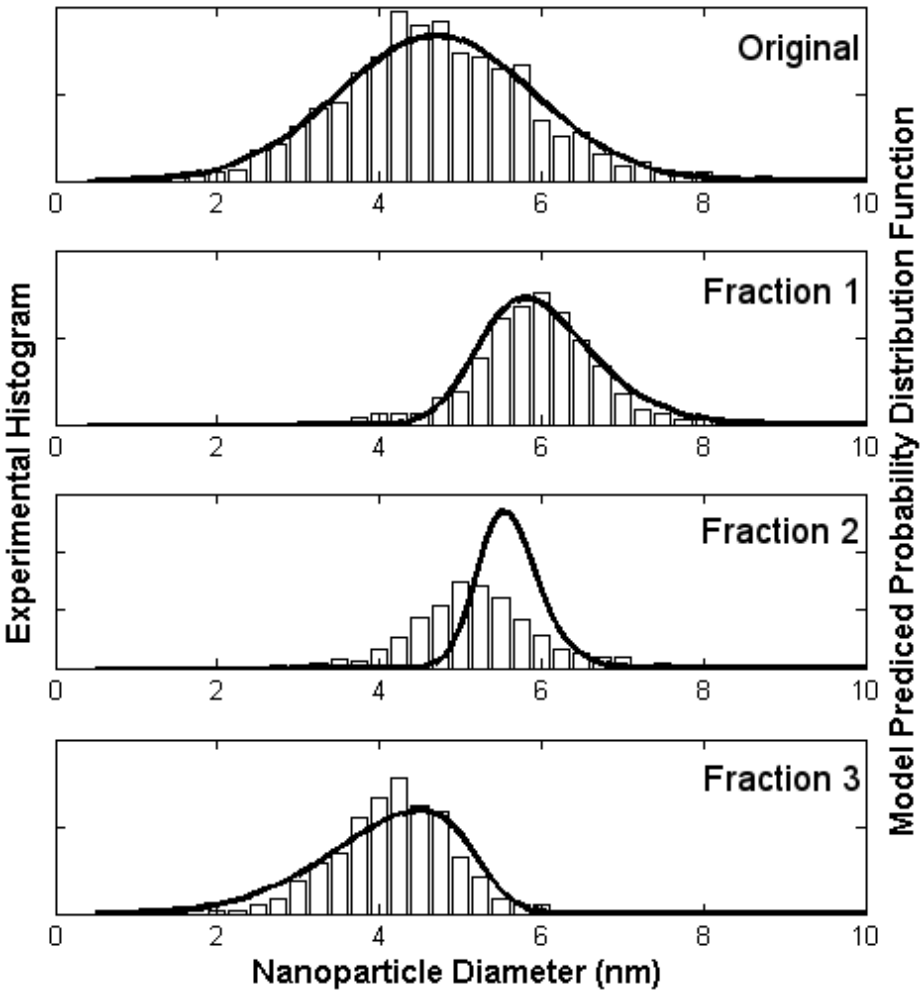

Figure 5.7: Experimental histograms and model predicted PDFs for a size-selective fractionation of dodecanethiol-stabilized gold nanoparticles precipitated at applied CO_2 pressures of 43.4 bar and 44.8 bar.

Applied CO_2 Pressure (Bar)	Bulk CO_2 Conc. (mol%)	Experimental		Model		
		Average (nm)	SDev (nm)	Average (nm)	SDev (nm)	Percent of Original
Original		4.70	1.20	4.70	1.20	
0 - 43.4	0 - 0.630	5.94	0.90	6.03	0.72	27.7
43.4 - 44.8	0.630 - 0.688	5.20	0.92	5.62	0.39	4.7
44.8+	0.688+	4.22	0.78	4.09	0.86	67.6

Table 5.2: Statistical comparison of a size-selective fractionation of 1-dodecanethiol-stabilized gold nanoparticles: experimental results and model prediction

nanoparticles that are deposited during this film formation constitutes a contamination of smaller nanoparticles that should have been removed with the dispersed nanoparticle phase. According to the model prediction, only 4.7% of the original nanoparticles (by number) should have precipitated in the second fraction. Given that this represents such a small fraction of the original distribution, the contamination from the film induced nanoparticle deposition can have significant effect. Note that this effect is not seen in Fraction 1 because the number of nanoparticles that should precipitate (27.7%) is five fold that in Fraction 2 causing the number of nanoparticles that are deposited during the film formation to be negligible. Even with this contaminant, the experimental average diameter of the second fraction is within 10% of the model predicted value.

This effect is seen more significantly when fractionations are performed at lower operating pressures. The experimental results for a size-selective fractionation of 4.56±1.24 nm 1-dodecanethiol stabilized gold nanoparticles dispersed in hexane when subjected to applied CO_2 pressures of 32.7 and 37.9 bar is presented in Figure 5.8 and Table 5.3. This fractionation was performed such that the first fraction of nanoparticles would be a very small percentage of the original dispersion and would likely exagerate the effect of the contamination due to the film formation. As expected, due to the small number of nanoparticles that should precipitate (3.6% according to the model), Fraction 1 is significantly "contaminated" with smaller nanoparticles. In this specific example, the effect of this contamination causes the size-selective fractionation to be ineffective as the second fraction contains, on average, larger nanoparticles than the first fraction. Even with this "worst case scenario," the error between the model predicted average diameter and the experiment findings for Fraction 1 is only 14.9% signifying that this model is extremely accurate across the entire precipititation range.

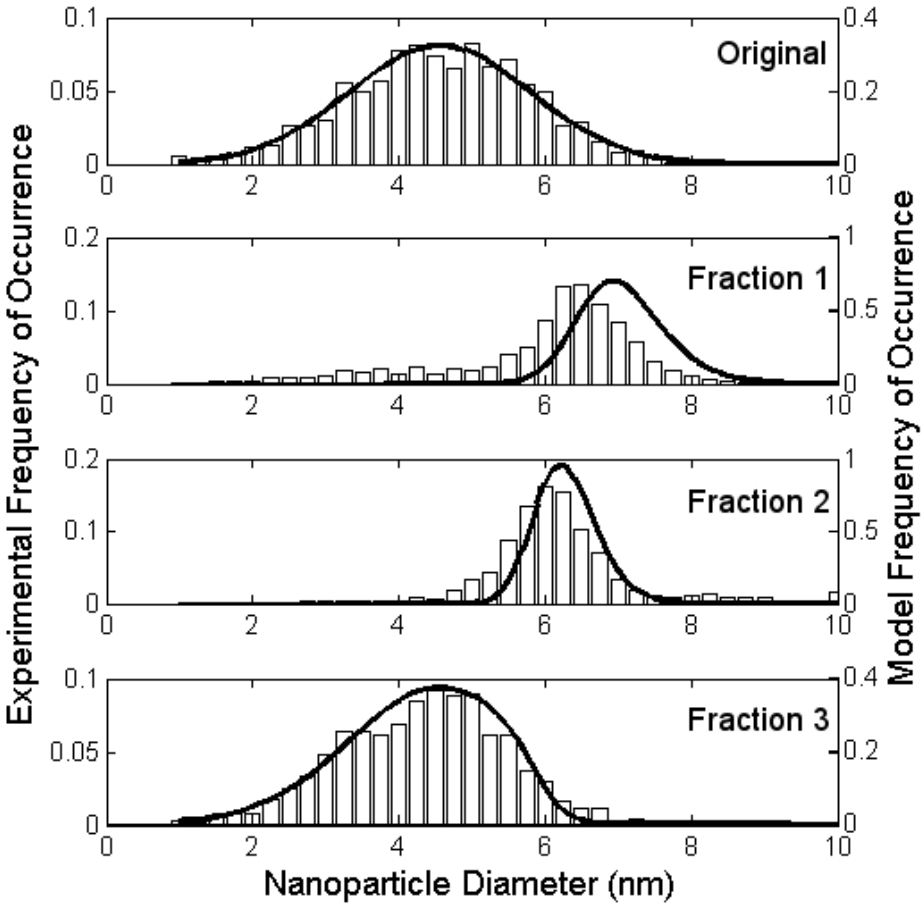

Figure 5.8: Experimental histograms and model PDFs for a size-selective fractionation of dodecanethiol-stabilized gold nanoparticles precipitated at applied CO_2 pressures of 32.7 bar and 37.9 bar.

Applied CO_2 Pressure (Bar)	Bulk CO_2 Conc. (mol%)	Experimental		Model		
		Average (nm)	SDev (nm)	Average (nm)	SDev (nm)	Percent of Original
Original		4.56	1.24	4.56	1.24	
0 - 32.7	0 - 0.482	6.01	1.39	7.06	0.61	3.6
32.7 - 37.9	0.482 - 0.572	6.20	1.18	6.29	0.43	9.2
37.9+	0.572+	4.33	1.12	4.28	1.02	87.2

Table 5.3: Statistical comparison of a size-selective fractionation of 1-dodecanethiol-stabilized gold nanoparticles: experimental results and model prediction

5.5 Stochastic Simulations

As a *real* system has many adjustable variables (size-distribution, ligand surface coverage ratio, local solvent compositions, and ligand shell thickness) all of which can vary, a simple statistical model would not be able to account for all the variability. A stochastic monte carlo simulation could allow the addition of this variability (e.g. varying the ligand surface coverage ratio between nanoparticles of the same size) and preform the calcuations described above. The preliminary work on developing a stochastic simulation is presenting in Appendix C.

5.6 Conclusions

Modeling nanoparticle precipitations as a simple two body interaction through a thermodynamic total interaction energy model is sufficient to accurately predict the size distribution of precipitated and dispersed fractions that could be recovered from a size-selective fractionation process. Like the corresponding experiments, the model has only one manipulative variable (the amount of antisolvent added to the system) and is capable of accurately predicting the average size and size distribution of precipitated and dispersed fractions. This model depends heavily on knowing, *a priori*, the physical nature of the ligand shell (i.e., the ligand shell thickness) with respect to the solvent conditions and, as such, is currently applicable to 1-dodecanethiol-stabilized nanoparticles dispersed in hexane and precipitated with the addition of CO_2, due to the availability of relevant experimental data (White & Kitchens, 2010). Applying this model to a different system (i.e., different stabilizing ligand, solvent, or antisolvent) would require information about the ligand shell which could be determined by small angle neutron scattering (White & Kitchens, 2010) or molecular modeling. Once a general method of determining the ligand shell thickness is perfected, this model could easily be applied to other systems including the traditional liquid-liquid solvent/antisolvent size-selective precipitation process.

Chapter 6

Conclusions and Proposed Future Work

6.1 Conclusions

The overall goal of this work was to advance the state of the art of nanoparticle processing through improvements in experimental techniques and modeling methods. Traditionally, nanoparticle precipitations and fractionations are performed using a solvent-antisolvent technique which is qualitative, time intensive, and produces large quantities of organic solvent waste. Previous work in the Roberts' group has demonstrated a method of size-selectively precipitating and fractionating nanoparticles using CO_2 as an antisolvent to destabilize a nanoparticle dispersion. The gas-expanded liquid precipitation and fractionation technique was only possible at very small scales (~200 μL). Several questions remained after previous studies: (1) can the precipitation and fractionation be performed at scale, (2) are there methods of tuning the range of applied CO_2 pressures over which nanoparticles precipitate and how do those methods affect the quality of the nanoparticles and the efficacy of the fractionations, (3) what physically occurs at the molecular scale that induces this nanoparticle precipitation, and (4) is it possible to predict the average sizes and size-distributions of the recovered nanoparticle fractions?

Chapter 2 attempted to address the possibility of performing the gas-expanded liquid precipitations and fractionations at scale. A new apparatus was developed which was capable of fractionating approximately 20 mL of a nanoparticle dispersion into three fractions while producing zero waste. The apparatus was designed such that it could be scaled to process larger volumes or create more fractions by simply using larger high pressure vessels or more vessels, respectively. The fractions obtained from the scaled apparatus were capable of producing three monodisperse nanoparticle fractions

from an initial polydisperse nanoparticle dispersion. This chapter also address methods of targeting average sizes and size distributions through judicious selections of the operating pressures. Through simple adjustments in the applied CO_2 pressures the recovered nanoparticle fractions could be shifted to larger sizes by decreasing the applied pressures (the opposite is true as well, smaller sizes by increasing the applied pressures). Likewise, by narrowing the pressure differences between each fractionation stage more monodisperse nanoparticle fractions could be recovered. A method of fairly comparing the relative broadness of the size distribution of nanoparticle samples was presented which makes use of a polydispersity index.

Methods of tuning the required applied CO_2 pressures needed to induce nanoparticle precipitation and their effect on the quality of the recovered nanoparticle fractions was addressed in Chapter 3. Through "seeding" a thermodynamically stable nanoparticle dispersion with a poor liquid solvent (acetone) prior to pressurization with CO_2, the required pressure needed to induce nanoparticle precipitation was reduced by approximately 43% as compared to the control (1-dodecanethiol stabilized nanoparicles dispersed in neat n-hexane). This method combined, with the size-selective fractionation technique developed in Chapter 2, was capable of producing three fractions which each demonstrated an extremely high degree of monodispersity. Secondly, by stabilizing the nanoparticle with a shorter ligand (1-hexanethiol vs. 1-dodecanethiol), the pressure needed to induced nanoparticle precipitation could be reduced to the same degree, however there was a drawback that the quality of the nanoparticles is slightly reduced. Due to the shorter ligand stablizing the nanoparticles to a lesser degree, the nanoparticles synthesized with 1-hexanethiol were not as spherical as those stabilized with 1-dodecanethiol. Combining both of these methods to reduce the pressure necessary to induce nanoparticle precipitation with CO_2 ("seeding" with a poor solvent and stabilizing with a shorter ligand), the onset of nanoparticle precipitation could be reduced 85% as compared to the control. However, a second drawback was created such that as the

applied pressure was drastically low, the transport properties of the GXL remained very much liquid-like and the processing times drastically increased. This implies that there is an optimum set of operating conditions (choice of stabilizing ligand, and solvent media) in order to produce the highest quality nanoparticle fractions in the quickest time. An empirical model was also presented which is capable of predicting the average size of the recovered fractions to within 5% of the experimental results.

Through the work performed with Madhu Anand and Seong-Sik Yoo, a simple, fundamental, thermodynamic model to predict the "threshold" nanoparticle size that could be dispersed in a given set of solvent conditions using the total interaction energy between two interacting nanoparticles. This model attempts to balance the inherent van der Waals attractive forces with two repulsive forces: an osmotic repulsive force (originating from the free energy of the solvation of the ligand tails) and an elastic repulsive force (due to the entropic losses created by compressing the ligand tails between the nanoparticle cores). Three phenomenological models were used to describe the physical nature of the solvent-ligand interactions. In the Extended Ligand Length Solvation Model (ELLSM), ligand tails were considered to be fully extended and the entire length of the tail is available to interact with the solvent. In the Condensed Phase Model (CPM), the ligand tails were considered to be condensed on the nanoparticle surface due to poor solvent strength. In the Limited Ligand Length Solvation Model (LLLSM), only a portion of the ligand length was available for solvation. Calculations with each of these models indicated that the two most important parameters for controlling nanoparticle dispersability are the thickness of the ligand shell (the available length of the ligand for solvation) and the ligand surface coverage. The most significant finding of this work was that the ligand shell thickness should decrease with increasing CO_2 concentration which was later confirmed (White & Kitchens, 2010).

Building on the work performed in Chapter 4, Chapter 5 presents a significantly more rigorous fundamental thermodynamic model which attempts to account for the

known collapse of the ligand shell, variable ligand surface coverage, and interactions between differently sized nanoparticles. This chapter presented a new phenomenological model which was consistent with findings of Chapter 4. This phenomenological model assumes a known (White & Kitchens, 2010) ligand shell thickness where the entire length of the ligand is accessible by the solvent. Making the adjustments to the total interaction energy model (to account for this phenomenological model, varying ligand surface coverage and interactions between different sized nanoparticles) the new model was used to predict which size combinations would be able to maintain a dispersion and those that would need to precipitate. Based on this data, using simple statistics that predict the frequency of interactions that would remain dispersed or would precipitate based on the original size distributions, predicted size distributions could be calculated which modeled the fractionation process. This method repeatedly predicted average sizes within 10% of the experimental findings and very good agreement with the standard deviations. This model also shed light on several experimental limitation such as a thin film deposition of nanoparticles that contaminated the precipitated fractions. This simple modeling technique (using statistics to predict the interactions between differently sized nanoparticles) could be used to model other systems if information on the nature of the ligand shell is known.

This work demonstrates several new methods of precipitating and fractionating nanoparticles at significant scales, controllably tuning those processes in order to create high quality monodisperse nanoparticle fractions, and accurately modeling the precipitation and fractionation of nanoparticles in a CO_2 gas-expanded liquid.

6.2 Proposed Future Work

The work presented here opens up new avenues that should be addressed in order to continue the themes of this dissertation: (1) Demonstrate the applicability of the use of gas-expanded liquids to process a wide-range of nanomaterials, (2) demonstrate the

controllability to tune the precipitation process in order to produce extremely high quality nanoparticle samples, (3) utilize the methods developed in this work to investigate new applications and perform fundamental studies and (4) continue modeling efforts in order to have a complete fundamental understanding of nanoparticle dispersion thermodynamics.

6.2.1 Investigation of the Precipitation and Fractionation of Different Nanoparticle Materials

The focus of this work was the investigation of the precipitation, fractionation, and modeling of gold and silver nanoparticles. However, gold and silver are only one material class of nanoparticles. Outside of the nobel metals, other materials such as oxides and semiconductors are seeing a great deal of interest in the medical and electronics industries. Of particular interest is iron oxide (Fe_3O_4 and Fe_2O_3) nanoparticles (Pankhurst *et al.*, 2003; Tartaj *et al.*, 2003; Berry & Curtis, 2010) as MRI contrast agents and as drug delivery agents due to their superparamagnetic properties. Fe_3O_4 has successfully been synthesized in the Roberts' lab by a thermal decomposition co-precipitation method (Tartaj *et al.*, 2003). However, it should be noted that several of the reaction reagents are not FDA approved. As such, modifications need to be made to the synthesis method using FDA approved chemicals such that the product can be ready for bio-applications while maintaining the requirements for the precipitation (organic solvent and aliphatic ligand, e.g. n-heptane and oleic acid). It should be noted that the ligand cannot be a thiol, therefore carboxylic acids have potential, specifically oleic acid. After successful synthesis modifications, precipitations studies and subsequent fractionations could potentially be preformed.

Two additional novel investigations would consist of shape-selective fractionation and a material-selective fractionation. The synthesis of nanorods always produces an amount of non-cylindrical particles. As such, in order to make use of the unique properties of rods, methods of size-selectively fractionating the spheres from the rods is necessary.

The hurdle with regard to shape-selectively fractionations is that nanorods are typically synthesized in aqueous media and are difficult to transfer to an organic. If this can be accomplished then the methods discussed in this work should apply to a shape-selective fractionation. It should be noted that shape-selective fractionations would more than likely be on the basis of surface area rather than diameter. Material-selective fractionations could be used to illustrate the underlying fundementals of the precipitation process. For example, a mixture of similarly sized nanoparticles from two different materials (with signficantly different Hamaker constants) are theoretically capable of being fractionated according to material.

6.2.2 Investigation of the Effect of the Type of Ligand on the Precipitation and Fractionation of Nanoparticles

This work has focused on the investigation of the precipitation, fractionation and modeling of alkanethiol stabilized nanoparticles. Very little investigation into other types of ligands has been explored. Methods of decreasing the slope of the precipitiation curve (Chapter 3) have been shown to increase the controllability of the precipitation and fractionation processing explored in this work. An additional method of altering the precipitation curve trajectory that has not been discussed in this work would be to change the *type* of ligand (i.e. adjusting the ligand backbone). One example of doing this would be to introduce an ether linkage into the backbone as ethers have been demonstrated to have favorable interactions with CO_2 (Hong *et al.*, 2008). This favorable interaction could lead to CO_2 not being as poor of a solvent for the ligand tails. Combine this with a poor liquid solvent, and a short ligand tail, the addition of CO_2 to the dispersion should create a slow precipitation with a high degree of controllability.

6.2.3 Application and Fundamental Studies Using Monodisperse Nanoparticles

With the ability to create large quantities of monodispersed nanoparticles there is an increased opportunity to explore the fundamental size-dependent properties and applications that exploit differences in these properties. A potential manner in which to explore the fundamental properties is with the before mentioned iron oxide superparamagnetic nanoparticles. The iron oxide nanoparticles can be easily synthesized and, potentially, size-selectively fractionated into monodisperse samples. By closely exploring the the variations in magnetic susceptibility and magnetization of the obtained monodisperse iron oxide nanoparticles with respect to the size of the nanoparticles, a new size-selective fractionation technique could potentially be developed. By exploiting those differences, nanoparticles could be size-selectively fractionated by applying different magnetic fields. In addition to exploiting the magnetic properties for a size-selective fractionation, iron oxide nanoparticle applications can be explored, the effect of the different sized (and different properties) on their efficacy as MRI contrast ratio and drug delivery agents. Additional materials that can be explored: the catalytic efficacy of cobalt nanoparticles, the effect on the work of adhesion of MEMS when uniformly coated with differently sized (or distributed) gold nanoparticles (Hurst *et al.*, 2009a; Hurst *et al.*, 2009b).

6.2.4 Intensive Computational Modeling of Nanoparticles in a Stable Dispersion and During Precipitation

The modeling presented in this work (Chapters 4 and 5), represent relatively simlpe models compared to a real system. The model presented in Chapter 4 presents the interaction between two identical nanoparticles while the model in Chapter 5 presents a more complicated model which accounts for interactions between different size nanoparticles (although with the assumption that the ligand shells are identical) along with accounting for the known variations in ligand shell thickness and surface coverage from published works. A real system is significantly more complex: the surface coverage

varying from nanoparticle to nanoparticle of the same size (Saunders & Korgel, 2004), the solvent compositions inside the ligand shell are not identical to those in the bulk solvent (implied in Chapter 5), and the constant Brownian movements of nanoparticles. In an attempt to capture these effects a stochastic simulation could be performed. This simulation would randomly place differently sized nanoparticles throughout a hypothetical box with set solvent properties where the nanoparticle properties (surface coverage, ligand shell thickness, etc.) can be defined according to known deviations. The nanoparticles can then be allowed to move (according to Brownian dynamics or through simple pseudorandom motions) until the total interaction energy of the system is minimized. Over the course of the calculation, any nanoparticle that no longer has the energy to maintain Brownian motion can be "removed" from the simulation (i.e. the nanoparticle precipitates). An anaylsis of the nanoparticles would shed light on the size and size distributions of the precipitated nanoparticles and the dispersed nanoparticles. Other calculations could be performed in order to minimized that amount of experimental data that is used and replaced with fundamental relationships (e.g. the ligand shell thickness data (White & Kitchens, 2010) can be replaced with an equation of state that is capable of calculating the volume fractions of all components or with data from a molecular simulation). This type of model would be a true representation of the known "non-idealities" of a real nanoparticle dispersion. The preliminary development of this stochastic model utilizing a monte carlo method is presented in Appendix C.

References

Adair, J H, Li, T, Kido, T, Havey, K, Moon, J, Mecholsky, J, Morrone, A, Talham, D R, Ludwig, M H, & Wang, L. 1998. Recent developments in the preparation and properties of nanometer-size spherical and platelet-shaped particles and composite particles. *Materials Science & Engineering R-Reports*, **23**(4-5), 139–242.

Adamczyk, Z, & Weronski, P. 1999. Application of the DLVO theory for particle deposition problems. *Advances in Colloid and Interface Science*, **83**(1-3), 137–226.

Alekseeva, A V, Bogatyrev, V A, Khlebtsov, B N, Melnikov, A G, Dykman, L A, & Khlebtsov, N G. 2006. Gold nanorods: Synthesis and optical properties. *Colloid Journal*, **68**(6), 661–678.

Alivisatos, A P. 1996a. Perspectives on the physical chemistry of semiconductor nanocrystals. *Journal of Physical Chemistry*, **100**(31), 13226–13239.

Alivisatos, A P. 1996b. Semiconductor clusters, nanocrystals, and quantum dots. *Science*, **271**(5251), 933–937.

Anand, M, McLeod, M C, Bell, P W, & Roberts, C B. 2005. Tunable solvation effects on the size-selective fractionation of metal nanoparticles in CO_2 gas-expanded solvents. *Journal of Physical Chemistry B*, **109**(48), 22852–22859.

Anand, M, Odom, L A, & Roberts, C B. 2007. Finely controlled size-selective precipitation and separation of CdSe/ZnS semiconductor nanocrystals using CO_2 Gas-Expanded liquids. *Langmuir*, **23**(13), 7338–7343.

Anand, Madhu, You, Seong-Sik, Hurst, Kendall M., Saunders, Steven R., Kitchens, Christopher L., Ashurst, W. Robert, & Roberts, Christopher B. 2008.

Thermodynamic analysis of nanoparticle size selective fractionation using gas-expanded liquids. *Industrial & Engineering Chemistry Research*, **47**(3), 553–559.

Arnaud, I, Abid, J P, Roussel, C, & Girault, H H. 2005. Size-selective separation of gold nanoparticles using isoelectric focusing electrophoresis (IEF). *Chemical Communications*, 787–788.

Beckman, E J. 2004. Supercritical and near-critical CO_2 in green chemical synthesis and processing. *Journal of Supercritical Fluids*, **28**(2-3), 121–191.

Berry, C C, & Curtis, A S G. 2010. Functionalisation of magnetic nanoparticles for applications in biomedicine. *Journal of Physics D: Applied Physics*, **36**(13), R198–R206.

Bethell, D, Brust, M, Schiffrin, D, & Kiely, C. 1996. From monolayers to nanostructured materials: An organic chemist's view of self-assembly. *Journal of Electroanalytical Chemistry*, **409**(1-2), 137–143.

Blasucci, V M, Husain, Z A, Fadhel, A Z, Donaldson, M E, Vyhmeister, E, Pollet, P, Liotta, C L, & Eckert, C A. 2010. Combining homogeneous catalysis with heterogeneous separation using tunable solvent systems. *Journal of Physical Chemistry A*, **114**(11), 3932–3938.

Brochard, F, & de Gennes, P G. 1977. Dynamical scaling for polymers in theta solvents. *Macromolecules*, **10**(5), 1157–1161.

Brown, K R, & Natan, M J. 1998. Hydroxylamine seeding of colloidal Au nanoparticles in solution and on surfaces. *Langmuir*, **14**(4), 726–728.

Brust, M, Walker, M, Bethell, D, Schiffrin, D J, & Whyman, R. 1994. Synthesis of thiol-derivatised gold nanoparticles in a two-phase liquid system. *Journal of the Chemical Society, Chemical Communications*, 801.

Capek, I. 2004. Preparation of metal nanoparticles in water-in-oil (w/o) microemulsions. *Advances in Colloid and Interface Science*, **110**(1-2), 49–74.

Cason, J P, Miller, M E, Thompson, J B, & Roberts, C B. 2001. Solvent Effects on Copper Nanoparticle Growth Behavior in AOT Reverse Micelle Systems. *The Journal of Physical Chemistry B*, **105**(12), 2297–2302.

Cassel, E, Matt, M, Rogalski, M, & Solimando, R. 1997. Phase equilibria modelling for binary systems that contain CO_2. *Fluid Phase Equilibria*, **134**(1-2), 63–75.

Clarke, N Z, Waters, C, Johnson, K A, Satherley, J, & Schiffrin, D J. 2001. Size-dependent solubility of thiol-derivatized gold nanoparticles in supercritical ethane. *Langmuir*, **17**(20), 6048–6050.

Clifford, T. 1999. *Fundamentals of supercritical fluids*. New York: Oxford University Press.

Cooper, A I. 2000. Polymer synthesis and processing using supercritical carbon dioxide. *Journal of Materials Chemistry*, **10**(2), 207–234.

Cushing, B L, Kolesnichenko, V L, & O'Connor, C J. 2004. Recent advances in the liquid-phase syntheses of inorganic nanoparticles. *Chemical Reviews*, **104**(9), 3893–3946.

Daniel, M C, & Astruc, D. 2004. Gold nanoparticles: Assembly, supramolecular chemistry, quantum-size-related properties, and applications toward biology, catalysis, and nanotechnology. *Chemical Reviews*, **104**(1), 293–346.

De Gennes, P. G. 1976a. Dynamics of Entangled Polymer Solutions. I. The Rouse Model. *Macromolecules*, **9**(4), 587–593.

De Gennes, P G. 1976b. Dynamics of Entangled Polymer Solutions II. Inclusion of Hydrodynamic Interactions. *Macromolecules*, **9**(4), 594–598.

Dixon, J D, & Johnston, K P. 1991. Molecular thermodynamics of solubilities in gas antisolvent crystallization. *AIChE Journal*, **37**(10), 1441–1449.

Dubois, L H, & Nuzzo, R G. 1992. Synthesis, Structure, and Properties of Model Organic Surfaces. *Annual Review of Physical Chemistry*, **43**(1), 437–463.

Durr, N J, Larson, T, Smith, D K, Korgel, B A, Sokolov, K, & Ben-Yakar, A. 2007. Two-Photon Luminescence Imaging of Cancer Cells Using Molecularly Targeted Gold Nanorods. *Nano Letters*, **7**(4), 941–945.

Eastoe, J, Hollamby, M J, & Hudson, L. 2006. Recent advances in nanoparticle synthesis with reversed micelles. *Advances in Colloid and Interface Science*, **128**, 5–15.

Eckert, C A, Bush, D, Brown, J S, & Liotta, C L. 2000. Tuning solvents for sustainable technology. *Industrial & Engineering Chemistry Research*, **39**(12), 4615–4621.

Fischer, C H, Weller, H, Katsikas, L, & Henglein, A. 1989. Photochemistry of colloidal semiconductors. 30. HPLC investigation of small CdS particles. *Langmuir*, **5**(2), 429–432.

Foss, C A, Hornyak, G L, Stockert, J A, & Martin, C R. 1994. Template-Synthesized Nanoscopic Gold Particles: Optical Spectra and the Effects of Particle Size and Shape. *The Journal of Physical Chemistry*, **98**(11), 2963–2971.

Frens, G. 1973. Controlled Nucleation for Regulation of Particle-Size in Monodisperse Gold Suspensions. *Nature-Physical Science*, **241**(105), 20–22.

Germain, V, Brioude, A, Ingert, D, & Pileni, M P. 2005. Silver nanodisks: Size selection via centrifugation and optical properties. *Journal of Chemical Physics*, **122**(12), –.

Goulet, Paul J G, & Lennox, R Bruce. 2010. New insights into Brust-Schiffrin metal nanoparticle synthesis. *Journal of the American Chemical Society*, **132**(28), 9582–4.

Granqvist, C G, & Buhrman, R A. 1976. Log-Normal Size Distributions of Ultrafine Metal Particles. *Solid State Communications*, **18**(1), 123–126.

Guerard, D, Janot, R, Ghanbaja, J, & Delcroix, P. 2007. Ball-milling with a fluid: A powerful means for new syntheses. *Journal of Alloys and Compounds*, **434-435**(May), 410–414.

Guzelian, A A, Banin, U, Kadavanich, A V, Peng, X, & Alivisatos, A P. 1996. Colloidal chemical synthesis and characterization of InAs nanocrystal quantum dots. *Applied Physics Letters*, **69**(10), 1432–1434.

Hallett, J P, Kitchens, C L, Hernandez, R, Liotta, C L, & Eckert, C A. 2006. Probing the cybotactic region in gas-expanded liquids (GXLs). *Accounts of Chemical Research*, **39**(8), 531–538.

Hamaker, H C. 1937. The London-van der Waals attraction between spherical particles. *Physica*, **4**(10), 1058–1072.

Hanauer, M, Pierrat, S, Zins, I, Lotz, A, & Sonnichsen, C. 2007. Separation of nanoparticles by gel electrophoresis according to size-and shape. *Nano Letters*, **7**(9), 2881–2885.

Haynes, Christy L., & Van Duyne, Richard P. 2001. Nanosphere Lithography: A Versatile Nanofabrication Tool for Studies of Size-Dependent Nanoparticle Optics. *The Journal of Physical Chemistry B*, **105**(24), 5599–5611.

Herrera, A P, Resto, O, Briano, J G, & Rinaldi, C. 2005. Synthesis and agglomeration of gold nanoparticles in reverse micelles. *Nanotechnology*, S618.

Hiemenz, P C. 1986. *Principles of colloid and surface chemistry*. 2nd edn. New York: M. Dekker.

Hill, E M, Broering, J M, Hallett, J P, Bommarius, A S, Liotta, C L, & Eckert, C A. 2007. Coupling chiral homogeneous biocatalytic reactions with benign heterogeneous separation. *Green Chemistry*, **9**(8), 888–893.

Hong, Lei, Tapriyal, Deepak, & Enick, Robert M. 2008. Phase Behavior of Poly(propylene glycol) Monobutyl Ethers in Dense CO 2. *Journal of Chemical & Engineering Data*, **53**(6), 1342–1345.

Hostetler, M J, Wingate, J E, Zhong, C-J, Harris, J E, Vachet, R W, Clark, M R, Londono, J D, Green, S J, Stokes, J J, Wignall, G D, Glish, G L, Porter, M D, Evans, N D, & Murray, R W. 1998. Alkanethiolate Gold Cluster Molecules with Core Diameters from 1.5 to 5.2 nm: Core and Monolayer Properties as a Function of Core Size. *Langmuir*, **14**(1), 17–30.

Houndonougbo, Yao, Jin, Hong, Rajagopalan, Bhuma, Wong, Kean, Kuczera, Krzysztof, Subramaniam, Bala, & Laird, Brian. 2006. Phase equilibria in carbon dioxide expanded solvents: Experiments and molecular simulations. *The journal of physical chemistry. B*, **110**(26), 13195–202.

Hsieh, H-T, Chin, W-K, & Tan, C-S. 2010. Facile Synthesis of Silver Nanoparticles in CO_2-Expanded Liquids from Silver Isostearate Precursor. *Langmuir*, **26**(12), 10031–10035.

Hsu, J J C, Nagarajan, N, & Robinson, R L. 1985. Equilibrium phase compositions, phase densities, and interfacial tensions for carbon dioxide + hydrocarbon systems. 1. Carbon dioxide + n-butane. *Journal of Chemical & Engineering Data*, **30**(4), 485–491.

Hurst, K, Roberts, C, & Ashurst, W. 2009a. A New Method to Determine Adhesion of Cantilever Beams Using Beam Height Experimental Data. *Tribology Letters*, **35**(1), 9–15.

Hurst, K M, Roberts, C B, & Ashurst, W R. 2009b. A gas-expanded liquid nanoparticle deposition technique for reducing the adhesion of silicon microstructures. *Nanotechnology*, **20**(18), 185303.

Israelachvili, J N. 1985. *Intermolecular and surface forces: with applications to colloidal and biological systems*. London ; Orlando, Fl.: Academic Press.

Jana, N R, Gearheart, L, & Murphy, C J. 2001a. Seed-Mediated Growth Approach for Shape-Controlled Synthesis of Spheroidal and Rod-like Gold Nanoparticles Using a Surfactant Template. *Advanced Materials*, **13**(18), 1389–1393.

Jana, N R, Gearheart, L, & Murphy, C J. 2001b. Wet Chemical Synthesis of High Aspect Ratio Cylindrical Gold Nanorods. *The Journal of Physical Chemistry B*, **105**(19), 4065–4067.

Jana, Nikhil R, Gearheart, Latha, & Murphy, Catherine J. 2001c. Seeding Growth for Size Control of 540 nm Diameter Gold Nanoparticles. *Langmuir*, **17**(22), 6782–6786.

Jessop, P G, & Subramaniam, B. 2007. Gas-expanded liquids. *Chemical Reviews*, **107**(6), 2666–2694.

Jessop, P G, Olmstead, M M, Ablan, C D, Grabenauer, M, Sheppard, D, Eckert, C A, & Liotta, C L. 2002. Carbon dioxide as a solubility "switch" for the reversible dissolution of highly fluorinated complexes and reagents in organic solvents: Application to crystallization. *Inorganic Chemistry*, **41**(13), 3463–3468.

Jimenez, V L, Leopold, M C, Mazzitelli, C, Jorgenson, J W, & Murray, R W. 2003. HPLC of Monolayer-Protected Gold Nanoclusters. *Analytical Chemistry*, **75**(2), 199–206.

Jung, J, & Perrut, M. 2001a. Particle design using supercritical fluids: Literature and patent survey. *The Journal of Supercritical Fluids*, **20**(3), 179–219.

Jung, J, & Perrut, M. 2001b. Particle design using supercritical fluids: Literature and patent survey. *The Journal of Supercritical Fluids*, **20**(3), 179–219.

Khiew, P S, Radiman, S, Huang, N M, Soot Ahmad, Md, & Nadarajah, K. 2005. Preparation and characterization of ZnS nanoparticles synthesized from chitosan laurate micellar solution. *Materials Letters*, **59**(8-9), 989–993.

Kho, Y W, Conrad, D C, & Knutson, B L. 2003. Phase equilibria and thermophysical properties of carbon dioxide-expanded fluorinated solvents. *Fluid Phase Equilibria*, **206**(1-2), 179–193.

Kim, Taehoon, Lee, Kangtaek, Gong, Myoung-seon, & Joo, Sang-Woo. 2005. Control of gold nanoparticle aggregates by manipulation of interparticle interaction. *Langmuir : the ACS journal of surfaces and colloids*, **21**(21), 9524–8.

Kim, Taehoon, Lee, Chang-Ha, Joo, Sang-Woo, & Lee, Kangtaek. 2008. Kinetics of gold nanoparticle aggregation: experiments and modeling. *Journal of Colloid and Interface Science*, **318**(2), 238–243.

Kimijima, K, & Sugimoto, T. 2005. Effects of the water content on the growth rate of AgCl nanoparticles in a reversed micelle system. *Journal of Colloid and Interface Science*, **286**(2), 520–525.

Kiss, L B, Soderlund, J, Niklasson, G A, & Granqvist, C G. 1999. New approach to the origin of lognormal size distributions of nanoparticles. *Nanotechnology*, **10**(1), 25–28.

Kitchens, C L, & Roberts, C B. 2004. Copper nanoparticle synthesis in compressed liquid and supercritical fluid reverse micelle systems. *Industrial & Engineering Chemistry Research*, **43**(19), 6070–6081.

Kitchens, C L, McLeod, M C, & Roberts, C B. 2003. Solvent effects on the growth and steric stabilization of copper metallic nanoparticles in AOT reverse micelle systems. *Journal of Physical Chemistry B*, **107**(41), 11331–11338.

Kitchens, C L, McLeod, M C, & Roberts, C B. 2005. Chloride Ion Effects on Synthesis and Directed Assembly of Copper Nanoparticles in Liquid and Compressed Alkane Microemulsions. *Langmuir*, **21**(11), 5166–5173.

Korgel, B A, Fullam, S, Connolly, S, & Fitzmaurice, D. 1998. Assembly and Self-Organization of Silver Nanocrystal Superlattices: Ordered "Soft Spheres". *The Journal of Physical Chemistry B*, **102**(43), 8379–8388.

Lee, M H, Dobson, P J, & Cantor, B. 1992. Optical properties of evaporated small silver particles. *Thin Solid Films*, **219**(1-2), 199–205.

Lee, M S, Park, S S, Lee, G-D, Ju, C-S, & Hong, S-S. 2005. Synthesis of TiO2 particles by reverse microemulsion method using nonionic surfactants with different hydrophilic and hydrophobic group and their photocatalytic activity. *Catalysis Today*, **101**(3-4), 283–290.

Lide, D R. 1994. *Handbook of Chemistry and Physics, 75th ed.* 75 edn. Boca Raton: CRC.

Lide, D R. 1995. *Handbook of Organic Solvents*. Boca Raton: CRC.

Lide, David R, & Frederikse, H P R. 1995. *CRC handbook of chemistry and physics*. Boca Raton, Fla.; London: CRC.

Lin, X M, Sorensen, C M, & Klabunde, K J. 1999. Ligand-Induced Gold Nanocrystal Superlattice Formation in Colloidal Solution. *Chemistry of Materials*, **11**(2), 198–202.

Link, S, & El-Sayed, M A. 1999. Size and Temperature Dependence of the Plasmon Absorption of Colloidal Gold Nanoparticles. *The Journal of Physical Chemistry B*, **103**(21), 4212–4217.

Lisiecki, I, & Pileni, M P. 1995. Copper Metallic Particles Synthesized "In Situ" in Reverse Micelles: Influence of Various Parameters on the Size of the Particles. *The Journal of Physical Chemistry*, **99**(14), 5077–5082.

Lisiecki, I, & Pileni, M P. 2003. Synthesis of well-defined and low size distribution cobalt nanocrystals: The limited influence of reverse micelles. *Langmuir*, **19**(22), 9486–9489.

Liu, J C, Anand, M, & Roberts, C B. 2006. Synthesis and extraction of beta-D-glucose-stabilized Au nanoparticles processed into low-defect, wide-area thin films and ordered arrays using CO_2-expanded liquids. *Langmuir*, **22**(9), 3964–3971.

Liu, X, Atwater, M, Wang, J, & Huo, Q. 2007. Extinction coefficient of gold nanoparticles with different sizes and different capping ligands. *Colloids and Surfaces B: Biointerfaces*, **58**(1), 3–7.

López-Quintela, M A, Tojo, C, Blanco, M C, García Rio, L, & Leis, J R. 2004. Microemulsion dynamics and reactions in microemulsions. *Current Opinion in Colloid & Interface Science*, **9**(3-4), 264–278.

Lu, J, Lazzaroni, J, Hallett, J P, Bommarius, A S, Liotta, C L, & Eckert, C A. 2004. Tunable solvents for homogeneous catalyst recycle. *Industrial & Engineering Chemistry Research*, **43**(7), 1586–1590.

Maillard, M, Giorgio, S, & Pileni, M-P. 2003. Tuning the Size of Silver Nanodisks with Similar Aspect Ratios: Synthesis and Optical Properties. *The Journal of Physical Chemistry B*, **107**(11), 2466–2470.

Marr, R, & Gamse, T. 2000. Use of supercritical fluids for different processes including new developments: A review. *Chemical Engineering and Processing*, **39**(1), 19–28.

Martin, C R. 1994. Nanomaterials: A Membrane-Based Synthetic Approach. *Science*, **266**(5193), 1961–1966.

Martin, C R. 1996. Membrane-Based Synthesis of Nanomaterials. *Chemistry of Materials*, **8**(8), 1739–1746.

Maxey, N B. 2006. *Transport and Phase Transfer Catalysis in Gas-Expanded Liquids*. Dissertation, Georgia Institute of Technology.

McHugh, M A, & Krukonis, V J. 1994. *Supercritical fluid extraction : principles and practice*. 2nd edn. Boston: Butterworth-Heinemann.

McLeod, M C, Kitchens, C L, & Roberts, C B. 2005a. CO_2-expanded liquid deposition of ligand-stabilized nanoparticles as uniform, wide-area nanoparticle films. *Langmuir*, **21**(6), 2414–2418.

McLeod, M C, Anand, M, Kitchens, C L, & Roberts, C B. 2005b. Precise and rapid size selection and targeted deposition of nanoparticle populations using CO_2 gas expanded liquids. *Nano Letters*, **5**(3), 461–465.

Metropolis, N, Rosenbluth, A W, Rosenbluth, M N, Teller, A H, & Teller, E. 1953. Equation of State Calculations by Fast Computing Machines. *Journal of Chemical Physics*, **21**(6), 1087–1092.

Mie, G. 1908. Beiträge zur Optik trüber Medien, speziell kolloidaler Metallösungen. *Annalen der Physik*, **330**(3), 377–445.

Murday, J S. 2002. The Coming Revolution: Science and Technology of Nanoscale Structures. *The AMPTIAC Newsletter*, **6**(1), 5–10.

Murray, C B, Kagan, C R, & Bawendi, M G. 2000. Synthesis and Characterization of Monodisperse Nanocrystals and Close-Packed Nanocrystal Assemblies. *Annual Review of Materials Science*, **30**(1), 545–610.

Murray, C B, Norris, D J, & Bawendi, M G. 2002. Synthesis and characterization of nearly monodisperse CdE (E = sulfur, selenium, tellurium) semiconductor nanocrystallites. *Journal of the American Chemical Society*, **115**(19), 8706–8715.

Nikoobakht, B, & El-Sayed, M A. 2003. Preparation and Growth Mechanism of Gold Nanorods (NRs) Using Seed-Mediated Growth Method. *Chemistry of Materials*, **15**(10), 1957–1962.

NNI. 2005. *The National Nanotechnology Initiative: Research and Development Leading to a Revolution in Technology and Industry*.

NNI. 2008. *National Nanotechnology Initiative: FY 2008 Budget & Highlights*.

NNI. 2009. *National Nanotechnology Initiative: FY 2009 Budget & Highlights*.

Ohara, P C, Leff, D V, Heath, J R, & Gelbart, W M. 1995. Crystallization of Opals from Polydisperse Nanoparticles. *Physical Review Letters*, **75**(19), 3466.

Palakodaty, S, & York, P. 1999. Phase Behavioral Effects on Particle Formation Processes Using Supercritical Fluids. *Pharmaceutical Research*, **16**(7), 976–985.

Pankhurst, QA, Connolly, J, Jones, SK, & Dobson, J. 2003. Applications of magnetic nanoparticles in biomedicine. *Journal of Physics D: Applied Physics*, **36**(13), R167–R181.

Parsegian, V. 1981. Spectroscopic parameters for computation of van der waals forces. *Journal of Colloid and Interface Science*, **81**(1), 285–289.

Peng, D, & Robinson, D B. 1976. NEW 2-CONSTANT EQUATION OF STATE. *Industrial & Engineering Chemistry Fundamentals*, **15**(1), 59–64.

Perez-Juste, J, Pastoriza-Santos, I, Liz-Marzan, L M, & Mulvaney, P. 2005. Gold nanorods: Synthesis, characterization and applications. *Coordination Chemistry Reviews*, **249**(17-18), 1870–1901.

Petit, C, & Pileni, M P. 1988. Synthesis of cadmium sulfide in situ in reverse micelles and in hydrocarbon gels. *The Journal of Physical Chemistry*, **92**(8), 2282–2286.

Petit, C, Lixon, P, & Pileni, M P. 1993. In-Situ Synthesis of Silver Nanocluster in AOT Reverse Micelles. *Journal of Physical Chemistry*, **97**(49), 12974–12983.

Petit, C, Taleb, A, & Pileni, M P. 1999. Cobalt nanosized particles organized in a 2D superlattice: Synthesis, characterization, and magnetic properties. *Journal of Physical Chemistry B*, **103**(11), 1805–1810.

Poole, C P, & Owens, F J. 2003. *Introduction to nanotechnology*. Hoboken, NJ: J. Wiley.

Porter, M D, Bright, T B, Allara, D L, & Chidsey, C E D. 1987. Spontaneously Organized Molecular Assemblies 4. Structural Characterization of Normal-Alkyl Thiol Monolayers on Gold by Optical Ellipsometry, Infrared-Spectroscopy, and Electrochemistry. *Journal of the American Chemical Society*, **109**(12), 3559–3568.

Prasad, B L V, Stoeva, S I, Sorensen, C M, & Klabunde, K J. 2003. Digestive-ripening agents for gold nanoparticles: Alternatives to thiols. *Chemistry of Materials*, **15**(4), 935–942.

Rauscher, F, Veit, P, & Sundmacher, K. 2005. Analysis of a technical-grade w/o-microemulsion and its application for the precipitation of calcium carbonate nanoparticles. *Colloids and Surfaces A: Physicochemical and Engineering Aspects*, **254**(1-3), 183–191.

Reverchon, E. 1999. Supercritical antisolvent precipitation of micro- and nano-particles. *The Journal of Supercritical Fluids*, **15**(1), 1–21.

Romero-Cano, M S, Puertas, A M, & Nieves, F J De Las. 2000. Colloidal aggregation under steric interactions: Simulation and experiments. *The Journal of Chemical Physics*, **112**(19), 8654–8659.

Saiwan, C, Krathong, S, Anukulprasert, T, & Rear, E A. 2004. Nano-Titanium Dioxide Synthesis in AOT Microemulsion System with Salinity Scan. *Journal of Chemical Engineering of Japan*, **37**(2), 279–285.

Sassiat, P R, Mourier, P, Caude, M H, & Rosset, R H. 1987. Measurement of diffusion coefficients in supercritical carbon dioxide and correlation with the equation of Wilke and Chang. *Analytical Chemistry*, **59**(8), 1164–1170.

Sato, Tatsuo. 1993. Stability of dispersion. *The Journal of Coatings Technology*, **v65**(825), 113.

Saunders, A E, & Korgel, B A. 2004. Second Virial Coefficient Measurements of Dilute Gold Nanocrystal Dispersions Using Small-Angle X-ray Scattering. *The Journal of Physical Chemistry B*, **108**(43), 16732–16738.

Saunders, S R, & Roberts, C B. 2009. Size-selective fractionation of nanoparticles at an application scale using CO_2 gas-expanded liquids. *Nanotechnology*, **20**(47), 475605.

Saunders, S R, & Roberts, C B. 2011. Modeling the Precipitation of Polydisperse Nanoparticles Using a Total Interaction Energy Model. *Journal of Physical Chemistry C (submitted)*.

Schapotschnikow, P, Pool, R, & Vlugt, T J H. 2008. Molecular simulations of interacting nanocrystals. *Nano Letters*, **8**(9), 2930–2934.

Schasfoort, R B M, & Tudos, Anna J. 2008. *Handbook of surface plasmon resonance*. Cambridge, UK: RSC Pub.

Shah, P S, Husain, S, Johnston, K P, & Korgel, B A. 2002a. Role of steric stabilization on the arrested growth of silver nanocrystals in supercritical carbon dioxide. *Journal of Physical Chemistry B*, **106**(47), 12178–12185.

Shah, P S, Holmes, J D, Johnston, K P, & Korgel, B A. 2002b. Size-selective dispersion of dodecanethiol-coated nanocrystals in liquid and supercritical ethane by density tuning. *Journal of Physical Chemistry B*, **106**(10), 2545–2551.

Shah, P S, Hanrath, T, Johnston, K P, & Korgel, B A. 2004. Nanocrystal and nanowire synthesis and dispersibility in supercritical fluids. *Journal of Physical Chemistry B*, **108**(28), 9574–9587.

Shi, J, & Verweij, H. 2005. Synthesis and Purification of Oxide Nanoparticle Dispersions by Modified Emulsion Precipitation. *Langmuir*, **21**(12), 5570–5575.

Shiang, J J, Kadavanich, A V, Grubbs, R K, & Alivisatos, A P. 1996. Symmetry of annealed Wurtzite CdSe nanocrystals: Assignment to the C-3v point group (vol 99, pg 17418, 1995). *Journal of Physical Chemistry*, **100**(32), 13886.

Siegel, R W, Hu, E, & Roco, M C. 1998. *Nanostructure Science and Technology: A Worldwide Study*.

Sigman, M B, Saunders, A E, & Korgel, B A. 2004. Metal nanocrystal superlattice nucleation and growth. *Langmuir*, **20**(3), 978–983.

Smith, D K, & Korgel, B A. 2008. The importance of the CTAB surfactant on the colloidal seed-mediated synthesis of gold nanorods. *Langmuir*, **24**(3), 644–649.

Spirin, M G, Brichkin, S B, & Razumov, V F. 2005. Synthesis and Stabilization of Gold Nanoparticles in Reverse Micelles of Aerosol OT and Triton X-100. *Colloid Journal*, **67**(4), 485–490.

Stanton, L A, Dehghani, F, & Foster, N R. 2002. Improving Drug Delivery Using Polymers. *Australian Journal of Chemistry*, **55**(7), 443–447.

Stavis, S M, Strychalski, E A, & Gaitan, M. 2009. Nanofluidic structures with complex three-dimensional surfaces. *Nanotechnology*, 165302.

Stoeva, S, Klabunde, K J, Sorensen, C M, & Dragieva, I. 2002. Gram-Scale Synthesis of Monodisperse Gold Colloids by the Solvated Metal Atom Dispersion Method

and Digestive Ripening and Their Organization into Two- and Three-Dimensional Structures. *Journal of the American Chemical Society*, **124**(10), 2305–2311.

Subramaniam, B, Rajewski, R A, & Snavely, K. 1997. Pharmaceutical processing with supercritical carbon dioxide. *Journal of Pharmaceutical Sciences*, **86**(8), 885–890.

Sun, Y D, Shekunov, B Y, & York, P. 2003. Refractive index of supercritical CO2-ethanol solvents. *Chemical Engineering Communications*, **190**(1), 1–14.

Sweeney, S F, Woehrle, G H, & Hutchison, J E. 2006. Rapid purification and size separation of gold nanoparticles via diafiltration. *Journal of the American Chemical Society*, **128**(10), 3190–3197.

Tan, E K, Tan, Y, Chai, A, Tan, C, Shen, H, Lum, S Y, Fook-Cheong, S M C, Teoh, M L, Yih, Y, Wong, M C, & Zhao, Y. 2003. Dopamine D2 receptor TaqIA and TaqIB polymorphisms in Parkinson's disease. *Movement Disorders*, **18**(5), 593–595.

Tan, H S, & Borsadia, S. 2001. Particle formation using supercritical fluids: pharmaceutical applications. *Expert Opinion on Therapeutic Patents*, **11**(5), 861–872.

Tartaj, Pedro, Morales, Mar A Del Puerto, Veintemillas-Verdaguer, Sabino, Gonz Lez-Carre O, Teresita, & Serna, Carlos J. 2003. The preparation of magnetic nanoparticles for applications in biomedicine. *Journal of Physics D: Applied Physics*, **36**(13), R182–R197.

Thomas, P J, Saravanan, P, Kulkarni, G U, & Rao, C N R. 2002. Arrays of magnetic nanoparticles capped with alkylamines. *Pramana-Journal of Physics*, **58**(2), 371–383.

Tom, J W, & Debenedetti, P G. 1991. Particle formation with supercritical fluids: A review. *Journal of Aerosol Science*, **22**(5), 555–584.

Turkevich, J, Garton, G, & Stevenson, P C. 1954. The color of colloidal gold. *Journal of Colloid Science*, **9**(Supplement 1), 26–35.

Ullmann, Marc, Friedlander, Sheldon K., & Schmidt-Ott, Andreas. 2002. *Nanoparticle Formation by Laser Ablation*.

Vesovic, V, Wakeham, W A, Olchowy, G A, Sengers, J V, Watson, J T R, & Millat, J. 1990. The Transport-Properties of Carbon-Dioxide. *Journal of Physical and Chemical Reference Data*, **19**(3), 763–808.

Vincent, B, Luckham, P F, & Waite, F A. 1980. The effect of free polymer on the stability of sterically stabilized dispersions. *Journal of Colloid and Interface Science*, **73**(2), 508–521.

Vincent, B, Edwards, J, Emmett, S, & Jones, A. 1986. Depletion flocculation in dispersions of sterically-stabilised particles ("soft spheres"). *Colloids and Surfaces*, **18**(2-4), 261–281.

Wei, G-T, Liu, F-K, & Wang, C R C. 1999. Shape Separation of Nanometer Gold Particles by Size-Exclusion Chromatography. *Analytical Chemistry*, **71**(11), 2085–2091.

White, G V, & Kitchens, C L. 2010. Small-Angle Neutron Scattering of Silver Nanoparticles in Gas-Expanded Hexane. *The Journal of Physical Chemistry C*, **114**(39), 16285–16291.

Wilcoxon, J P, Martin, J E, Parsapour, F, Wiedenman, B, & Kelley, D F. 1998. Photoluminescence from nanosize gold clusters. *The Journal of Chemical Physics*, **108**(21), 9137–9143.

Williams, D P, & Satherley, J. 2009. Size-Selective Separation of Polydisperse Gold Nanoparticles in Supercritical Ethane. *Langmuir*, **25**(6), 3743.

Wyatt, V T, Bush, D, Lu, J, Hallett, J P, Liotta, C L, & Eckert, C A. 2005. Determination of solvatochromic solvent parameters for the characterization of gas-expanded liquids. *The Journal of Supercritical Fluids*, **36**(1), 16–22.

Xing, S, Chu, Y, Sui, X, & Wu, Z. 2005. Synthesis and characterization of polyaniline in CTAB/hexanol/water reversed micelle. *Journal of Materials Science*, **40**(1), 215–218.

Yamaki, Mariko, Higo, Junichi, & Nagayama, Kuniaki. 1995. Size-Dependent Separation of Colloidal Particles In Two-Dimensional Convective Self-Assembly. *Langmuir*, **11**(8), 2975–2978.

Ye, X, & Wai, C M. 2003. Making Nanomaterials in Supercritical Fluids: A Review. *Journal of Chemical Education*, **80**(2), 198.

Yeo, S-D, & Kiran, E. 2005. Formation of polymer particles with supercritical fluids: A review. *The Journal of Supercritical Fluids*, **34**(3), 287–308.

Yonezawa, T, & Kunitake, T. 1999. Practical preparation of anionic mercapto ligand-stabilized gold nanoparticles and their immobilization. *Colloids and Surfaces a-Physicochemical and Engineering Aspects*, **149**(1-3), 193–199.

Yonezawa, T, Onoue, S, & Kimizuka, N. 2000. Preparation of highly positively charged silver nanoballs and their stability. *Langmuir*, **16**(12), 5218–5220.

Yu, Y-Y, Chang, S-S, Lee, C-L, & Wang, C R C. 1997. Gold Nanorods: Electrochemical Synthesis and Optical Properties. *The Journal of Physical Chemistry B*, **101**(34), 6661–6664.

Zhang, J, Han, B, Liu, J, Zhang, X, Liu, Z, & He, J. 2001. A new method to recover the nanoparticles from reverse micelles: recovery of ZnS nanoparticles synthesized in reverse micelles by compressed CO2. *Chemical Communications*, 2724–2725.

Appendices

Appendix A

Empirical Model

Included in the following pages are an example of the MathCAD calculation sheets developed for and discussed in detail in Chapter 3. This example demonstrates a calculation of the average fraction diameters of 1-dodecanethiol stabilized gold nanoparticles dispersed in neat hexane fractionation at applied CO_2 pressures of 36.2 and 37.6 bar (525 and 545 psi, respectively).

Particle Size Distribution

Hidden in the above area is data for the particle distribution. Array data for: diameters, counts, and frequency.

$\mu_A := 5.24$ $\mu_{LN} := \ln(5.25)$ data from sizing sheet

$sd_A := 1.22$ $sd_{LN} := \ln(1.33)$

$distN(x) := dnorm(x, \mu_A, sd_A)$ Normal distribution based on sizing statistics

$$SS_{tot} := \sum_{i=0}^{20} \left(frequencynorm_i - mean(frequencynorm)\right)^2$$

$$SS_{err} := \sum_{i=0}^{20} \left(frequencynorm_i - dnorm\left(\frac{i}{2}, \mu_A, sd_A\right)\right)^2$$

$$\left[R^2\right] := 1 - \frac{SS_{err}}{SS_{tot}}$$

$\left[R^2\right] = 0.888$ R^2 value for normal distribution based on sizing statistics

$distLN(x) := dlnorm(x, \mu_{LN}, sd_{LN})$ Lognormal distribution based on sizing statistics

$distfitA(x) := dnorm(x, \mu_{LN}, sd_{LN})$

$$SS_{err} := \sum_{i=0}^{20} \left(frequencynorm_i - dlnorm\left(\frac{i}{2}, \mu_{LN}, sd_{LN}\right)\right)^2$$

$$\left[R^2\right] := 1 - \frac{SS_{err}}{SS_{tot}}$$

$\left[R^2\right] = 0.743$ R^2 value for normal distribution based on sizing statistics

cubic spline fit to the diameter / frequency data

$$distspline(x) := interp(cspline(diameter, frequency), diameter, frequency, x)$$

$$distspline(x) := \frac{1}{\int_0^{10} distspline(y)\,dy} \cdot distspline(x)$$

$$SS_{err} := \sum_{i=0}^{20} \left(frequencynorm_i - distspline\left(\frac{i}{2}\right) \right)^2$$

$$\left[R^2\right] := 1 - \frac{SS_{err}}{SS_{tot}}$$

$$\left[R^2\right] = 1$$

R^2 value for a cubic spline fit

regressed data fits to the diameter / frequency data

$$\mu_{fitAg} := 6 \qquad \mu_{fitLNg} := \ln(5)$$

$$sd_{fitAg} := 1 \qquad sd_{fitLNg} := \ln(1.2)$$

Given

$$\sum_{i=0}^{20} \left(frequencynorm_i - dnorm\left(\frac{i}{2}, \mu_{fitAg}, sd_{fitAg}\right) \right)^2 = 0$$

$$\begin{pmatrix} \mu_{fitA} \\ sd_{fitA} \end{pmatrix} := Minerr\left(\mu_{fitAg}, sd_{fitAg}\right)$$

$$\begin{pmatrix} \mu_{fitA} \\ sd_{fitA} \end{pmatrix} = \begin{pmatrix} 5.552 \\ 0.978 \end{pmatrix}$$

Normal distribution based on frequency data

$$distfitN(x) := dnorm\left(x, \mu_{fitA}, sd_{fitA}\right)$$

$$SS_{err} := \sum_{i=0}^{20} \left(frequencynorm_i - dnorm\left(\frac{i}{2}, \mu_{fitA}, sd_{fitA}\right)\right)^2$$

$$\left[R^2\right] := 1 - \frac{SS_{err}}{SS_{tot}}$$

$$\left[R^2\right] = 0.981$$

R^2 value for normal distribution based on frequency data

Given

$$\sum_{i=0}^{20} \left(frequencynorm_i - dlnorm\left(\frac{i}{2}, \mu_{fitLNg}, sd_{fitLNg}\right)\right)^2 = 0$$

$$\begin{pmatrix} \mu_{fitLN} \\ sd_{fitLN} \end{pmatrix} := Minerr\left(\mu_{fitLNg}, sd_{fitLNg}\right)$$

$$\begin{pmatrix} \mu_{fitLN} \\ sd_{fitLN} \end{pmatrix} = \begin{pmatrix} 1.726 \\ 0.176 \end{pmatrix}$$

Lognormal fit based on frequency data

$$distfitLN(x) := dlnorm\left(x, \mu_{fitLN}, sd_{fitLN}\right)$$

$$SS_{err} := \sum_{i=0}^{20} \left(frequencynorm_i - dlnorm\left(\frac{i}{2}, \mu_{fitLN}, sd_{fitLN}\right)\right)^2$$

$$\left[R^2\right] := 1 - \frac{SS_{err}}{SS_{tot}}$$

$$\left[R^2\right] = 0.962$$

R^2 value for lognormal distribution based on frequency data

Summary of Particle Size Distribution Fits

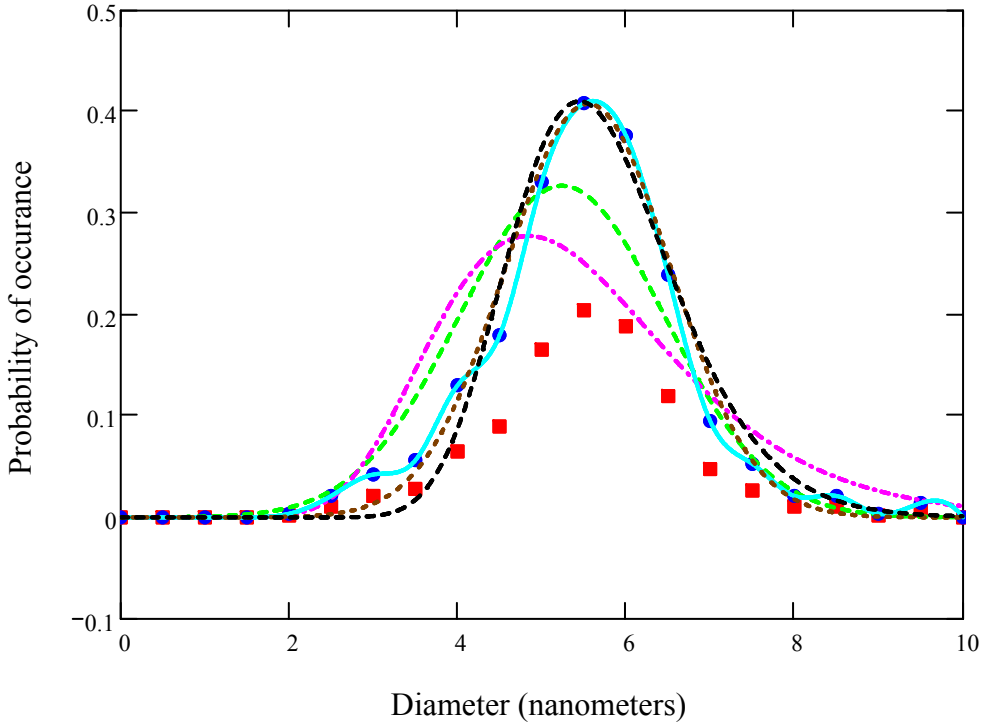

Frequency Data
Normalized Frequency Data
Normal Distribution (sizing statistics)
Lognormal Distribution (sizing statistics)
Cubic spline fit (frequency data)
Normal Distribution (frequency data)
Lognormal Distribution (frequency data)

Distribution	R^2
Normal (sizing)	0.888
Lognormal (sizing)	0.743
Cubic Spline (frequency)	1
Normal (frequency)	0.981
Lognormal (frequency)	0.962

dist(x) := distN(x) selects fit to use

UV extinction curve

hidden above is the Pressure / Absorbance Curve

cubic spline fit

$$UVfitspline(x) := interp(cspline(Pressure, Absorbance), Pressure, Absorbance, x)$$

$$SS_{tot} := \sum_{i=0}^{15} \left(Absorbance_i - mean(Absorbance)\right)^2$$

$$SS_{err} := \sum_{i=0}^{15} \left(Absorbance_i - UVfitspline(i \cdot 50)\right)^2$$

$$\left[R^2\right] := 1 - \frac{SS_{err}}{SS_{tot}}$$

$$\left[R^2\right] = 1$$

R^2 value for cubic spline fit to Pressure / Absorbance data

Regressed fits

$$\mu_{fitUVg} := 500$$

$$sd_{fitUVg} := 100$$

Given

$$\sum_{i=0}^{15} \left[Absorbance_i - \left(1 - pnorm\left(i \cdot 50, \mu_{fitUVg}, sd_{fitUVg}\right)\right)\right]^2 = 0$$

$$\begin{pmatrix} \mu_{fitUV} \\ sd_{fitUV} \end{pmatrix} := Minerr\left(\mu_{fitUVg}, sd_{fitUVg}\right)$$

$$\begin{pmatrix} \mu_{fitUV} \\ sd_{fitUV} \end{pmatrix} = \begin{pmatrix} 513.81 \\ 84.178 \end{pmatrix}$$

$$UVfitN(x) := 1 - pnorm\left(x, \mu_{fitUV}, sd_{fitUV}\right)$$

Normal CDF fit to Pressure / Absorbance data

$$SS_{err} := \sum_{i=0}^{15} \left(Absorbance_i - UVfitN(i \cdot 50)\right)^2$$

$$\left[R^2\right] := 1 - \frac{SS_{err}}{SS_{tot}}$$

$$\left[R^2\right] = 0.999$$

R^2 value for normal CDF fit to Pressure / Absorbance data

Given

$$\sum_{i=0}^{15} \left[Absorbance_i - \left(1 - plnorm\left(i \cdot 50, \mu_{fitUVg}, sd_{fitUVg}\right)\right)\right]^2 = 0$$

$$\begin{pmatrix} \mu_{fitUV} \\ sd_{fitUV} \end{pmatrix} := Minerr\left(\mu_{fitUVg}, sd_{fitUVg}\right)$$

$$\begin{pmatrix} \mu_{fitUV} \\ sd_{fitUV} \end{pmatrix} = \begin{pmatrix} 6.236 \\ 0.162 \end{pmatrix}$$

$$UVfitLN(x) := 1 - plnorm\left(x, \mu_{fitUV}, sd_{fitUV}\right)$$

Lognormal CDF fit to Pressure / Absorbance data

$$SS_{err} := \sum_{i=0}^{15} \left(Absorbance_i - UVfitLN(i \cdot 50)\right)^2$$

$$\left[R^2\right] := 1 - \frac{SS_{err}}{SS_{tot}}$$

$$\left[R^2\right] = 0.997$$

R^2 value for lognormal CDF fit to Pressure / Absorbance data

Summary of UV Extinction fits

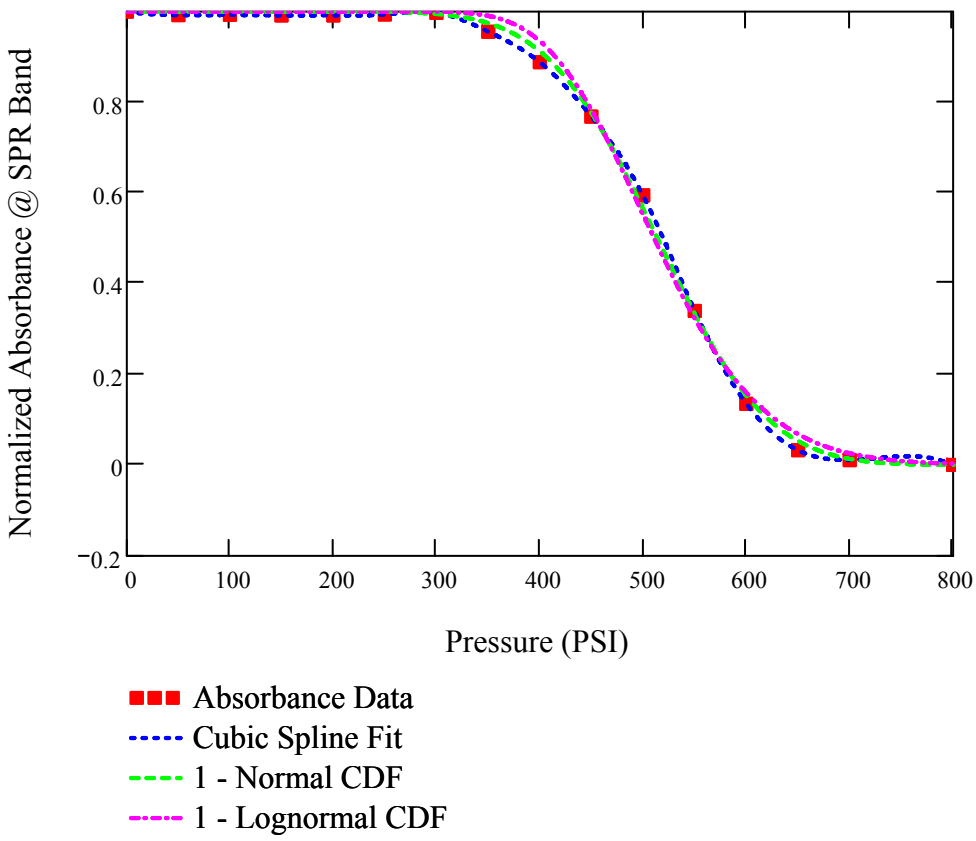

Fit Choice	R^2 Value
Cubic Spline	1
1 - Normal CDF	0.999
1 - Lognormal CDF	0.997

UVfit(x) := UVfitN(x) selects which fit to use

Extinction coefficient

$k := 3.36$

From El-Sayed paper on Mie Theory, validated by Liu and Huo

$a := 8.1$

$\varepsilon(D) := \exp(k \cdot \ln(D) + a)$

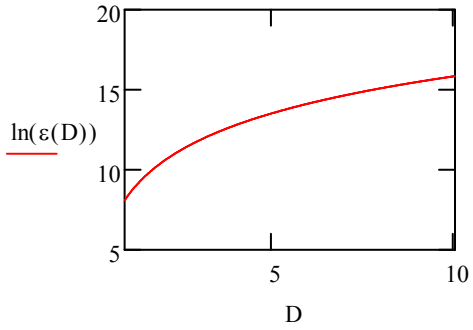

$$\varepsilon_{ave}(x,y) := \int_x^y \varepsilon(z) \cdot \left(\frac{\mathrm{dist}(z)}{\int_x^y \mathrm{dist}(w)\, dw} \right) dz$$

Average extinction coefficient from a sample in the distribution from x nm to y nm

$\varepsilon_{ave}(x) := \varepsilon_{ave}(0,x)$

Concentration from distribution

$\rho := 19.3 \quad M := 197 \quad N_a := 6.023 \cdot 10^{23}$

$$N(D) := \frac{\pi}{6} \cdot \frac{\rho \cdot N_a \cdot \left(D \cdot 10^{-7}\right)^3}{M}$$

Moles of gold per particle as a function of particle diameter

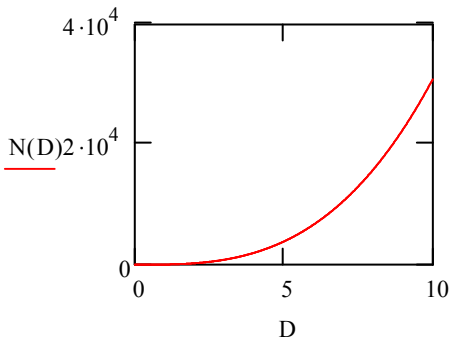

$$N_{ave}(x,y) := \int_{x}^{y} N(z)\cdot\left(\frac{dist(z)}{\int_{x}^{y} dist(w)\,dw}\right) dz$$

Average moles per particles of a part of the distribution from x nm to y nm. This is simply Conc*Volume/number of particles

$$N_{ave}(x) := N_{ave}(0,x)$$

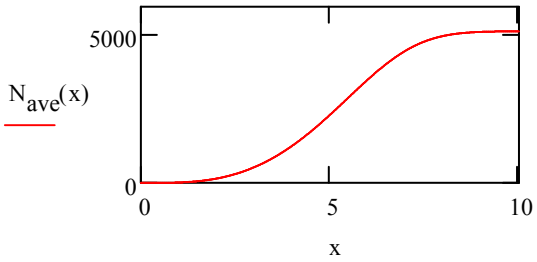

Absorbance from distribution

$$\varepsilon_{ave}(x) := 1$$

overrides inclusion of the extinction coefficient

$$A := \varepsilon Cl$$

$$Abfit(x) := \frac{\varepsilon_{ave}(x)\cdot N_{ave}(x)}{\varepsilon_{ave}(10)\cdot N_{ave}(10)}$$

Generates the absorption curve based on the size distribution and normalizes it.

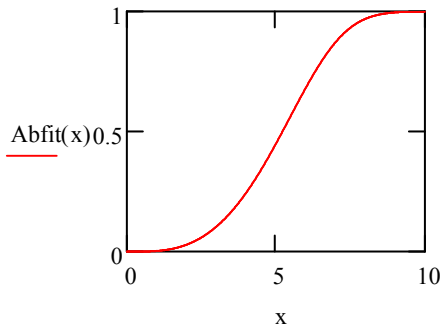

Calculation of the fraction cutoffs

$cutoff := 5$

$Pressure_1 := 525$

$Pressure_2 := 545$

Pressures of each fractionation stage

Given

$UVfit(Pressure_1) = Abfit(cutoff)$

$cutoff_1 := Find(cutoff)$

Says the absorption at the pressure should be equal to the absorption based on the distribution from 0 nm to cutoff

Given

$UVfit(Pressure_2) = Abfit(cutoff)$

$cutoff_2 := Find(cutoff)$

$cutoff_1 = 4.996$

$cutoff_2 = 4.578$

cutoffs for size distribution of each fractionation stage

Calculation of average size of recovered fractions

$$CDF(x) := \int_0^x dist(x)\,dx$$

$average_g := 5$

Given

$$\mathrm{CDF}(\mathrm{average}_g) = \frac{\mathrm{CDF}(10) + \mathrm{CDF}(\mathrm{cutoff}_1)}{2}$$

$$\mathrm{average}_0 := \mathrm{Find}(\mathrm{average}_g)$$

Given

$$\mathrm{CDF}(\mathrm{average}_g) = \frac{\mathrm{CDF}(\mathrm{cutoff}_2) + \mathrm{CDF}(\mathrm{cutoff}_1)}{2}$$

$$\mathrm{average}_1 := \mathrm{Find}(\mathrm{average}_g)$$

Given

$$\mathrm{CDF}(\mathrm{average}_g) = \frac{\mathrm{CDF}(\mathrm{cutoff}_2) + \mathrm{CDF}(0)}{2}$$

$$\mathrm{average}_2 := \mathrm{Find}(\mathrm{average}_g)$$

$$\mathrm{average} = \begin{pmatrix} 5.916 \\ 4.793 \\ 3.959 \end{pmatrix}$$

Appendix B

Statistical Thermodynamic Model Code

B.1 Main Statistical Model Script

```
%clear workspace and command windows and close and figures
clear
clc
close

%CO2 molefractions to fractionate at
CO2 = [0.6 1];

%range of particle sizes to explore and resolution
DiameterLow =5;
DiameterHigh = 20;
DiameterInc = .1;

%preallocation variables for speed
dia = zeros(1,(DiameterHigh-DiameterLow)/DiameterInc+1);
dist = zeros(length(CO2)+1,(DiameterHigh-DiameterLow)/DiameterInc+1);
precip = zeros(length(CO2)+1,(DiameterHigh-DiameterLow)/DiameterInc+1);
averagedist = zeros(length(CO2)+2,1);
stdevdist = zeros(length(CO2)+2,1);
averageprecip = zeros(length(CO2)+1,1);
stdevprecip = zeros(length(CO2)+1,1);
threshold = zeros(length(CO2),(DiameterHigh-DiameterLow)/DiameterInc+1);
percentremain = 1;
percent = zeros(length(CO2)+1,1);

%original distribution statistics
disttype = {'normal'};
%disttype = ('uniform');
averagedist(1) = 4.56 ;
stdevdist(1) = 1.24;

%creates original distribution
for i = 1:((DiameterHigh-DiameterLow)/DiameterInc+1)
     dia(i) = (DiameterLow + (i - 1)*DiameterInc);
     if strcmp(disttype,'normal')==1
        dist(1,i) = normpdf(dia(i),averagedist(1),stdevdist(1));
     elseif strcmp(disttype,'uniform')==1
        dist(1,i) = unifpdf(dia(i),DiameterLow,DiameterHigh);
```

```
        else
            display('Problem with Distribution type')
            pause
        end
    end
    dist(1,:) = dist(1,:)./trapz(dia,dist(1,:));

    %plots original distribution
    hold on
    subplot(411)
    plot(dia,dist(1,:))
    hold all

    %Sets plot parameters
    subplot(412)
    xlabel('Nanoparticle Diameter (nm)')
    ylabel(['Nanoparticle',10,'Threshold Size (nm)'])
    hold all
    subplot(411)
    xlabel('Nanoparticle Diameter (nm)')
    ylabel(['Nanoparticle',10,'Distribution'])
    title('Dispersed Nanoparticles')
    hold all
    subplot(413)
    xlabel('Nanoparticle Diameter (nm)')
    ylabel(['Nanoparticle',10,'Distribution'])
    title('Precipitated Nanoparticles')
    hold all
    subplot(414)
    xlabel('Nanoparticle Diameter (nm)')
    ylabel(['Nanoparticle',10,'Distribution'])
    title('Equilibrium Approach')
    hold all
    pause(1)

    %loop for various CO2 concentrations
    for i = 1:length(CO2)

        %loop to determine threshold particle sizes
        for j = 1:((DiameterHigh-DiameterLow)/DiameterInc+1)

            %creates global variable to be used by subroutines
            global xco2 d1 %#ok<TLEV>
            xco2 = CO2(i);

            %sets diameter for particle of interest
            d1 = (DiameterLow + (j - 1)*DiameterInc);

            %solves for threshold
            options = optimset('TolFun',1e-6,'TolX',1e-6,'Display','off');
            threshold(i,j)  = fsolve(@EvdFun,5,options);

        end
```

```
%plots threshold curve
subplot(412)
plot(dia,threshold(i,:))
hold all
axis([2 20 0 20])
pause(1)

%determine precipitation
iterations = 30;   %number of precipitation until equilibrium
disttemp = zeros(iterations+1,(DiameterHigh-DiameterLow)/DiameterInc+1);
       %preallocation of variable for speed
preciptemp = zeros(iterations+1,(DiameterHigh-DiameterLow)/DiameterInc
   +1);  %preallocation of variable for speed
disttemp(1,:)=dist(i,:);
preciptemp(1,:)= 0*dist(i,:);
for k=2:iterations+1
    distfit = @(x)(spline(dia,disttemp(k-1,:),x));
    %precipfit = @(x)(spline(dia,preciptemp(k-1,:),x));
    for j = 1:((DiameterHigh-DiameterLow)/DiameterInc+1)
        if threshold(i,j) > DiameterHigh
            thres = DiameterHigh;
        else
            thres = threshold(i,j);
        end
        CDF = quad(distfit,DiameterLow,thres)/quad(distfit,DiameterLow,
           DiameterHigh);
        if CDF > 1
            CDF = 1;
        elseif CDF<0
            CDF = 0;
        end
        disttemp(k,j) = disttemp(k-1,j)-disttemp(k-1,j)*(1-CDF);%+
           preciptemp(k-1,j)*CDF;
        preciptemp(k,j) =preciptemp(k-1,j)+disttemp(k-1,j)*(1-CDF);%-
           preciptemp(k-1,j)*CDF;
    end

    %plots precipitation curve every ___ iterations
    if mod(k,1) == 0
        subplot(414)
        hold on
        plot(dia,preciptemp(k,:))
        pause(1)
    end
end

preciparea = trapz(dia,preciptemp(k,:));
percent(i) = percentremain*preciparea;
percentremain = percentremain-percent(i);

%normalizes distributions
dist(i+1,:) = disttemp(k,:)/(1-preciparea);
precip(i,:) = preciptemp(k,:)/preciparea;

```

```
        %determines average and stdev of distribtions
        averagedist(i+1) = trapz(dia,dia.*dist(i+1,:));
        stdevdist(i+1) = sqrt(trapz(dia,(dia-averagedist(i+1)).^2.*dist(i+1,:)))
            ;
        averageprecip(i) = trapz(dia,dia.*precip(i,:));
        stdevprecip(i) = sqrt(trapz(dia,(dia-averageprecip(i)).^2.*precip(i,:)))
            ;

        %plots dispersed particles
        subplot(411)
        plot(dia,dist(i+1,:))
        hold all

        %plots precipitated particles
        subplot(413)
        plot(dia,precip(i,:))
        hold all
        pause(1)
    end

    %final fraction = last dispersed
    precip(i+1,:) = dist(i+1,:);
    averageprecip(i+1) = trapz(dia,dia.*precip(i+1,:));
    stdevprecip(i+1) = sqrt(trapz(dia,(dia-averagedist(i+1)).^2.*precip(i+1,:)))
        ;
    percent(i+1) = percentremain;

    %plots final precipitated fraction
    subplot(413)
    plot(dia,precip(i+1,:))
    pause(1)

    %summary
    stats(:,1) = averageprecip(:);
    stats(:,2) = stdevprecip(:);
    stats(:,3) = percent(:);
    display(stats)

    hold off
```

B.2 Energy Versus Distance Function

```
function energy = EvDfun(d2)

    T = 298.15; %K
    material = 'Au';    %defines what material

    %universal constants
    kB = 1.38*10^(-23);     %(J/K)
    h = 6.62*10^(-34);  %(J*s)
    Na = 6.022*10^23;   %(1/mol)
    ve = 3*10^15;   %(1/sec)
    R = 8.314;  %J/molK

    %molar densities
    vLco2 = 55;  %cm^3/mol
    vLhex = 132; %cm^3/mol

    %material properties (dielectric constant refractive index, hamaker
    %constants)

    %Dielectric Constants
    DCco2 = 1.483;
    DChex = 1.882;
    DCvac = 1;

    %Refractive Indexes
    RIco2 = 1.185;
    RIhex = 1.372;
    RIvac = 1;

    %Hamaker Constant
    A33hex = (3/4)*kB*T*((DChex-DCvac)/(DChex+DCvac))^2+(3*h*ve/(16*sqrt(2))
       )*(RIhex^2-RIvac^2)^2/(RIhex^2+RIvac^2)^(3/2);
    A33co2 = (3/4)*kB*T*((DCco2-DCvac)/(DCco2+DCvac))^2+(3*h*ve/(16*sqrt(2))
       )*(RIco2^2-RIvac^2)^2/(RIco2^2+RIvac^2)^(3/2);
    A11Au = 31.0*10^(-20);  %J
    A11Ag = 35.0*10^(-20); %J

    %solubility parameters
    SPco2 = 12.3;   %(J/cm^3)^1/2
    SPhex = 14.9;   %(J/cm^3)^1/2
    SPlig = 16.0;

    %Miscellaneous ligand properties
    rholig = 850000;    %g/m^3
    MWlig = 202.4;  %g/mol
    AreaThiol = 14.5;   %cross-sectional area of tail
    rlig = 2.27*10^(-10);   %radius of cross-sectional area
```

```
Ligand = 1.21*10^(-9);  %
liglen = (12.4-1.8)*10^(-10);

%Gold Properties
AreaAu = 6.51;

rco2 = 1;
rhex = vLhex/vLco2;

global xco2
xhex = 1-xco2;

vLmix = xco2*vLco2+xhex*vLhex;
phico2 = xco2*vLco2/vLmix;
phihex = 1-phico2;

if strcmp(material,'Au') == 1
    A131 = (sqrt(A11Au)-(phico2*sqrt(A33co2)+phihex*sqrt(A33hex)))^2;
elseif strcmp(material,'Ag') == 1
    A131 = (sqrt(A11Ag)-(phico2*sqrt(A33co2)+phihex*sqrt(A33hex)))^2;
else
    disp('Material Problem')
    pause
end

chico2hex = (vLmix/(R*T))*(SPco2-SPhex)^2;
chico2lig = (vLco2/(R*T))*(SPco2-SPlig)^2;
chihexlig = (vLhex/(R*T))*(SPhex-SPlig)^2;
global d1

RadiusInterest = d1/2*10^(-9);
gamma = 2.054*10^(-10)/RadiusInterest+(1/3);   %surface coverage

ligcollapse=(3*gamma*Ligand*(AreaThiol/AreaAu)*RadiusInterest^2+(
   RadiusInterest+2*rlig)^3)^(1/3)-(RadiusInterest+2*rlig);
%intercept = ligcollapse*10^10;
%shell = @(alpha , x)(alpha.*(x - 1).^2 + intercept);
%load Kitchens
%alpha = 10;
%slope = nlinfit(KitchensCO2,KitchensLen,shell,alpha);
%shelllen = slope*(xco2-1)^2 + intercept;
shelllen = 7.607094864*(xco2-1)^2+5.326704141; %Angstroms
shelllen = shelllen*10^(-10);  %meters

ligcollapse=(3*gamma*Ligand*(AreaThiol/AreaAu)*RadiusInterest^2+(
   RadiusInterest+2*rlig)^3)^(1/3)-(RadiusInterest+2*rlig);
if shelllen < ligcollapse
print('error')
shelllen = ligcollapse;
end
```

```
philigand = 3*gamma*Ligand*(AreaThiol/AreaAu)*RadiusInterest^2/((
    RadiusInterest+shelllen+2*rlig)^3-(RadiusInterest+2*rlig)^3);
RadiusInteraction = d2/2*10^(-9);
l = 1;
vdw = zeros(1,901);
osm = zeros(1,901);
ela = zeros(1,901);
r = zeros(1,901);
for s2stemp=.1:0.01:10
    %plot(r,vdw)
    %pause(1)
    s2s=s2stemp*10^(-9);
    f1 = s2s^2+2*RadiusInterest*s2s+2*RadiusInteraction*s2s;
    f2 = f1+4*RadiusInterest*RadiusInteraction;
    vdw(l) = -(A131/6)*(2*RadiusInterest*RadiusInteraction/f1 + 2*
        RadiusInterest*RadiusInteraction/f2+log(f1/f2));

    s2s = s2s*liglen/shelllen;
    if s2s <= liglen
        osm(l) = (4*pi()*RadiusInterest*kB*T/(vLmix/Na))*10^6*philigand
            ^2*(xco2*(0.5+phihex*rco2*chico2hex-rco2*chico2lig)+xhex
            *(0.5-rhex*chihexlig))*(liglen^2*((s2s/(2*liglen))-(0.25)-(
            log(s2s/liglen))));
        ela(l) = 2*pi()*RadiusInterest*kB*T*liglen^2*philigand*rholig/(
            MWlig/Na)*(((s2s/liglen)*log((s2s/liglen)*((3-s2s/liglen)/2)
            ^2))-6*log((3-s2s/liglen)/2)+3*(1-s2s/liglen));
    elseif s2s < 2*liglen && s2s > liglen
        osm(l) = (4*pi()*RadiusInterest*kB*T/(vLmix/Na))*10^6*philigand
            ^2*(xco2*(0.5+phihex*rco2*chico2hex-rco2*chico2lig)+xhex
            *(0.5-rhex*chihexlig))*(liglen-s2s/2)^2;
        ela(l) = 0;
    else
        osm(l) = 0;
        ela(l) = 0;
    end

    r(l) = s2stemp;
    l=l+1;
end

osm = osm/(kB*T);
vdw = vdw/(kB*T);
ela = ela/(kB*T);
total = osm+vdw+ela;

[minvalue,minindice] = findpeaks(-total);
minvalue = max(minvalue);

energy = minvalue - 1.5;
```

Appendix C

Stochastic Monte Carlo Thermodynamic Model

C.1 Preliminary Stochastic Simulations

The goal of this thermodynamic model is to gain the ability to predict the nanoparticle size that can be dispersed at given solvent conditions, however, due to the many system properties that can vary with nanoparticle size and solvent conditions (ligand surface coverage, ligand length available for solvation, solubility parameters, etc) as well as interactions between different sized nanoparticles, a simple 'static' model may not be able to capture all the inter-nanoparticle interactions. Therefore, a stochastic model has been under development which will allow for a wide range of calculations to be completed starting from a polydisperse sample with variable ligand surface coverage. This will not only allow for the calculation of a very complex system with many variables, but also give an insight into the nature of nanoparticle dispersions.

C.1.1 Theory

Monte Carlo stochastic simulations have been in wide use since the early 1950's with the development of computers with significant computational abilities (Metropolis *et al.*, 1953). The Metropolis scheme for Monte Carlo simulations uses a three-dimensional theoretical box in which N nanoparticles are placed on a lattice or randomly. An energy calculation is then performed for each nanoparticle with respect to every other nanoparticle, Φ_{ij}, according to the potential energy model (total interaction energy), and

hence the total energy of the system (E) is defined.

$$E = \frac{1}{2}\sum_{i}\sum_{\substack{j \\ i \neq j}} \Phi_{ij} \tag{C.1}$$

Each particle is then moved, in turn, in 3 dimensions according to

$$X = X + \alpha\xi_1 \tag{C.2a}$$

$$Y = Y + \alpha\xi_2 \tag{C.2b}$$

$$Z = Z + \alpha\xi_3 \tag{C.2c}$$

where α is the maximum one-dimensional step size, and ξ_1, ξ_2, and ξ_3 are random numbers between -1 and 1, such that after a single move a particle is equally likely to be inside a box of side length 2α centered about its original position. After a single nanoparticle move, the energy change of the system (ΔE) is recalculated according to Equation C.1. If the move brings the system to a lower energy state, i.e. $\Delta E < 0$, the move is allowed. If $\Delta E > 0$ we allow the move only if Equation C.3 is true.

$$\xi_4 < \exp\left(-\frac{\Delta \mathrm{E}}{\mathrm{k_B T}}\right) \tag{C.3}$$

where ξ_4 is a random number between 0 and 1. We allow the move to occur even with a probability of the system increasing in energy. If $\Delta E > 0$ and Equation C.3 is not true, the move is not allowed and a new move according to Equation C.2 is made. A series of M moves is performed, where each particle is moved M total times sequentially until the system energy remains stable. At this point, the system is in a local energy minimum not necessarily a global energy minimum. Therefore this energy calculation must be performed several times from the same original positions in order to verify results. At the end of the M moves, any nanoparticle with a total interaction energy with any other nanoparticle less than the Boltzmann threshold energy for dispersion ($-3/2k_BT$) will be

considered as precipitated and removed from further calculations. The solvent conditions can now be changed and the calculation repeated, in essence performing the size-selective fractionation stages as a Monte Carlo simulation. Each fraction can then be analyzed the same way a TEM image would be, by analyzing the mean diameter and standard deviation of the 'recovered fraction.'

C.1.2 Simulation Parameters

At current computational scales, only a limited simulation can be performed, i.e. the number of simulated nanoparticles, N, is kept low (10 - 1000) and the total number of moves per nanoparticle, M, is kept low (100 - 5000). Current computational scales (1 CPU) performs the simulations in several hours, therefore the number of simulated nanoparticles and moves per nanoparticle must be kept low. This allows for bench testing of the simulation, and hence, the results are strictly preliminary as they do not necessarily represent a system in a local energy minimum. The size of the box which contains the nanoparticles is sized such that the nanoparticle number density matches experimental data ($\approx 2.5 \cdot 10^{27} nanoparticles/m^3$), which has been calculated from TEM sizing data along with TGA mass data. Preliminary simulations were performed with a move length, α, of 1 Å, however this will need to be reduced in later simulations. As the number of moves per nanoparticle is kept low and the move length is relatively large, nanoparticles were placed randomly to investigate the movement of nanoparticles. Particles that are placed on a lattice have been typically too far apart to see significant changes. The simulation code is available in Appendix D.

C.1.3 Results

A simulation of 30 nanoparticles (Gaussian distributed, average diameter 5 nm with a standard deviation of 1 nm) in a box with sides of 230 nm in pure hexane was performed allowing for a sufficient number of cycles until the total interaction energy of the system

stabilizes. The total energy of the system, as given in Equation C.1, trends to lower values with increasing cycles, as expected. Interestingly, each time a nanoparticle or nanoparticles begin to group together in small clusters, the energy drastically drops and leads to the shoulders evident in Figure C.1. It was found that the nanoparticles maintain a separation distance of $2l$ or such that the ligands between the nanoparticles do not touch and hence there is no, or very little, repulsive energy. A three-dimensional rendering of the nanoparticles at the beginning and end of simulation for comparison can be seen in Figure C.2.

A second simulation of 1000 nanoparticles (Gaussian distributed, average diameter 5nm with a standard deviation of 1 nm) in a box with sides of 720 nm in pure hexane was performed with a slightly modified total interaction energy to investigate how the simulation performs with large particle numbers. This modified total interaction model was similar to Sutherland potential model with a positive infinite potential for separation distances $h < 2l$. This allows for a simpler calculation while still maintaining the van der Waals attractive potential. As the previous simulation showed that the nanoparticles settle to a distance such that the osmotic repulsive energy is negligible and the elastic repulsive energy is nonexistent, performing this simulation where the ligands do not interact is not trivial. The total van der Waals energy (which is equal to the total interaction energy in this simulation) of each nanoparticle is proportionally distributed against nanoparticle size, as seen in Figure C.3. As expected, the largest nanoparticles experience the largest total van der Waals potential and hence, the largest nanoparticles would be the first to be excluded from the simulation due to the total interaction energy being less than the Boltzmann threshold. However, it is clear that there is no 'threshold nanoparticle size,' and recovered fractions would have size distributions, as can be seen from experiments.

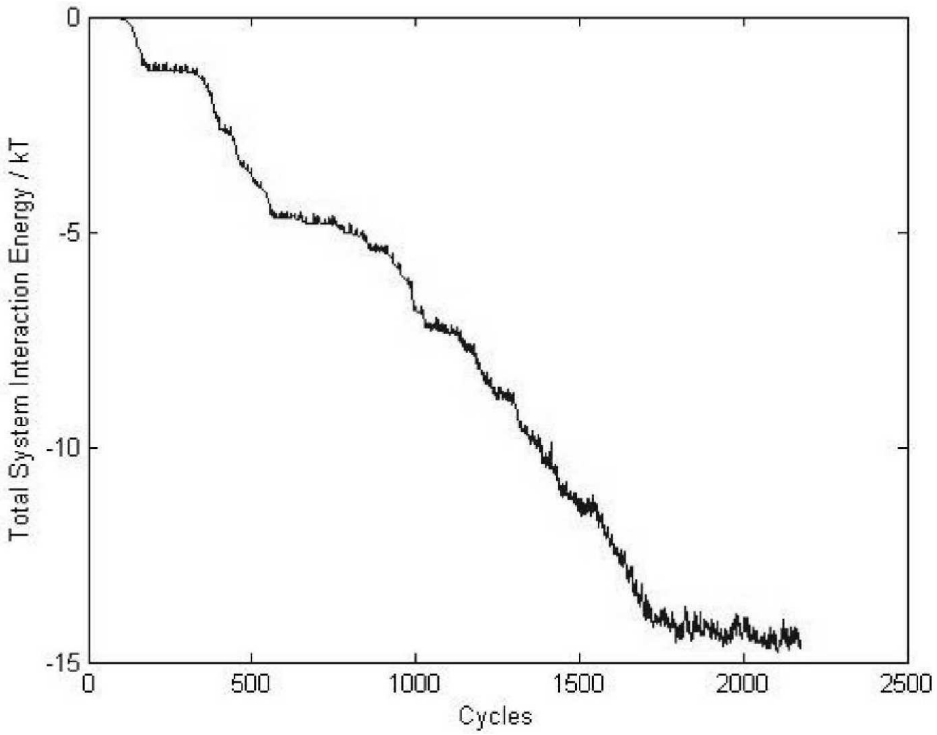

Figure C.1: Total system interaction energy for a Monte Carlo simulation of 30 nanoparticles in a box of edge length 230 nm.

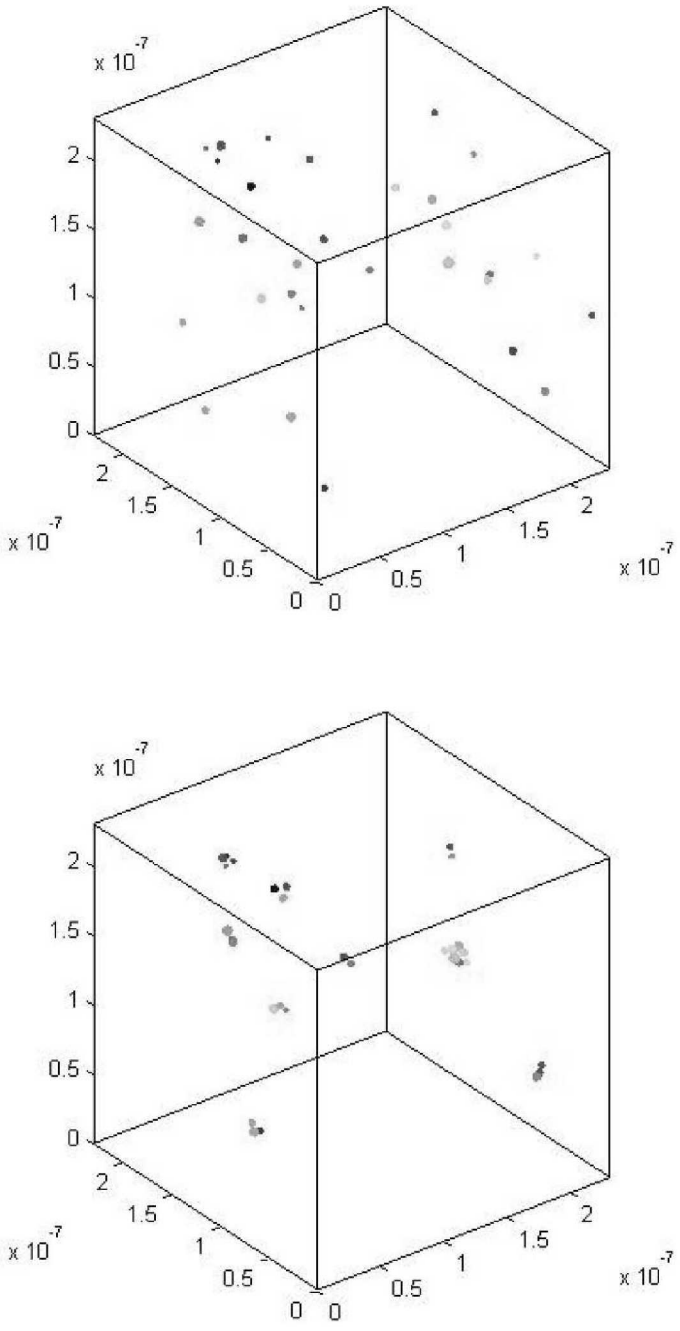

Figure C.2: Example three dimensional rendering of a 30 nanoparticle Monte Carlo simulation (top) before and (bottom) after performing the simulation.

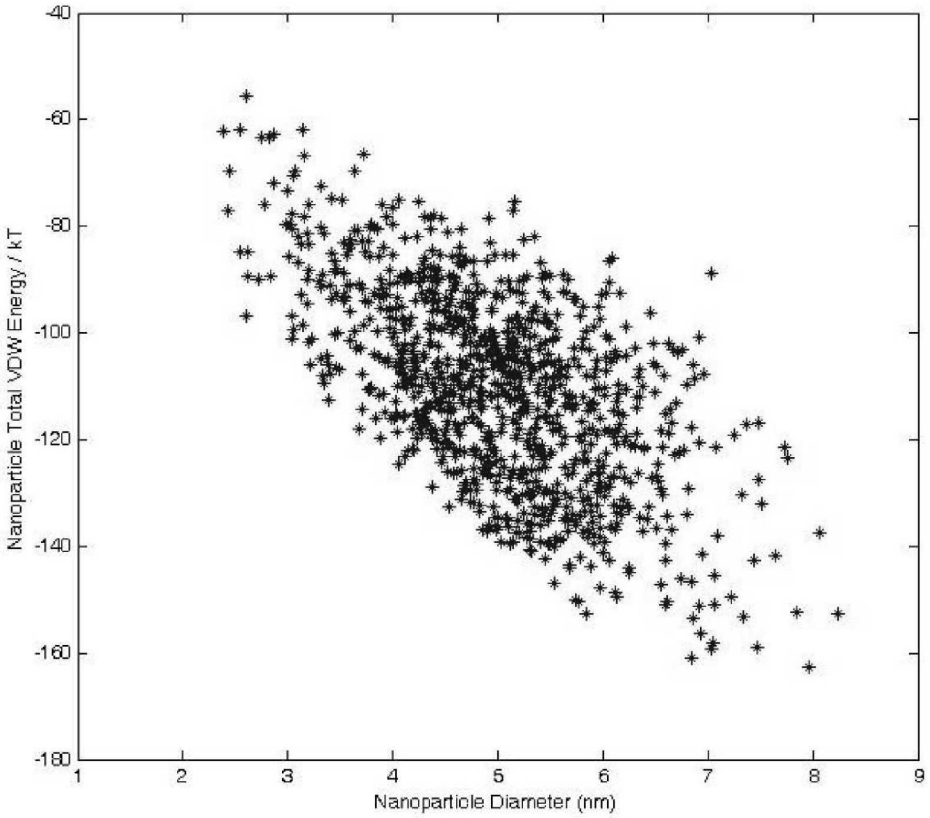

Figure C.3: Distribution of the total van der Waals potential a nanoparticle experiences when simulated with 1000 Gaussian-distributed sized nanoparticles using a Sutherland-like model.

Appendix D

Stochastic Monte Carlo Simulation Code

D.1 Main Stochastic Monte Carlo Script

```
clear        %clears workspace variables
clc          %Clears Command Window
tic          %Starts a system timer

format short e          %Formats Output
makeplot = 0;           %Makes a Plot if 1
makemovie = 0;          %Makes a Video if 1
makeMCmovie = 0;        %makes an MC Video if 1
doMC = 0;                %Performs MC Steps if 1
savedata = 0;            %saves data
ParticleNumber=1000;                %number of particles
BoxDim= 0.00000072;           %Box Dimension
Volume = BoxDim^3;
DistMu=5*10^(-9);           %Particle Distribution Average Diameter
DistSigma= 1*10^(-9);      %Particle Distribution Standard Deviation

T = 300;        %(K)
xco2 = 0;       %mole fraction of CO2
xhex = 1-xco2;


MCmoves = 10000;     %Number of Monte Carlo Moves to be allowed
MClen = 0.1*10^-9 ; %MC move length


ParticleDensity = ParticleNumber/Volume;
fprintf('Total Volume is %.2d mL \n', Volume*100^3)
fprintf('Particle Number Density is %.2d \n', ParticleDensity)

disp('Generating Random Positions')
pause(.01)
size = normrnd(DistMu,DistSigma,[ParticleNumber,1]); %Size Matrix (m)
fprintf('Simulating a %.2d +/- %.2d nm system, (inputed %.1d +/- %.1d nm) \n
    ', mean(size)*10^9,std(size)*10^9,DistMu,DistSigma)
position = BoxDim.*rand([ParticleNumber,3]); %position matrix (m)
colors = rand([ParticleNumber,3]);
disp('Checking for Overlapping Particles')
for i = 1:ParticleNumber
```

```
    Overlaps = 1;
    while Overlaps > 0
        Overlaps = 0;
        for j = 1:ParticleNumber
            if j ~= i
                if s2sdistance(position(i,1),position(i,2),position(i,3),
                    size(i)/2,position(j,1),position(j,2),position(j,3),size(
                    j)/2)<0;
                    Overlaps = Overlaps +1;
                end
            else
            end
        end
        if Overlaps > 0
            fprintf('Found %i overlaps on the %i particle.  Must Fix \n',
                Overlaps,i)
            position(i,1) = BoxDim*rand;
            position(i,2) = BoxDim*rand;
            position(i,3) = BoxDim*rand;
        end
    end

end

if makeplot == 1
    plotspheres(position(:,1),position(:,2),position(:,3),size./2,BoxDim,
        colors);
end
if makemovie == 1
    frames = 180;
    m = moviein(frames);
    [az,el] = view;
    for i= 1:frames
        m(:,i) = getframe(gcf);
        az = az + 2;
        view(az,el);
    end
    movie2avi(m,'newvideo','QUALITY',100);
end

distance = zeros(ParticleNumber);
for i = 1:ParticleNumber
    for j = 1:ParticleNumber
        distance(i,j) = s2sdistance(position(i,1),position(i,2),position(i
            ,3),size(i)/2,position(j,1),position(j,2),position(j,3),size(j)
            /2);
    end
    distance(i,i) = 0;
end

disp('Starting Energy Calculations')
pause(0.01)
```

```
initiateconstants

[vanderwaals osmotic elastic TotalEnergy] = systemenergy(ParticleNumber,size
    ,position,T,xco2);

TotalEnergy = vanderwaals+osmotic+elastic;
disp('Energy Calculations Completed')


if doMC == 1

    disp('Beginning Monte Carlo Moves')

    MCposition = zeros(ParticleNumber,3,MCmoves+1);
    MCTotalEnergy = zeros(MCmoves+1,1);

    for h = 1 : MCmoves
        MCposition(:,:,h) = position(:,:);
        MCTotalEnergy(h) = sum(TotalEnergy);
        plot(1:MCmoves+1,MCTotalEnergy/(kB*T))
        pause(0.01)
        MCaccepts = 0;
        for i = 1:ParticleNumber
            MCEnergy = 0;
            while MCEnergy < 4
                Overlaps = 1;
                while Overlaps > 0
                    Overlaps = 0;
                    tempposition = [position(i,1)+(2*rand-1)*MClen,position(
                        i,2)+(2*rand-1)*MClen,position(i,3)+(2*rand-1)*MClen
                        ];   %Monte Carlo Move
                    for j = 1:ParticleNumber
                        if j ~= i
                            if s2sdistance(tempposition(1),tempposition(2),
                                tempposition(3),size(i)/2,position(j,1),
                                position(j,2),position(j,3),size(j)/2)<0;
                                 Overlaps = Overlaps +1;
                            end
                        end
                    end
                    if Overlaps > 0
                        %fprintf('Found %i overlaps on the %i particle.
                            Must Fix \n',Overlaps,i)
                    end
                end
               temptotalposition = position;
               temptotalposition(i,:) = tempposition;
               [tempvanderwaals temposmotic tempelastic TempTotalEnergy] =
                   systemenergy(ParticleNumber,size,temptotalposition,T,xco2)
                   ;
                delTotalEnergy = sum(TempTotalEnergy)- sum(TotalEnergy);
                if (sum(TempTotalEnergy)/(kB*T)) > 0
                     MCEnergy = MCEnergy+1
```

```
                elseif (delTotalEnergy < 0 || rand > exp(-delTotalEnergy/(kB
                    *T))) %Accepts the MCMove
                    MCEnergy = 11;
                    MCaccepts = MCaccepts +1;
                    position(i,:) = tempposition;
                    [vanderwaals osmotic elastic TotalEnergy] = systemenergy
                        (ParticleNumber,size,position,T,xco2);
                    if sum(TotalEnergy) > 0
                        send_text_message('412-849-XXXX','att2','problem','
                            system paused, Totalenergy positive')
                        pause

                    end
                else
                    MCEnergy = MCEnergy+1;
                end
            end
        end
        %plotspheres(position(:,1),position(:,2),position(:,3),size./2,
            BoxDim,colors);
        fprintf('Accepted %i Moves out of %i on Monte Carlo Move Of %i   \n'
            ,MCaccepts, ParticleNumber,h)

    end
    MCposition(:,:,MCmoves+1) = position(:,:);
    MCTotalEnergy(MCmoves+1) = sum(TotalEnergy);
end

if makeMCmovie == 1
        frames = MCmoves;
        m = moviein(frames);
        for i= 1:frames
            plotspheres(MCposition(:,1,i),MCposition(:,2,i),MCposition(:,3,i
                ),size./2,BoxDim,colors)
            m(:,i) = getframe(gcf);
            close

        end
        movie2avi(m,'newvideo','QUALITY',100);
end

toc
if savedata == 1
    save('Overnight.mat','*')
    send_text_message('412-849-XXXX','att2','MATLAB','Finished Successfully'
        )
end
```

D.2 Initiateconstants Script

```
vLco2 = .00055;   %(m^3/mol)
vLhex = .00132;    %(m^3/mol)
vLmix = vLco2*xco2+vLhex*xhex;
gamma = 0.75;
liglen = 15*10^(-10);  %ligand length in m
phico2 = xco2*vLco2 / (xco2*vLco2+ xhex*vLhex);
phihex = 1-phico2;
A11 = 31.0*10^(-20);    %gold-gold in vacuum (J)
kB = 1.38*10^(-23);     %(J/K)
h = 6.62*10^(-34);  %(J*s)
Na = 6.022*10^23;   %(1/mol)
ve = 3*10^15;   %(1/sec)
eco2 = 1.483;
ehex = 1.882;
evac = 1;
nco2 = 1.185;
nhex = 1.372;
nvac = 1;
A33co2 = (3/4)*kB*T*((eco2-evac)/(eco2+evac))^2+(3*h*ve/(16*sqrt(2)))*((nco2
    ^2-nvac^2)^2)/((nco2^2+nvac^2)^2);
A33hex = (3/4)*kB*T*((ehex-evac)/(ehex+evac))^2+(3*h*ve/(16*sqrt(2)))*((nhex
    ^2-nvac^2)^2)/((nhex^2+nvac^2)^2);
A131 = (sqrt(A11)-(phico2*sqrt(A33co2)+phihex*sqrt(A33hex)))^2;
rco2 = 1;
rhex = vLhex/vLco2;
delco2 = 12.3;  %(J/cm^3)
delhex = 14.9;  %(J/cm^3)
dellig = 16.0;  %(J/cm^3)
R= 8.314; %(J/molK)
chico2hex = (vLmix/R*T)*(delco2 - delhex)^2;
chico2lig = (vLmix/R*T)*(delco2 - dellig)^2;
chihexlig = (vLmix/R*T)*(delhex - dellig)^2;
rholig = 850000;    %g/m^3
MWlig = 202.4;
```

D.3 S2sdistance Function

```
function distance = s2sdistance(x1,y1,z1,r1,x2,y2,z2,r2)

  distance = sqrt((x1-x2)^2+(y1-y2)^2 + (z1-z2)^2)-(r1+r2);
```

D.4 Systemenergy Function

```
function [vdw osm ela total] = systemenergy(ParticleNumber,size,position,T,
    xco2)

xhex = 1- xco2;

vLco2 = .00055;   %(m^3/mol)
vLhex = .00132;    %(m^3/mol)
vLmix = vLco2*xco2+vLhex*xhex;
gamma = 0.75;
liglen = 15*10^(-10);  %ligand length in m
phico2 = xco2*vLco2 / (xco2*vLco2+ xhex*vLhex);
phihex = 1-phico2;
A11 = 31.0*10^(-20);    %gold-gold in vacuum (J)
kB = 1.38*10^(-23);     %(J/K)
h = 6.62*10^(-34);  %(J*s)
Na = 6.022*10^23;   %(1/mol)
ve = 3*10^15;   %(1/sec)
eco2 = 1.483;
ehex = 1.882;
evac = 1;
nco2 = 1.185;
nhex = 1.372;
nvac = 1;
A33co2 = (3/4)*kB*T*((eco2-evac)/(eco2+evac))^2+(3*h*ve/(16*sqrt(2)))*((nco2
    ^2-nvac^2)^2)/((nco2^2+nvac^2)^2);
A33hex = (3/4)*kB*T*((ehex-evac)/(ehex+evac))^2+(3*h*ve/(16*sqrt(2)))*((nhex
    ^2-nvac^2)^2)/((nhex^2+nvac^2)^2);
A131 = (sqrt(A11)-(phico2*sqrt(A33co2)+phihex*sqrt(A33hex)))^2;
rco2 = 1;
rhex = vLhex/vLco2;
delco2 = 12.3;  %(J/cm^3)
delhex = 14.9;  %(J/cm^3)
dellig = 16.0;  %(J/cm^3)
R= 8.314; %(J/molK)
chico2hex = (vLmix/R*T)*(delco2 - delhex)^2;
chico2lig = (vLmix/R*T)*(delco2 - dellig)^2;
chihexlig = (vLmix/R*T)*(delhex - dellig)^2;
rholig = 850000;    %g/m^3
MWlig = 202.4;


vanderwaals = zeros(ParticleNumber,1);
osmotic = zeros(ParticleNumber,1);
elastic = zeros(ParticleNumber,1);
for i = 1:ParticleNumber
    philigand = gamma*(3*(size(i)/2)^2*liglen/(((size(i)/2)+liglen)^3-(size(
        i)/2)^3));
    for j = 1:ParticleNumber
```

```
        if j≠i
            s2s = s2sdistance(position(i,1),position(i,2),position(i,3),size(
                i)/2,position(j,1),position(j,2),position(j,3),size(j)/2);
            rad1 = size(i)/2;
            rad2 = size(j)/2;
            newvalueVDW = -(A131/6)*((2*rad1*rad2/(s2s^2+2*rad1*s2s+2*rad2*
                s2s))+((2*rad1*rad2)/(s2s^2+2*rad1*s2s+2*rad2*s2s+4*rad1*rad2)
                )+log((s2s^2+2*rad1*s2s+2*rad2*s2s)/(s2s^2+2*rad1*s2s+2*rad2*
                s2s+4*rad1*rad2)));

             if s2sdistance(position(i,1),position(i,2),position(i,3),size(i)
                /2,position(j,1),position(j,2),position(j,3),size(j)/2) <
                liglen
                 newvalueOSM = (4*pi*(size(i)/2)*kB*T/(vLmix/Na))*philigand
                     ^2*(xco2*(0.5+phihex*rco2*chico2hex-rco2*chico2lig)+xhex
                     *(0.5-rhex*chihexlig))*(liglen^2*(s2sdistance(position(i
                     ,1),position(i,2),position(i,3),size(i)/2,position(j,1),
                     position(j,2),position(j,3),size(j)/2)/(2*liglen)-0.25-
                     log(s2sdistance(position(i,1),position(i,2),position(i,3)
                     ,size(i)/2,position(j,1),position(j,2),position(j,3),size
                     (j)/2)/liglen)));
                 newvalueELA = -((2*pi*(size(i)/2)*kB*T*philigand*rholig*
                     liglen^2)/(MWlig/Na))*((s2sdistance(position(i,1),
                     position(i,2),position(i,3),size(i)/2,position(j,1),
                     position(j,2),position(j,3),size(j)/2)/liglen)*log((
                     s2sdistance(position(i,1),position(i,2),position(i,3),
                     size(i)/2,position(j,1),position(j,2),position(j,3),size(
                     j)/2)/liglen)*(((3-(s2sdistance(position(i,1),position(i
                     ,2),position(i,3),size(i)/2,position(j,1),position(j,2),
                     position(j,3),size(j)/2)/liglen))/2)^2))-6*log((3-(
                     s2sdistance(position(i,1),position(i,2),position(i,3),
                     size(i)/2,position(j,1),position(j,2),position(j,3),size(
                     j)/2)/liglen))/2)+3*(liglen-(s2sdistance(position(i,1),
                     position(i,2),position(i,3),size(i)/2,position(j,1),
                     position(j,2),position(j,3),size(j)/2)/liglen)));
             elseif liglen < s2sdistance(position(i,1),position(i,2),position
                 (i,3),size(i)/2,position(j,1),position(j,2),position(j,3),
                 size(j)/2) && s2sdistance(position(i,1),position(i,2),
                 position(i,3),size(i)/2,position(j,1),position(j,2),position(
                 j,3),size(j)/2) < 2*liglen
                 newvalueOSM = (4*pi*(size(i)/2)*kB*T*philigand^2/(vLmix/Na))
                     *(xco2*(0.5+phihex*rco2*chico2hex-rco2*chico2lig)+xhex
                     *(0.5-rhex*chihexlig))*(liglen-s2sdistance(position(i,1),
                     position(i,2),position(i,3),size(i)/2,position(j,1),
                     position(j,2),position(j,3),size(j)/2)/2)^2;
                 newvalueELA = 0;
             else
                 newvalueOSM = 0;
                 newvalueELA = 0;
             end
             vanderwaals(i) = vanderwaals(i) + newvalueVDW;
             osmotic(i) = osmotic(i) + newvalueOSM;
             elastic(i) = elastic(i) + newvalueELA;
         end
```

```
      end
65 end


  vdw = vanderwaals;
  osm = osmotic;
70 ela = elastic;
  total = vdw + osm + ela;
```